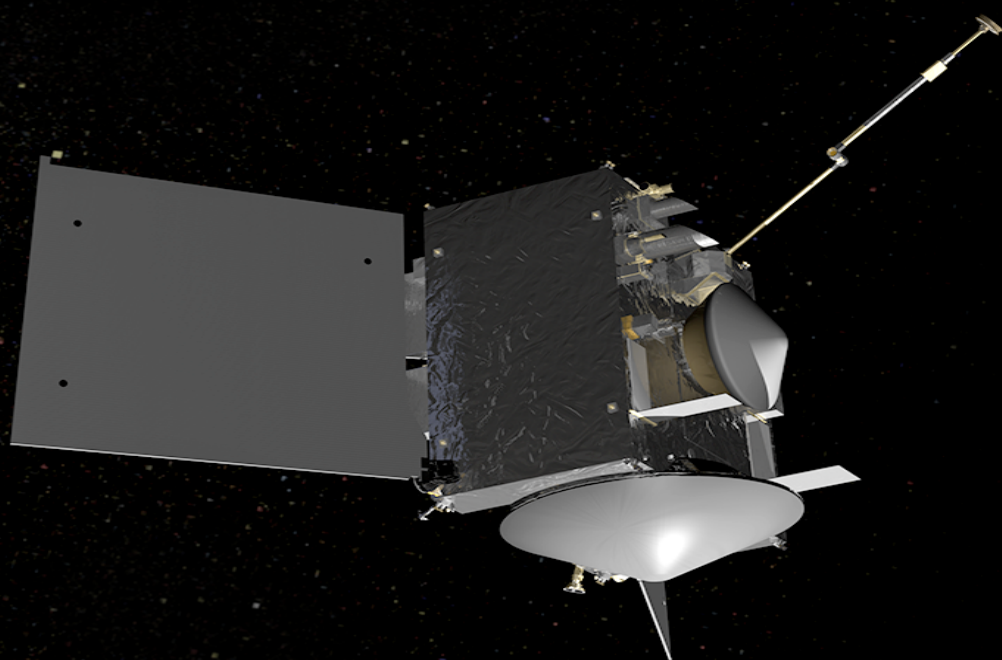


Autonomous Guidance for Asteroid Mapping and Touch and Go Descent

Dual Quaternion Approach

S. Hazra



Autonomous Guidance for Asteroid Mapping and Touch and Go Descent

Dual Quaternion Approach

by

S. Hazra

to obtain the degree of Master of Science
at the Delft University of Technology,
to be defended publicly on –

Student number: 4598342
Project duration: November 18, 2017 – June 18, 2018
Thesis committee: Prof. dr. ir. E. Mooij, TU Delft
Dr. ir. M. Sagliano, DLR

This thesis is confidential and cannot be made public until –

An electronic version of this thesis is available at <http://repository.tudelft.nl/>.



Abstract

With the onset of the age of space travel, asteroid missions have been steadily gaining interest. The pristine nature of asteroids due to their preserved state since the formation of the solar system is an opportunity to unravel many mysteries about the solar system. Also with the ever growing need for resources, asteroids prove to be a plentiful source. With the discovery of asteroids in the close vicinity of our planet and a probable threat to the preservation of life, a need for defence missions has also arisen. With many successful missions like NEAR to Eros, Rosetta to Comet 67P, Hayabusa to Itokawa etcetera, the requirement of precise navigation with autonomous guidance and control for future missions has been established.

The ever-growing need for better computational speed and accuracy has led to the development of new representations for attitude and position of the spacecraft in the past. The usual methods of representations of position and attitude (pose) are the Cartesian coordinates and quaternions. A recent development is the simultaneous representation of the pose of the spacecraft using dual quaternions which are eight-dimensional vectors. As of December 2017, a variety of missions using dual quaternions for relative navigation, rendezvous and docking, entry, descent and landing have been conceptualized.

In this thesis, we try to combine two recently developed guidance methods: *Sampling Based Motion Planning Optimisation* and *Successive Convexification* with a *Dual Quaternion Approach* for mapping the asteroid and descending on it respectively. To achieve this we browse through past missions to establish the requirements of a mission to asteroids, explore the augmented algebra of dual numbers and their application in the concept of dual quaternions, establish how the environment around the asteroid needs to be modelled for a realistic validation of the GN&C algorithm and also study the kinematics and dynamics of the spacecraft using dual quaternions in relative frame.

The relative navigation for an asteroid mission using dual quaternions (Razgus 2017) and (Mao, Szmuk, and Acikmeşe 2016) (Surovik and Scheeres 2014) form the base of this thesis and we build the guidance algorithms to incorporate them.

Preface

qwertzuiop

*S. Hazra
Delft, 2018*

Contents

Preface	v
1 Introduction	1
1.1 Asteroid Mission Objectives	2
1.2 Guidance, Navigation, and Control	3
1.3 Dual Quaternions	4
1.4 Research Questions	4
1.5 Report Outline	5
2 Asteroids and Mission Heritage	7
2.1 Asteroids	7
2.1.1 Classification by Location	7
2.1.2 Classification by Composition	9
2.1.3 Properties of Asteroids	9
2.2 Mission Heritage	10
2.2.1 Asteroid Missions	10
2.2.2 Autonomous GNC and Dual Quaternion Research	14
2.3 Research Mission	15
2.3.1 Target Asteroids	15
2.3.2 Mission Objectives	16
2.3.3 Mission Requirements	16
2.3.4 Assumptions	17
2.4 Conclusion	17
3 Dual Quaternions	19
3.1 Dual Numbers	19
3.1.1 Dual Numbers Arithmetic Operations	19
3.1.2 Dual Vectors	20
3.2 Dual Quaternions	20
3.2.1 Dual Quaternions Geometric Algebra	20
3.2.2 Dual Quaternion Conjugates	21
3.2.3 Unit Dual Quaternion	22
3.3 Dual Quaternion Attitude and Position Representation	22
3.3.1 Rigid Displacement	22
3.4 Screw Motion with Dual Quaternions	24
3.4.1 Plücker Coordinates	24
3.4.2 Screw Displacement	25
3.4.3 Screw Linear Interpolation	27
3.5 DQ Example	27
4 Asteroid and Spacecraft Orbital and Attitude Dynamics	29
4.1 Reference Frames	29
4.2 Attitude Representation Methods	31
4.2.1 Direction Cosine Matrices (DCMs) and Euler Angles	31
4.2.2 Euler's Eigenaxis Rotation and Quaternions	33
4.2.3 Rodrigues Parameters	35
4.2.4 Dual Quaternions	36
4.3 Reference Frame Transformations	36
4.4 Translational Motion (Orbital Motion)	38
4.4.1 Kinematics	38
4.4.2 Dynamics	38

4.5	Rotational Motion	38
4.5.1	Kinematics	38
4.5.2	Attitude Dynamics	39
4.6	Asteroid Dynamics	39
4.7	Relative Dynamics and Kinematics	40
4.7.1	Translational Motion	40
4.7.2	Rotational Motion	40
4.8	Dual Quaternion Dynamics and Kinematics	41
4.8.1	DQ Inertial EOMS	41
4.8.2	DQ Relative Kinematics	42
4.8.3	DQ Relative Dynamics	42
4.9	State Vectors	43
4.10	External Disturbances	43
4.10.1	Small Body Gravity Field	44
4.10.2	Third Body Gravitational Perturbation	49
4.10.3	Solar Radiation Pressure	50
4.10.4	Disturbances in the B Frame	51
5	Fundamentals of Autonomous Guidance and Control	53
5.1	Elements of GNC System	53
5.1.1	Definitions of Guidance, Navigation and Control	53
5.1.2	GNC Architecture and System Interaction	54
5.1.3	Separating Guidance from Navigation	54
5.1.4	General Guidance Problem	55
5.2	Technological Considerations for Autonomous G&C	56
5.2.1	Reasons for High Resolution Imaging and Precise Ranging	57
5.2.2	Reasons for Hazard Detection	59
5.2.3	Reasons for Precision Descent/Landing	59
5.2.4	Relevance to the Guidance System	60
5.3	Global Mapping Phase	60
5.3.1	Basic Mapping GNC framework	61
5.3.2	Refined Problem Formulation	62
5.4	Touch and Go Descent Phase	62
5.4.1	Basic Descent GNC framework	63
5.4.2	Refined Problem Formulation	63
6	Sampling Based Motion Planning	65
6.1	Predictive Model	65
6.2	Abstract Reachability	65
6.3	Map Computation	65
6.4	Planning	65
7	Successive Convex Optimisation	67
7.1	Basic Concepts of Convex optimisation	68
7.1.1	Convex Sets and Functions	68
7.1.2	Convex optimisation Problems: Second-Order Cone Programming	70
7.2	Lossless Convexification	71
7.2.1	Introduction of Slack Variables	72
7.2.2	Change of Variables	73
7.3	Dual Quaternion Problem Formulation	75
7.4	Successive Convexification	76
7.4.1	Linearisation	76
7.4.2	Virtual Control	78
7.4.3	Trust Regions	78

7.5	Extended Convex Guidance	79
7.5.1	Need for Extended Constraints.	79
7.5.2	Glide-Slope Constraint.	79
7.5.3	Attitude Constraints	80
7.5.4	Thrust Direction Constraint	80
7.5.5	Polyhedral Gravity Field	80
7.6	Discretisation	80
7.7	Algorithm	80
8	Simulator Design and Verification	81
8.1	Software Architecture	81
8.2	Spacecraft Model	82
8.2.1	Structure.	83
8.2.2	Mass Properties	83
8.2.3	Reflectivity.	84
8.3	Asteroid Model	84
8.3.1	Polyhedron Model	85
8.3.2	Landmark Map.	85
8.3.3	Illumination Model	86
8.4	Dynamics Model	87
8.4.1	Translational and Rotational Motion.	87
8.4.2	Solar Radiation Pressure	89
8.4.3	Third Body Perturbation	90
8.4.4	Gravity Gradient Torque	90
8.4.5	Polyhedron Gravity	90
8.5	Validation.	91
8.5.1	SPICE	91
8.6	Control Actuators	91
8.7	Navigation	91
9	Results	93
10	Conclusions and Recommendations	95
A	Mathematical Properties	97

Nomenclature

Abbreviations

AOCS	Attitude and Orbit Control System
AU	Astronomical Unit
COM	Centre of Mass
DCM	Direction Cosine Matrix
DOF	Degree of Freedom
DQ	Dual Quaternion
DQEKF	Dual Quaternion Extended Kalman Filter
DQMEKF	Dual Quaternion Multiplicative Extended Kalman Filter
EKF	Extended Kalman Filter
ESA	European Space Agency
FOV	Field of View
GG	Gravity Gradient
GNC	Guidance, Navigation and Control
GPS	Global Positioning System
IMU	Inertial Measurement Unit
IRU	Inertial Reference Units
JAXA	Japanese Space Agency
JPL	Jet Propulsion Laboratory
LIDAR	Light Imaging, Detection, And Ranging
LOS	Line of Sight
LR	Laser Ranger
LVLH	Local Vertical Local Horizontal
MC	Monte Carlo
MEKF	Multiplicative Extended Kalman Filter
MEMS	Micro-Electro-Mechanical System
NAIF	Navigation and Ancillary Information Facility
NASA	National Aeronautics and Space Administration
NAVCAM	Navigation Camera
NEA	Near-Earth Asteroid
NEAR	Near Earth Asteroid Rendezvous
QVEKF	Quaternion-Vector Extended Kalman Filter
RK45	Runge-Kutta 45
SC	Spacecraft
SPICE	Spacecraft, Planet, Instrument, C-matrix, Events
SRP	Solar-Radiation Pressure
STT	Star Tracker

Introduction

Asteroids are the remnant debris from the planetary formation phases during the initialisation of the solar system around 4.6 billion years ago. The debris left from the phase of the runaway growth were perturbed by the newly formed planetary embryos that were cleaning up the gas and matter in their path. The gravity of newly formed Jupiter brought an end to the formation of planetary bodies in the region near it and caused the small bodies to collide with one another, fragmenting them into the asteroids we observe today. They can provide details of the process of core formation or the composition of the protoplanetary disk due to the different condensates present at varying distances from the protosun. Furthermore, collisions of such asteroids on Earth could be its source of water. They could also provide information to establish possible mechanisms for the formation of the inner planets. Figure 1.1 provides a visual of the presently believed procedure of the formation of the solar system.

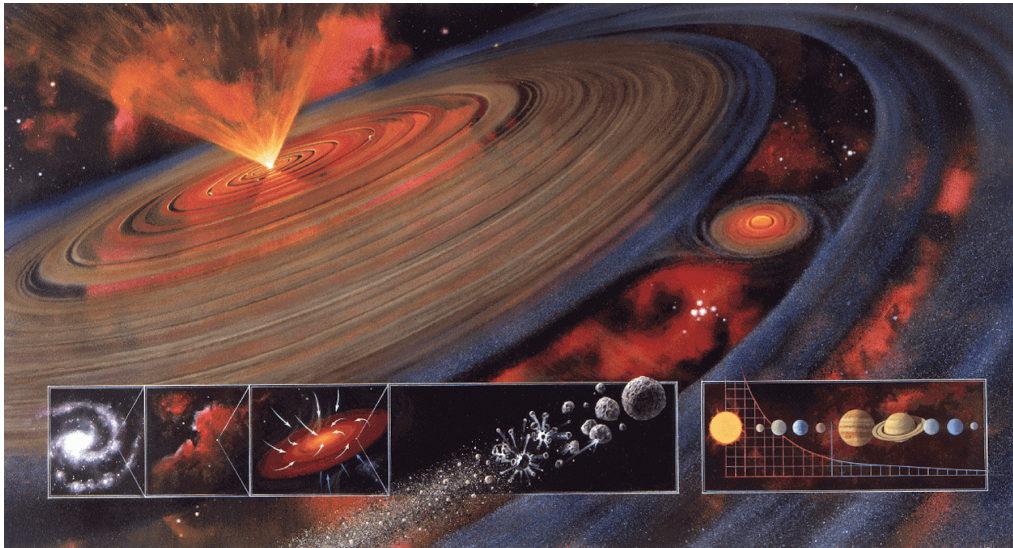


Figure 1.1: An artist's rendition of the planetary formation process ¹

Unfortunately, despite the weak nominal accelerations present at small bodies, the fuel cost of continually overpowering the natural dynamics to simplify trajectory design can become excessive for longer-duration close-proximity operations [6, 9]. This motivates the leveraging of the natural system dynamics in order to enable ambitious mission concepts, a prospect that would require extensive tool development for accurately and rapidly exploring the complex mission design space and identifying efficient and innovative trajectories [10]. Consequently, a need for advanced trajectory design tools and GNC capabilities to meet the challenges of these complex and unintuitive regimes is well-recognized [11]. As will be discussed later, this capability

¹<http://www.agnld.uni-potsdam.de/frank/research.html>; da: 04-10-17

might have benefited the design of the deployment trajectory for the Philae lander, whose energetic touch-down resulted in a large rebound and ultimate landing at an unfavorable distant location after energy dissipation and anchoring systems failed. 1.1.3 Modern Trends Due to the high cost and latency of remotely operating an interplanetary mission from Earth, an autonomous online implementation of such design techniques is highly desirable [12]. Problems encountered by the Hayabusa mission illustrate the drawbacks of insufficiently developed autonomous capabilities | its touch-and-go sampling operation met limited success, returning far less material than planned, while an unexpected interaction between autonomous and human-issued commands resulted in the deployed science package MINERVA escaping the system rather than landing as intended [2, 13]. Improved autonomy could help prevent such mishaps while alleviating much of the frequent operational demands upon interplanetary communication systems and human navigators. Additionally, improved mission returns could be obtained by enabling expedient pursuit of unforeseen scientific opportunities in an agile science" paradigm

There are quite a few difficulties for missions to asteroids: their distance from the Earth, their variable or fast rotation rates, irregular shapes, the effect of the disturbing forces of planets and the sun on them. The distance causes problems in active control due to communication delays. Another main obstacle for a mission to asteroids is mapping and analyzing them while staying in an orbit around them. This is required for landing at the right location to extract material for both scientific and mining purposes.² The development of affordable high-end technology for a mission to them is required. This would provide computational reliability and robustness for passive guidance, navigation and control for orbiting and landing on asteroids.

Asteroids are irregular small bodies with weak and noncentral gravity fields. Some are subject to fast spinning and are strongly affected by SRP. As a target for a mission, they have the most perturbed environment and hence the dynamics around them can be unpredictable. Earth-based measurements can provide accurate navigation but there is a time delay involved which could prove to be too large for proximity manoeuvres. This calls for autonomy in precise navigation relative to the small solar system object.

The main problems faced by the GNC system for an asteroid mission are the communication delays due to the large distance between them and Earth and their physical properties like irregular shape and non-uniform high-speed rotation. The gravity fields about them are highly perturbed due to their irregular shape or differentiated composition and very weak. Due to this stable near-circular orbits could turn into crashing or escape orbits in days and this poses a problem. They are greatly subject to perturbations by nearby object approaches and solar radiation pressure (SRP).

1.1. Asteroid Mission Objectives

Asteroids as we can see therefore are of fundamental scientific importance. Missions to asteroids could serve the following objectives:

- **Science:**

Being the remnants of the solar system formation and having their conditions preserved, from their different compositions we can find out the different conditions during the formation respective to their distance from the sun.³

- **Future Resource:**

Asteroids are the closest substantial resource beyond the Earth for scarce materials. Asteroid mining is, therefore, a future objective to quench our needs. These objects are classified based on their spectral type. The C-type, dark and carbon-rich, have phosphorous and other elements required in fertilizers, high abundances of water that could provide for in-situ utilization as rocket propellant. S-types contain significant fractions of iron, nickel and cobalt. They also have a good ratio of rare metals like platinum and gold. M-class asteroids have ten times more metal than the S-types but pose a high cost of mission due to their distance and rarity.⁴

- **Planetary Defence:**

In the past, Earth has been a subject to asteroid impacts. The Lunar and Planetary Laboratory at the University of Arizona provides the fact that Earth has more than three million impact craters larger than 1km

²http://m.esa.int/Our_Activities/Space_Engineering_Technology/Asteroid_Impact_Mission/Planetary_defence; da: 30-09-17

³Refer footnote 8

⁴<https://www.nasa.gov/content/goddard/new-nasa-mission-to-help-us-learn-how-to-mine-asteroids>; da: 01-10-17

in diameter, the largest as we all know being 1000km in diameter. In 2013, an asteroid of mere 20m in diameter sent a shockwave striking six cities across Russia, the Chelyabinsk airburst.⁵ Although rare, larger impacts could lead to major natural catastrophes. NASA and ESA both have been considering the use of space missions for asteroid risk assessments.

1.2. Guidance, Navigation, and Control

The GNC system onboard an SC is responsible for enabling it to carry out the mission objectives as required and with safety. Many factors need to be considered for the development of the GNC system and these differ from mission to mission. In general some of these factors are that the targeted body is itself moving, the gravitational effect of the targeted object as also perturbing bodies, other perturbing forces like solar radiation pressure or atmospheric drag. Communication feasibility with the ground station on Earth also plays a role in this development. As can be seen, the GNC system is a complex development that can successfully combine the effects of the above mentioned factors with available spacecraft technologies to accomplish the mission requirements.

The consideration of these factors leads to a typical SC trajectory, which is plotted and optimized during mission planning. The SC, for any kind of mission, has finite limits on the electrical energy, thrust or propellants. This drives the requirements of efficient and accurate equipment for functions like steering and navigating along the planned path. It also has to maintain stable vehicle attitude while performing the above functions. There are added restrictions on minimum volume and mass making the designing, constructing and testing of such an intricate system an expensive one (Ley, Wittmann, and Hallmann 2011). These functions are achieved by means of a GNC system.

The combination of all the three functions leads to an *integrated guidance, navigation, and control system*. To perform these functions the system must have a reasonably precise knowledge of the acceleration achieved during thrusting and the pointing direction of the SC. Various onboard instruments like gyroscopes, accelerometers, star trackers, horizon sensors, sun-earth sensors, radio navigational aids are used to accomplish the guidance and navigation of the SC. They help provide the position and attitude of the SC then calculate and derive the next set of actions to be taken by the control system. Actuators, like attitude control thrusters, reaction wheels, control moment gyros, aerodynamic surfaces and drag devices are used to control the SC to accomplish the guided path. The architecture and system interactions of the GNC system will be discussed in later chapters along with the specific requirements for this thesis.

The function of the guidance system is to calculate the desired attitude or trajectory of the SC by optimising certain parameters like propellant consumption or time of flight etcetera. It is, therefore, nothing but a mathematical black box, that contains algorithms to compute the desired attitude and rate based on the current mode, time and function of the SC. This desired output is then compared to the actual attitude and rate of the SC provided by the navigation system and the error is computed. The guidance system then generates the required command to correct the attitude which is then received by the control system of the SC. The control system contains the algorithms for controlling manoeuvres which are required a few times during the cruise phase and frequently to maintain stable orbits around asteroids. The control actuators receive the command inputs from the algorithm and are operated to correct the attitude and achieve the desired attitude. The GNC software also includes the orbit dynamics for the Earth, Sun, SC, and asteroid; models of gravity and possible perturbations. The control system makes sure that the spacecraft follows the guidance command in a smooth way that ensures stability of the system despite the presence of disturbances and modelling uncertainties.

Ignorance of the above factors prior to the asteroid rendezvous during the mission make the designing, testing and verification of the onboard GNC system really difficult. Hence active and instantaneous guidance, navigation and control are a necessity of future asteroid missions. Hence the development of autonomous GNC systems has been a prime objective for distant space missions. This involves developing a software that is robust, reliable and efficient. For robustness and reliability, the guidance and control algorithms have to be chosen such that they can provide optimized and converged results every time they are used. A high efficiency of the software is required for high computational speeds since the SC autonomously needs to maintain its attitude and orbit in a perturbed environment.

⁵http://m.esa.int/Our_Activities/Space_Engineering_Technology/Asteroid_Impact_Mission/Planetary_defence; da: 30-09-17

1.3. Dual Quaternions

For GNC the position and the attitude of the SC are represented in different forms: Cartesian, Keplerian or Non-singular parameters. Quaternions and Modified Rodrigues Parameters (MRPs), which are non-singular parameters, have proved to be the best way to achieve an efficient, robust and reliable system so far. Quaternions are four-dimensional vectors based on the Euler theorem representing a point on the Euler axis of rotation and the angle of rotation about the axis in a three-dimensional space. They are popular due to their compactness saving onboard memory and also being singularity free, enabling the transformation of attitude by rotation about the Euler axis. Dual quaternions are a step ahead in the representation of pose (position and attitude) that combines the concept of dual numbers and quaternions. A dual quaternion contains two quaternions, one that represents rotation and the other translation. As can be guessed, the kinematics or dynamics formed with dual quaternions would represent both the translation and rotation of the SC. The easiest way to visualise a dual quaternion is to discern the motion of a screw. When the SC is operated by a dual quaternion, it could be imagined that the SC was being translated and rotated about a particular axis just like the motion of the screw. The mathematics governing dual quaternion operations is discussed in chapter 3. Although being complex to understand their superior compactness compared to quaternions with the kinematic and dynamic equations has increased the interest in them. They also have properties similar to regular quaternions which makes their operations more lucrative. It is however yet to be proven to be computationally more efficient than quaternions by equivalent or analogous comparison and needs further research work to be included as a beneficial non-singular parameter.

1.4. Research Questions

The discussions from the section above lead to three regions of interest, that combine towards a question for immediate future research. Asteroids being the future destination for space missions, need to be studied in situ as well as brought back as samples for further research. Being separated by huge distances from the Earth and having a perturbed environment around them, the GNC system for an asteroid mission needs to be developed to run autonomously and enable the SC to meet its scientific and mission objectives on time in real time. For autonomous GNC, computations need to be faster; with smaller onboard memory utilization and this calls for better and better ways of pose representation. This is where dual quaternions come in the picture. All these lead to the following questions of interest as motivation for research: The research motivation for the literature study and chapters on guidance and control guide us towards the areas that require further research for the GNC systems to advance towards the need for autonomous systems. The following research question would help answer this need.

How can a spacecraft autonomously map an asteroid for feasible landmarks and descend for a touch-and-go sampling process in a robust and optimal fashion whilst being accurate and safe?

In order to answer this question we will address and research the following sub-questions:

- How can the SC attitude and orbital dynamics be represented by dual quaternions?
- What are the cost functions that need to be optimized, the constraints they are subject to and how can they be formulated with dual quaternions?
- How can SBMPO, successive convexification and pseudospectral optimal control methods be implemented to optimize the derived cost functions?
- What are the actuator models that need to be utilized to achieve this control?
- How can we integrate the G&C with the developed subsystem for relative navigation?
- What are methods by which we can verify and validate the GNC system and qualify the system to be accurate, safe and robust?
- Does dual quaternion representation provide better guidance and control as compared to quaternions?
- How useful is this representation and can it be used in real time autonomous applications?

1.5. Report Outline

The report consists of eleven chapters, including the introduction. The organization is chosen such that the required concepts are discussed sequentially to help define the research required for the next topic or chapter. A brief overview of each chapter is discussed below to help the reader understand the gist of the report.

- **Chapter 2**

In this chapter, we discuss all the relevant past and future missions to asteroids, the initial applications of the dual quaternions and the reference mission for the literature study. We will also briefly discuss the top level initial mission requirements to guide the literature study

- **Chapter 3**

In this chapter, we discuss the attitude representation methods used so far and the novel concept of dual quaternions. We discuss the mathematical concept of dual numbers, their arithmetic and how they have been incorporated to represent both position and attitude of the SC. We also discuss the operations that have been established with dual quaternions and some additional benefits from them for consideration during the thesis assignment.

- **Chapter 4**

This chapter discusses all the forces that act on the SC when it is performing its mission and how they perturb it from its desired motion. We also decide on which perturbing forces need to be considered for the thesis assignment and which ones can be left for further work.

- **Chapter 5**

The reference frames required for the asteroid mission, the SC attitude kinematics and dynamics and the orbital dynamics have been discussed in this chapter. A quaternion and dual quaternion representation of them have also been discussed.

- **Chapter 6**

In this chapter, we discuss the instruments required for navigation as well as for guidance. We discuss the state estimator in its quaternion form. We also discuss the results from Razgus (2017) and the conclusions and recommendations from his work.

- **Chapter 7**

In this chapter, we discuss the guidance and control concepts. The presently used problem formulation and the manoeuvring techniques for autonomous spacecraft. We discuss the methods that need further work and development for better autonomous guidance and control of the SC. We discuss the actuator models and their dynamics to be considered during the thesis work. The recent developments in this field have also been shortly discussed. We conclude with the types of guidance and control we would focus and research on during the thesis

- **Chapter 8**

This chapter discusses the type of integrator to be used for SC propagation. Other numerical methods required will be explored during the thesis.

- **Chapter 9**

This chapter discusses the available software to deal with the prescribed mission and the top level architecture to be further built on during the thesis. It also gives a general idea of how the verification and validation of the software would be performed during the thesis.

- **Chapter 10**

In this chapter, we discuss the research question derived from the literature study and how it would be addressed in the thesis. We also provide a timeline to help keep the work on track and ensure timely completion

2

Asteroids and Mission Heritage

The first asteroid flyby was in 1991 by the spacecraft Galileo across the asteroids Gaspra and Ida on its way to Jupiter. Since then there have been a number of missions that have been dedicated to not just flybys but landing on and studying asteroids. There is an increased interest in them in recent years due to the objectives discussed in the previous chapter. In this chapter, we will briefly discuss the small solar system bodies categorized as asteroids and some of the most recent asteroid missions. A brief discussion on relative navigation: a dual quaternion approach (Razgus 2017) will also be presented along with relevant research work done on the combined topics of asteroid missions, dual quaternions and optimized guidance and control.

2.1. Asteroids

According to the new classification by International Astronomical Union (IAU), celestial bodies are classified as planets, dwarf planets, and small solar system bodies. Any object that has a size smaller than Mercury and has enough gravity to hold a spherical shape is classified as a dwarf planet.¹ Subsequently any object not massive enough for its gravity to hold a spherical shape is classified as a small Solar System body. Most of the solar system asteroids fall in this group. Almost one and a half million asteroids are now known with an average separation of greater than 1-3 million km between each other.² Figure 2.1 provides an image of small solar system bodies that have had different spacecraft flyby them or landed on them.

2.1.1. Classification by Location

Asteroids have elliptical orbits around the sun and rotate about themselves. Quite a number of asteroids have been found to have smaller asteroids or moonlets revolving around them. Binary and tertiary systems have also been observed where 2 or 3 similar sized asteroids orbit around each other as a system.³ They are classified depending on their location in the solar system as given below.

Near Earth Objects (NEO)

Asteroids that have orbits with perihelia 1.3 AU causing a close approach with the Earth fall in this category. These attract the much attention due to the danger they pose due to the possibility of collisions with Earth. There are four subcategories: *Amor*, *Apollo*, *Atens* and *Apohele* based on their perihelia(p), aphelia(q) and semi-major axes(a).

- **Amor:** ($1.017 \text{ AU} < p < 1.3 \text{ AU}$) They are outside the Earth's orbit but within Mars's.
- **Apollo:** ($p < 1.017 \text{ AU}$ and $a > 1 \text{ AU}$) They spend most of their time away from the Sun than Earth.
- **Atens:** ($a < 1 \text{ AU}$ and $q > 0.983 \text{ AU}$) They are the Earth-crossing asteroids and spend most of their time closer to the orbit of the Earth.
- **Apohele:** Orbits completely within the Earth's orbit. These asteroids are difficult to detect

NEOs have a short dynamical lifetime of $\leq 10^7$ years and get ejected into space or are tidally or thermally destroyed by the sun. They need to be replenished and their source is the main asteroid belt.

¹<https://www.iau.org/public/themes/pluto>; da: 30-09-17

²<https://solarsystem.nasa.gov/planets/asteroids/indepth>; da: 30-09-17

³<https://solarsystem.nasa.gov/planets/asteroids/indepth>; da: 30-09-17

Main Belt Asteroids (MBA)

The main belt asteroids lie between 2.1 - 3.3 AU from the sun, between Mars and Jupiter. Most asteroids are in this belt. The orbits of these asteroids are a subject to the strong gravitational influence of Jupiter. The giant planet causes perturbations leading to chaotic zones around resonance locations. This can cause the eccentricity of the orbits of the inner belt of asteroids to increase enough to have close approaches to Mars and Earth or even the Sun. They can thereby be removed from orbit by the gravitational interactions or made to collide with terrestrial planets.

Trans-Neptunian Objects (TNO)

As the name suggests these asteroids lie beyond the orbit of Neptune and account for the majority of small bodies in the Solar System. This is also known as the Kuiper belt. According to the IAU's new classification, Pluto and its moon Charon are a part of this belt. They contain the classical Kuiper belt objects that have low eccentricities and the scattered disk objects with high eccentricities.

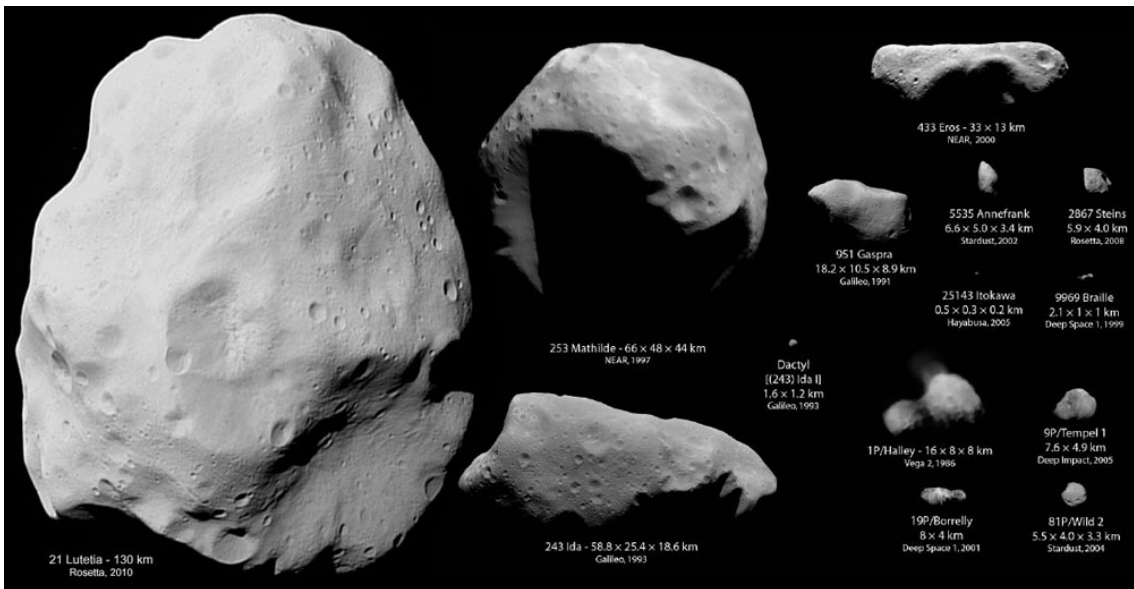


Figure 2.1: Images of small solar system bodies from flyby missions⁴

Trojans

Asteroids that lie in the same orbit as the planet near the Lagrangian points L_4 and L_5 of the planet and the sun are known as Trojan asteroids. These points are approximately 60° ahead and behind the planet known as Greek camp and Trojan camp respectively. Jupiter has the most number of trojans, believed to be almost a million in the count. 6000 of them have been already identified. A few Neptune (17) and Mars (4) trojans have also been found (Sheppard, Jewitt, and Kleyna 2006). Saturn and Uranus are also believed to have trojans based on numerical calculations of the involved orbital dynamics. Earth's first trojan, 2010 TK7 was found in 2011.⁵

Centaurs

Centaurs orbit between the orbits of Jupiter and Neptune and sometimes also have chaotic planet-crossing orbits. Their dynamical lifetime is around $10^6 - 10^8$ years. They are believed to be transitioning from mostly the TNO's scattered disk objects.

Vulcanoids

It is believed that there are asteroids between 0.07 to 0.21 AU from the sun. To date, not a single Vulcanoid has been observed. Even if they exist, being so close to the sun they would be difficult to find. So they remain hypothetical till proven right by observation.

⁴http://www.russianspaceweb.com/spacecraft_small_bodies.html; da: 04-10-17

⁵<http://www.nature.com/nphys/journal/v7/n8/full/nphys2061.html?foxtrotcallback=true>; da: 01-10-17

2.1.2. Classification by Composition

The composition of asteroids as discussed in the previous chapter depends on their distance from the sun. The variation in the undergone thermal processing has led to the existence of a compositionally diverse group of objects. For example, ones that faced higher temperatures have iron centres since it melted and sunk in forcing basaltic lava to surface. Vesta is one such asteroid. They are classified based on their composition as carefully inspected from their spectral images accounting in the space weathering.⁶ The three main types with respect to composition are the C, S and M type.

Carbonaceous C-type

The C-type is the largest class of asteroids; roughly 40% of the known asteroids. These asteroids are dark and have flat spectra. They seem to be made of low-temperature condensates, that have undergone little or no heating. The appearance indicates the presence of clay and silicate rocks.

Stony/S-type

The next largest class of asteroids; around 30-35%, is this one. They are fairly bright and appear to consist of silicates and iron-nickel.

Metallic/M-type

M-type asteroids have spectra that show a composition of nickel-iron embedded in enstatite, which is a magnesium-rich silicate. These asteroids have undergone a melt phase due to substantial thermal processing and could also possibly be cores of disrupted larger asteroids.

D & P-types

D & P-type asteroids do not exhibit any spectral features and could be the most primitive class of asteroids. They appear to be redder than the S-type asteroids and this has been attributed to the possible formation of organic compounds due to space weathering.

Water/W-type

W-type was a reclassification from M-type when many of the larger asteroids ($\geq 30\text{ km}$) showed an absorption band implying the presence of water in the form of hydration.

Vesta/V-type

As said earlier, the asteroid Vesta is one of a kind due to its size, to have a surface covered by basaltic material. Smaller objects in similar orbits to Vesta have been found to have a similar composition. They could have possibly been eroded off from Vesta due to an impact collision.

2.1.3. Properties of Asteroids

The shape of a solid minor body depends on its mass, composition, and temperature. It also depends on its spin rate and tides. Depending on the internal strength of the material and its density, the body has to have a certain minimum radius to be spherical. If the body is composed of silicates then the minimum radius has to be approximately 350 km whereas for a metallic body the minimum radius is merely 100km (Lissauer and Pater 2013). Except for the dwarf planets, asteroids are very irregular in shape. These shapes also depend on collisions and accretion of material leading to abnormal shapes and differentiated compositions. (Holsapple 2001) have proved that such cohesionless bodies can exist in equilibrium with a number of possible shapes at a particular spin rate. The asteroids also undergo changes in their shape due to weathering. The Yarkovsky–O’Keefe–Radzievskii–Paddack effect (YORP) changes the rotation rate of small bodies and are responsible for creating tumbling and binary asteroids hence modifying their heliocentric radial drifts.⁷ As these bodies gain momentum from the YORP torque, their shapes change. Simulations were made for this torque, till landslides occur on the body and the stable shape acquired is like a ‘top’ resembling several such critically tumbling bodies imaged by RADAR (Harris, Fahnestock, and Pravec 2009).

They range from big sizes like Ceres that is around 587 km in diameter to ones that are smaller than 10 m in diameter.⁸ Being less massive they have weak gravity fields. Hence they cannot sustain and do not have atmospheres. Their surface is usually pitted or cratered. The irregularity in shape causes erratic rotation and their gravity field to be perturbed. Due to this a central-gravity field model cannot be used for asteroids. Due

⁶It is the interaction of solar wind particles, solar radiation and cosmic rays with asteroids

⁷https://en.wikipedia.org/wiki/Yarkovsky–O’Keefe–Radzievskii–Paddack_effect; da: 01-10-17

⁸<https://solarsystem.nasa.gov/planets/asteroids/indepth>; da: 01-10-17

to their weak gravitational field forces like gravitational attraction by other celestial bodies, solar radiation and electromagnetic force can perturb them from their Keplerian orbits.

Asteroids have a varied range of spin rates. Mostly they gained angular momentum from collisions (Harris, Fahnestock, and Pravec 2009). Depending on their size, shape, and composition they have an upper limit to their spin rate. If above this limit, the centrifugal force would exceed its self-gravitational force scattering itself in space. It is seen that no small body larger than 100 km in diameter has a rotation rate less than 2 hours. But we do observe smaller bodies rotating with periods as small as 0.0222 hours.⁹ This says that the bigger objects are an aggregate of rocks or differentiated than solid, whereas the smaller bodies being monolith have more tensile strength rather than gravity keeping them together. Spin rates of asteroids are affected by close encounters with planets, the Yarkovsky effect as well as its variant the YORP effect.

2.2. Mission Heritage

Missions to asteroids deal with an uncertain a priori knowledge of the target object; its shape, size, rotation rate, kinematics, orbit dynamics and other factors. This led to the development of autonomous navigation and advanced guidance and control techniques for accurate pointing and landing; serving the mission's science objectives. This section is dedicated to the discussion of some state of the art missions till September 2017 that observed and landed on small solar system bodies. It also discusses certain research work directed towards the utilization of dual quaternions for the development of autonomous guidance and control of space crafts for observing and landing on celestial bodies relevant to asteroid missions.

2.2.1. Asteroid Missions

A few of the most recent asteroid missions are JAXA's Hayabusa and Hayabusa 2, ESA's Rosetta, NASA's DIXI and NASA's Osiris-REx. Hayabusa 2 and Osiris-REx are still ongoing missions, but the onboard GNC strategies used are relevant for the thesis research.

Hayabusa/Hayabusa 2

This was the first sample return mission from an asteroid undertaken by JAXA, launched in May 2003 to the asteroid Itokawa. Hayabusa collected some material from the asteroid surface on its first touchdown but the second attempt faced operational problems. It returned to Earth with the samples in June 2010. Hayabusa 2 is an extension of Hayabusa and was launched in December 2014 to the asteroid Ryugu (1999 JU3). It is expected to arrive at the target in July 2018. It is planned to survey the asteroid for a year and a half and then return back with samples in December 2020. Three sampling touchdowns and a 2 m crater generation by high-speed impact operation have been planned for the proximity operation.

Hayabusa used a multiband imaging camera to image the entire surface of the asteroid whilst its tracking and navigation data provided with a mass and volume estimate of the asteroid (Fujiwara et al. 2006). It had an autonomous onboard guidance and navigation system to touch down on Itokawa since the exact shape, size and surface conditions of the asteroid were unknown. The onboard GNC system consisted of a two axes sun sensor, star tracker and an IRU for attitude determination, an accelerometer and reaction control system with thrusters and reaction wheels for attitude and position control. Figure 2.2 provides the GNC functional block diagram. Navigation was carried out by means of a narrow-angle and wide-angle cameras. for mapping and for regional safety monitoring of surface obstacles. High altitude and low altitude measurements were done by a LIDAR and a laser ranger respectively. The AOCS used the inputs from the cameras, LIDAR, laser ranger and an extended Kalman filter for state estimation. The design of GNC system of Hayabusa 2 is significantly similar to Hayabusa. The instruments for navigation are just upgraded versions as those of Hayabusa. The AOCS consists of two redundantly equipped attitude and orbit control processor units, two star trackers, two IRUs, four accelerometers, four coarse Sun sensors and four reaction wheels (Tsuda, Yoshikawa, Abe, et al. 2013).

Rosetta

ESA's Rosetta was launched in March 2004 to the Comet 67P/Churyumov-Gerasimenko. It performed flybys of asteroid Steins and Lutetia before reaching the comet in August 2014. It mapped the comet from an orbit around it before sending the lander, Philae to its surface. After being in space for more than 12 years Rosetta's mission concluded with it descending on the surface of the comet in September 2016.

⁹<https://web.archive.org/web/20060512060350/http://spaceguard.iasf-roma.inaf.it/tumblingstone/issueSCurrent/eng/ast-day.htm>; da: 01-10-17

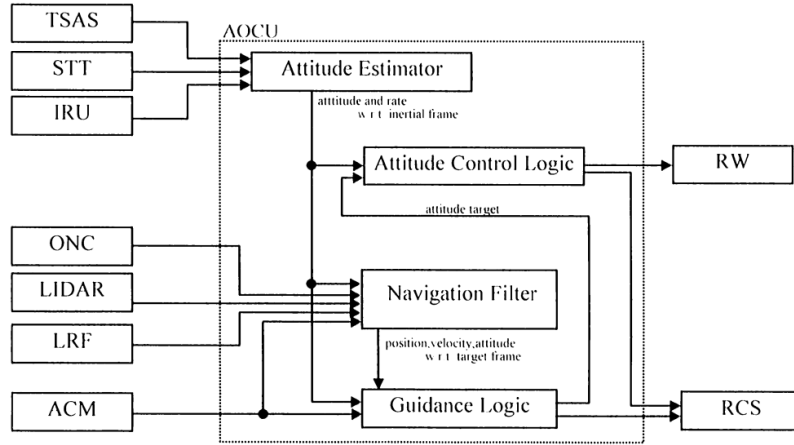


Figure 2.2: Functional Block Diagram of Hayabusa GNC function (Kubota et al. 2006)

Rosetta's GNC system consisted of two pairs of coarse sun sensors, two star trackers, three IMUs with three gyros and accelerometers each and two navigation cameras (NAVCAM) for navigation and for control two sets of twelve thrusters of 10 N each, a bi-propellant system, four-momentum wheels, 1-DOF solar array pointing mechanisms and a 2-DOF antenna pointing mechanism. Similar to Hayabusa, a priori knowledge of the comet kinematics and dynamics was uncertain and hence needed to be obtained in situ during navigation. Radiometric tracking from ground stations of the SC's trajectory using range and Doppler measurements prove insufficient due to this uncertainty and therefore a relative state needed to be measured to improve relative navigation performance. OSIRIS-NAC and NAVCAMS provided optical images to detect the asteroid of interest and deduce the relative trajectory from Rosetta to the centre of the asteroid of interest or to a recognizable feature on its surface. Three separate computer programs were used for orbit determination (OD): first; SC OD using radiometric data only, second; object OD using astrometric data only and third; SC-object relative state estimation using optical measurements of the direction from SC to body centre taking the first two OD solutions (Munoz 2012). For the comet, there were four observational phases to achieve navigation accuracy for the lander delivery phase. Figure 2.3 provides a montage of images by Rosetta during the descent and topple of Philae.

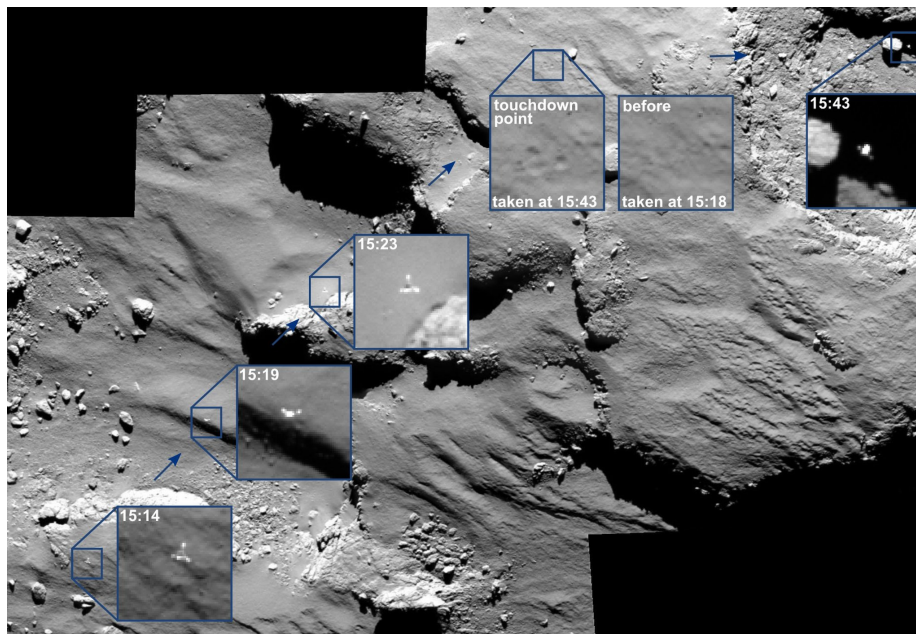


Figure 2.3: Rosetta tracking Philae's descent and topple on Churyumov-Gerasimenko. Image Courtesy: ESA

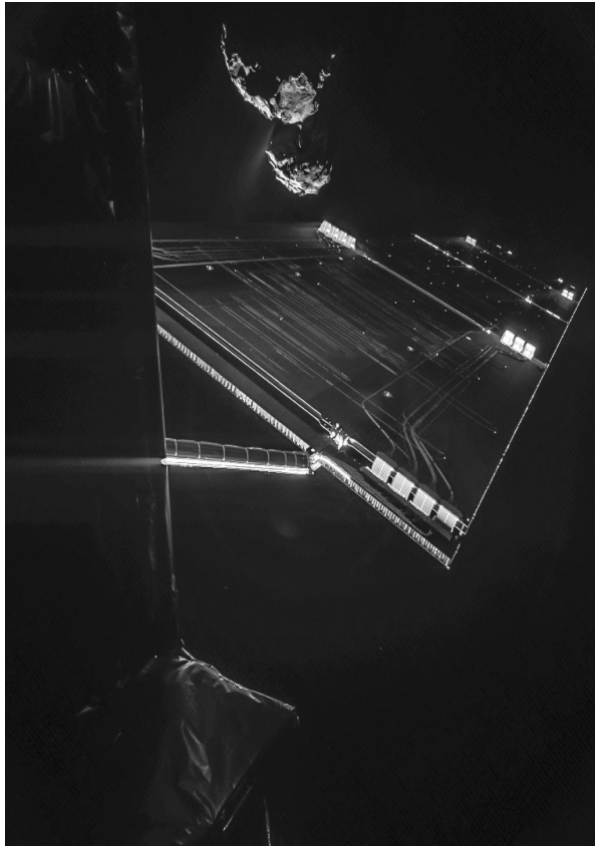


Figure 2.4: Rosetta taking a selfie with Comet Churyumov-Gerasimenko. Image Courtesy: ESA

Deep Impact Extended Investigation (DIXI)

NASA designed a probe to study the composition of the Comet Tempel 1 and launched it in January 2005. DIXI successfully launched an impactor at the nucleus of the comet, ejecting a debris cloud for the first time from a comet's surface. Figure 2.5 elaborates the flyby and impactor trajectories on the encounter.

The flyby SC was equipped with two instruments the High-Resolution Instrument (HRI) combined with a filtered CCD camera and IR spectrometer and the Medium Resolution Instrument (MRI) and the impactor was equipped with Impactor Targeting Sensor (ITS) which is a duplicate of the MRI camera (Hampton et al. 2005). The nucleus was imaged by the flyby SC for days before the impact but its shape was incompletely determined due to its slow rotation period and high speed of the flyby. Observations from the impactor saw numerous outbursts from the surface as expected in the close vicinity of the sun. The impact was near the southern limb of the nucleus and was an oblique one. The flyby SC was made to slow down by 100 m/s and oriented such that it could look back to image the impact. These look-back images helped observe and determine the lateral expansion of the ejecta cone and its ballistic path back to the surface and the local gravitational field of the nucleus respectively.

MRI was used for autonomous navigation during the encounter and HRI in the approach phase by the flyby SC. An S-band antenna was used for communication with the impactor. A three-axis stabilised momentum wheel-based control system along with four RCS thruster hydrazine propulsion for TCMs and momentum dumps was used for its control. The ADCS subsystem estimated and controlled the SC's attitude, rates and linear accelerations with the help of two star trackers and an IRU and provided the information to the AutoNav system to determine the pointing of the navigation camera's boresight (Mastrodemos, Kubitschek, and Synnott 2005). The impactor itself had a three-axis stabilized rate control system (RCS) with four RCS thrusters and an ADCS system with a star tracker and an IRU along with ITS. The AutoNav used a combination of images from the impactor and its attitude telemetry to determine its impact site. A few problems were faced by the impactor when large dust particles hit it and slewed away its pointing but the ADCS subsystem brought it back centring on the impact site.

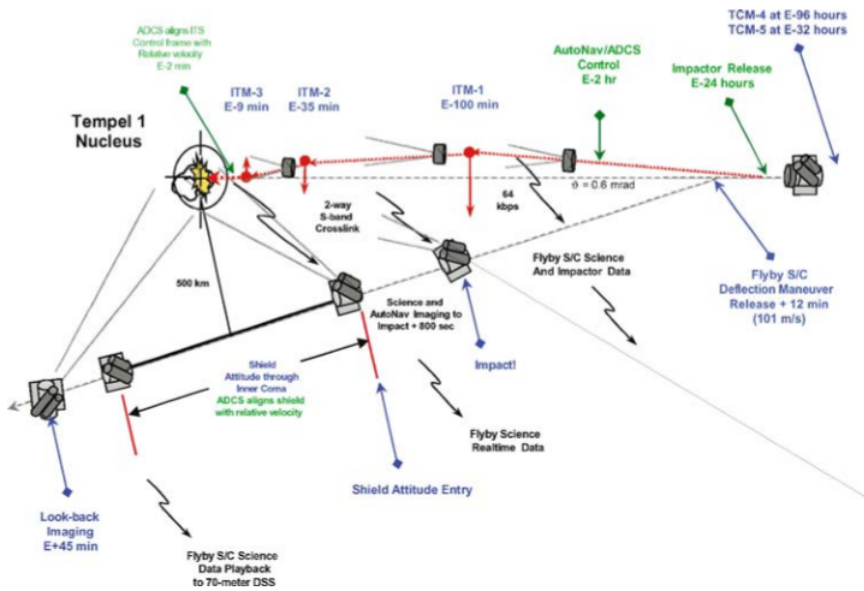


Figure 2.5: Tempel 1 encounter schematic for Deep Impact mission (Mastrodemos, Kubitschek, and Synnott 2005)

OSIRIS-REx

NASA launched the Origins Spectral Interpretation Resource Identification Security - Regolith Explorer (OSIRIS-REx) in September 2016 to the asteroid Bennu. It is presently on a seven-year journey to the asteroid, to study it, obtain samples and return back to Earth. The spacecraft is shown in Figure 2.6. It will rendezvous with the asteroid in late 2018.

As with the above missions, OSIRIS-REx will perform initial characterization of Bennu. Optical navigation will be used to refine Bennu's ephemeris. With a closer approach, the SC will collect higher resolution images (stereophotoclinometry) to construct a shape model and identify landmarks for landing and sample collection. For the above PolyCAM, MapCam, OSIRIS-REx Laser Altimeter (OLA), OTES and OVIRS data will be used.¹⁰ A detailed gravity field will be acquired by radiometric ranging and Doppler tracking using DSN.

The Touch and Go (TAG) operation to collect the sample and back away will also require onboard guidance and navigation. The TAGCAMS have two redundant NavCams for tracking star fields and landmarks on Bennu for SC position determination during mission operations and a StowCam. The TAG sequence is shown in Figure 2.7. NEAR and Hayabusa experiences were used to design a methodical phase approach and low-risk operations so the mission can be stopped at any point and can go back to the previous step. Consultations with ESA led to the implementation of an independent NavCam.



Figure 2.6: The Osiris-REx Spacecraft, Image Courtesy: NASA

¹⁰<http://www.asteroidmission.org/instrumentation/>; da: 07-10-2017

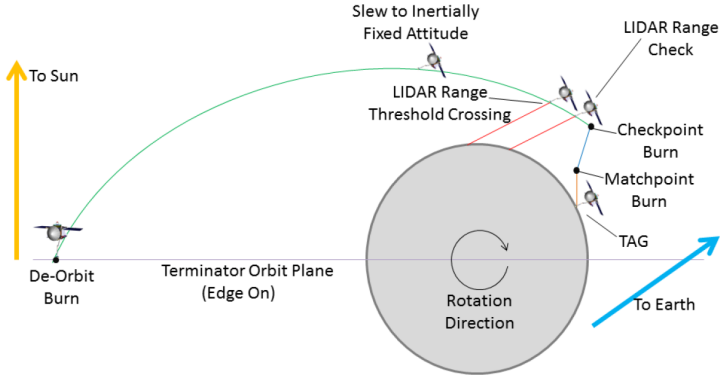


Figure 2.7: The TAG sequence of the Osiris-REx mission (Berry et al. 2013)

2.2.2. Autonomous GNC and Dual Quaternion Research

In the recent years, a lot of work has been done for asteroid missions and they will be used for guidance and reference data during the thesis. There has been a growing interest in dual quaternions and their simplicity of problem representation. Dual quaternions are an upgrade to regular quaternions since they allow the unification of translation and rotation in a single state rather than representation in separate vectors. They provide a concise, singularity free and an unambiguous rigid transform that is also computationally minimalist. Dual quaternions hence enable robustness, efficiency, and ease of use for rigid transformation. Robotics and computer graphics are the two fields where dual quaternions have been worked on the most. Below are the most recent works using DQs, with or without asteroid missions:

- Zhang and Duan 2011 presented a robust finite time manoeuvre using a backstepping control strategy in the Lyapunov for a rigid SC using DQs. The settling time bound was significant in their research to be applicable for real-time application and also a certain control parameter affects both the system response and control input and therefore needs careful selection for desired control.
- Filipe and Tsotras 2013 proposed a nonlinear adaptive position and attitude tracking controller for a rigid body without the requirement of its mass and inertia matrix. Conditions placed on the reference trajectory help the identification of the mass and inertia matrix. The controller is almost asymptotically stable and is capable of handling large error angles and displacements.
- Lee and Mesbahi 2015, Lee and Mesbahi 2017 have worked with DQs for SC rendezvous with a tumbling asteroid and optimal powered descent guidance on Mars with 6 DOF LOS constraints. Their work is based on convex optimisation with piece-wise affine model predictive control (PWA-MPC). Their results show that PWA-MPC may sometimes cause the finite horizon OCP to become infeasible i.e. the required control at a certain time-step might not be available and the computed control may not converge to the origin i.e. the closed loop system is not guaranteed to be asymptotically stable. hence for the stability and feasibility of PWA-MPC additional conditions may be required.
- Kwon, Lee, and Bang 2016 developed a virtual trajectory augmented landing control based on DQs for enabling pinpoint soft landing with a low touchdown velocity for a lunar lander. It introduces a new force-torque sequential control law to resolve the coupling of the main descent thruster and the attitude control thrusters to improve the coupled translational and rotational motion it uses the virtual landing trajectory augmented control law. Simulations show good performance and conformity with the virtual landing trajectory while the attitude is pitched up for the terminal descent.
- Dong et al. 2017 addressed integrated attitude and position control for the final phase of proximity operations of SC rendezvous and docking. They have developed a special DQ based APF to encode motion constraints of the chaser SC and a novel 6 DOF control while complying with these constraints. Stability of the system is ensured through a Lyapunov based method and the effectiveness of this method is proved by numerical simulations.

- Razgus, Mooij, and Choukroun 2017 developed a relative navigation system with quaternion and dual quaternion Kalman filters (QVEKF & DQEKF). Based on the realistic simulations of the environment with typical sensing accuracies it was seen that significant gains in the estimation errors' transients were achieved by the DQEKF compared to QVEKF filter. The DQEKF filter was successful in estimating the relative position and attitude, gyroscope drift and the asteroid angular rates with high accuracy. Its error settling times were lesser by a 1000 s for asteroid rate, relative altitude and relative position and 1500 s for relative velocity than those of QVEKF filter. This results from the coupling of position and velocity using dual quaternions. A similarity between the errors' steady states was found and can be explained by the design models that have similar expressions for linearised position error vector.

Pavone et al. 2014 mention a list of methods to improve the GNC system to make it autonomous and applicable in real-time. Some of these methods have been implemented in the recent years. There are also a few futuristic methods other than those that have been ventured and developed. We discuss the topics that are relevant and need further research below:

- Surovik and Scheeres 2014, Surovik and Scheeres 2017 have proposed a heuristic-guided objective reachability analysis for Non-Keplerian trajectory planning with a receding-horizon control or MPC. The heuristics have been formulated for efficient searching of reachable sets with a complex and finely detailed structure to manage with a scarcity of onboard computing resources. They have examined a heuristic with global search with a combination of simulated annealing and hill climbing to locate sparse regions of the planning domain. The search also satisfies the geometric and timing constraints for the remote sensing objectives for the mission whilst using receding horizon control.
- Mao, Szmuk, and Acikmeşe 2016 have presented an algorithm to solve non-convex optimal control problems via convexification in a successive manner. They have incorporated virtual control and trust regions to guarantee convergence to the optimal solution of the original problem. The advantages of this method are that every limit point in an infinite convergent case will satisfy the optimality condition for the original non-convex optimal control problem and it can be used in real-time path planning for autonomous vehicles.
- Capolupo, Simeon, and Berges 2017 have introduced Sampling-Based Motion Planning (SBMP) and Rapidly-exploring Random Tree (RRT) algorithms for proximity operations and descent on a small solar system body. These methods have provided an efficient exploration of the state space and have enabled construction of a feasible sequence of manoeuvres and trajectories that abide by the constraints of the system. The advantage of these algorithms is the capacity to solve high-level planning problems and guide the SC in a cluttered environment.
- Sagliano 2017 has treated the convex optimization problem with pseudospectral optimal control for powered descent and landing. The flipped Radau and Lobatto families of the pseudospectral methods have been used for this research. The algorithm has been demonstrated for NASA's Mars Science Laboratory. The results show more accurate results when compared with standard transcription methods.

2.3. Research Mission

With the discussion of the mission heritage and the recent research work done, we will design a research mission for this thesis. We will select the target asteroids and define the mission objectives and requirements along with the required assumptions.

2.3.1. Target Asteroids

Selection of the target asteroids needs to be done on the basis of meeting the scientific goals of the intended thesis topic. At the same time sufficient data about the targets must be available for implementing the research on them. To evaluate the developed G&C algorithms for a perturbed environment we require asteroids with irregular shapes and varied rotation rates and sizes. In the reference mission for this thesis (Razgus 2017), the navigation system has been tested on the asteroids Kleopatra and Itokawa and validated for the Comet 67P - Churyumov Gerasimenko. Since there is sufficient data available for these small Solar System bodies, we will use the same for this thesis. The key parameters for these asteroids is given in the Table 2.1.¹¹

¹¹<https://ssd.jpl.nasa.gov/sbdb.cgi>; da: 14/02/18

Table 2.1: Key Parameters of the asteroids Kleopatra, Itokawa and comet 67P

	Kleopatra	Itokawa	67P
Semi-major axis (AU)	2.79	1.32	3.46
Eccentricity	0.25	0.28	0.64
Inclination (deg)	13.11	1.62	7.04
RAAN (deg)	215.36	69.08	50.18
Argument of Perigee (deg)	180.11	162.80	12.69
Mean motion (deg/d)	0.211	0.647	0.153
Size (km)	$217 \times 94 \times 81$	$0.535 \times 0.294 \times 0.209$	$4.1 \times 3.3 \times 1.8$
Mass (kg)	4.64×10^{18}	3.51×10^{10}	9.98×10^{12}
Density (kg/m^3)	6545	1959	532.28
Rotation Period (h)	5.385	12.132	12.761
Rotation Axis $[\lambda; \beta]$ (deg)	[76; 16]	[355; -84]	[65; 59]

2.3.2. Mission Objectives

The main objective of this thesis is to enable an SC to autonomously map and observe a target asteroid and to descend for a sample collection mission. It can be broken down as below:

- The SC should autonomously map the target small solar system body for developing insitu maps for potential landing sites. It should maintain the required attitude and perform maneuvers and corrections autonomously.
- The scientific instruments must be pointed towards the comet for the observational phase of the mission including all proximity maneuvers and also for global mapping.
- The SC should autonomously develop a safe optimal trajectory for a particular landmark based on an a priori perfect knowledge of landmarks from a global mapping phase and perform a descent for a touch and go mission.

2.3.3. Mission Requirements

To understand and develop the concepts required to satisfy the research objective, the mission requirements need to be defined. Using the information received from the mission heritage, we can define the requirements as given below. The individual sensor, actuator requirements are given in the respective chapters of guidance and control, that is chapter five. Detailed requirements during the different phases is discussed in the chapters seven and eight.

- The mission shall include the phases: *mapping* and *descent*.
- The mapping phase shall include high altitude, close observation and asteroid synchronous orbits in the ranges of few kilometers to a few hundreds of metres and the manoeuvres from one orbit to the other.
- The descent phase shall involve the SC following a certain safe optimal trajectory for a particular landmark based on an a priori perfect knowledge of landmarks from a global mapping phase.
- The SC design shall be such that it is applicable to asteroid missions to NEAs or MABs i.e. from 0.9 AU to 3.2 AU approximately and that it can carry out sample collection from the asteroid surface.
- The SC shall have solar arrays and HGA with flexible joints to continuously point towards the Sun and Earth respectively except during the descent phase for safety.
- The SC shall orbit the asteroids Kleopatra and Itokawa to test the guidance and control algorithms and the comet 67P for validation.
- There shall be two guidance and control algorithms based on quaternions and dual quaternions for each of the phases to compare their performance.
- The navigation subsystem shall be used as is from Razgus (2017); with a star tracker, navigation camera, laser ranger and gyroscope with the addition of the sun sensor and accelerometer.

- The control subsystem shall have reaction wheels and reaction thrusters for reactive SC control for low and high thrust operations as needed. (provide min and max thrust level and min resolution for corrections)
- Control and state constraints for the SC motion shall be defined to ascertain desired operation of the SC.
- The GNC system shall meet the pointing requirements and the descent error constraints.

2.3.4. Assumptions

For the feasibility of implementing the guidance and control algorithms certain assumptions need to be made. They are enlisted as follows:

- The guidance problem for both mapping and descent phase are deterministic and the stochastic influences from navigation errors is negligible i.e. ideal/perfect navigation.
- The ephemerides data, polyhedron gravity model and axial tilt of the target body are available.
- The small body rotates about itself with a constant angular velocity with known uncertainties.
- Navigation system provides accurate position and attitude of the SC at all times.
- SC flexible dynamics will be treated in a simplistic manner for representation and can be replaced with better models as future work. (might exclude)
- A priori global maps are available for navigation and landmark identification for the descent and therefore no image processing is done.
- SC considered to be stably injected into required orbit and no tumbling present before mapping or descent phase.
- Control actuators have no mass expulsion disturbance torques.
- Thermal recoil forces on the SC are very small compared to other perturbing forces and hence will not be considered.
- The sun angle with the asteroid will be assumed to be constant for the period of mapping and descent each.

2.4. Conclusion

We discussed the asteroid classes and properties in this chapter along with the successful missions to such small solar system bodies and also some ongoing missions. We also discussed some recent work in the development of GNC algorithms for better computational efficiency for autonomous applications. Based on these, we selected the asteroids Kleopatra and Itokawa for investigation and comet 67P for validation of the guidance and control algorithms developed during this thesis. Also, we equip the SC with the navigation system developed by Razgus (2017) and add control actuators; reaction wheels and thrusters. From the advantages seen in the previous research work guidance and control algorithms based on motion planning and successive convexification will be developed for the mapping and descent phase respectively. These algorithms will be developed with quaternions and dual quaternions and compared to prove the better choice of the two for autonomous systems.

3

Dual Quaternions

Rigid body orientations and translations can be represented by a number of methods, of which the most popular ones are design cosine matrices (DCMs), Euler angles, Euler-eigenaxis rotation, quaternions and Rodrigues parameters. All these methods have their own set of strengths and weaknesses. In this chapter, we discuss these methods in brief, before introducing the dual quaternions. Dual quaternions are an extension to quaternions and provide a tool to help express and analyse physical properties of rigid bodies. They are eight-dimensional numbers that help represent translation and rotation in a single state. They thereby cut down the volume of algebra and make the problem more concise as well as robust and singularity free. We shall introduce dual quaternions and how they can be used to represent rigid transformations in this chapter.

3.1. Dual Numbers

Dual numbers were introduced in 1873 by William Clifford as an extension to real numbers.¹ With the concept of complex numbers adding the imaginary number i , with the property that $i^2 = -1$, he brought forth the element ϵ which has the property of being nilpotent that is $\epsilon^2 = 0$ although $\epsilon \neq 0$. The form of a dual number is analogous to complex numbers and is written as

$$\check{d} = a + b\epsilon \quad (3.1)$$

where, $a, b \in \mathbb{R}$ and ' \check{d} ' represents dual nature of a number and will be used throughout the literature. The number when introduced was used to represent dual angles, which measured the relative position of two skewed lines in three-dimensional space. In d , a represented the angle between the directions of the two lines and b the distance between them. It is actually a special case of one-dimensional algebra later generalized to n dimensions and known as Grassman numbers which are now used as a foundation to define superspace or concepts like supersymmetry. Understanding dual numbers are key to understanding dual quaternions. In Eq. 3.46 a represents the real part of the number and b the dual part.

3.1.1. Dual Numbers Arithmetic Operations

Addition, subtraction, multiplication and division between dual numbers are shown as below (Jia 2013):

$$\check{d}_1 \pm \check{d}_2 = (a_1 \pm a_2) + (b_1 \pm b_2)\epsilon \quad (3.2)$$

$$\check{d}_1 \otimes \check{d}_2 = a_1 a_2 + (a_1 b_2 + b_1 a_2)\epsilon \quad (3.3)$$

$$\frac{\check{d}_1}{\check{d}_2} = \frac{a_1 + b_1\epsilon}{a_2 + b_2\epsilon} = \frac{a_1 + b_1\epsilon}{a_2 + b_2\epsilon} \cdot \frac{a_2 - b_2\epsilon}{a_2 - b_2\epsilon} = \frac{a_1 a_2 + (b_1 a_2 - a_1 b_2)\epsilon}{a_2^2} \quad (3.4)$$

The inverse of a dual number exists as long as $a \neq 0$, given as

$$\check{d}^{-1} = a^{-1}(1 - ba^{-1}\epsilon) \quad (3.5)$$

¹https://en.wikipedia.org/wiki/Dual_number; da: 15-10-2017

A function of a dual number can be defined using Taylor series

$$\begin{aligned} f(a + b\epsilon) &= f(a) + \frac{f'(a)}{1!} b\epsilon + \frac{f''(a)}{2!} b^2 \epsilon^2 + \dots \\ &= f(a) + b f'(a)\epsilon \end{aligned} \quad (3.6)$$

since $\epsilon^2 = 0$ and any higher power of ϵ would be zero. This equation enables to establish a number of functions of dual numbers. The derivative also helps find the tangent to an arbitrary point on a parametric curve which is equal to the normalized dual part of the point (Kenwright 2012).

3.1.2. Dual Vectors

A dual vector, $\check{\mathbf{d}} = (\check{d}_1, \check{d}_2, \check{d}_3)$ consists of three dual numbers \check{d}_1 , \check{d}_2 and \check{d}_3 . The product of a dual vector with a dual number is another dual vector given as follows (Jia 2013):

$$\check{\mathbf{d}}\check{\mathbf{d}} = (\check{d} \otimes \check{d}_1, \check{d} \otimes \check{d}_2, \check{d} \otimes \check{d}_3) \quad (3.7)$$

The inner and outer products of two dual vectors $\check{\mathbf{d}}$ and $\check{\mathbf{e}}$ are similar to those of two normal vectors and are as below (YB Jia, 2013)

$$\check{\mathbf{d}} \cdot \check{\mathbf{e}} = \check{d}_1 \otimes \check{e}_1 + \check{d}_2 \otimes \check{e}_2 + \check{d}_3 \otimes \check{e}_3 \quad (3.8)$$

$$\check{\mathbf{d}} \times \check{\mathbf{e}} = \begin{pmatrix} \check{d}_2 \otimes \check{e}_3 - \check{d}_3 \otimes \check{e}_2 \\ \check{d}_3 \otimes \check{e}_1 - \check{d}_1 \otimes \check{e}_3 \\ \check{d}_1 \otimes \check{e}_2 - \check{d}_2 \otimes \check{e}_1 \end{pmatrix}^T \quad (3.9)$$

These equations will be used ahead for the algebraic operations of dual quaternions.

3.2. Dual Quaternions

Dual Quaternions (DQs) are an extension of dual numbers and quaternions together. They can be used to solve a range of complex problems in a compact and elegant fashion. A rigid transformation is one such problem that can be tackled with dual quaternions. DQs have eight scalar variables that are combined through concatenation (Jia 2013). It helps achieve smooth interpolation between rigid transforms seamlessly and effortlessly. A dual quaternion is of the form

$$\check{\mathbf{q}} = \mathbf{q}_r + \mathbf{q}_d\epsilon \quad (3.10)$$

where,

$$\mathbf{q}_r = q_{r_1} i + q_{r_2} j + q_{r_3} k + q_{r_4} \quad (3.11)$$

$$\mathbf{q}_d = q_{d_1} i + q_{d_2} j + q_{d_3} k + q_{d_4} \quad (3.12)$$

In the above quaternions (\mathbf{q}_r & \mathbf{q}_d), i , j and k are imaginary numbers with properties defined in Eqs. 3.27, 3.28 and 3.29. As per the definition of dual numbers, \mathbf{q}_r represents the real part and \mathbf{q}_d the dual part. It can also be represented as the sum of a dual number and a dual vector:

$$\check{\mathbf{q}} = (q_{r_4} + q_{d_4}\epsilon) + (\mathbf{q}_{r_{1:3}} + \mathbf{q}_{d_{1:3}}\epsilon) \quad (3.13)$$

The DQ can also be written as an 8-tuple vector(YB Jia, 2013)

$$\check{\mathbf{q}} = (\mathbf{q}_r \ \mathbf{q}_d)^T = (q_{r_1}, q_{r_2}, q_{r_3}, q_{r_4}, q_{d_1}, q_{d_2}, q_{d_3}, q_{d_4})^T \quad (3.14)$$

This representation makes the dual quaternion algebraic operations easy to handle and we will use it in the literature study henceforth in this form.

3.2.1. Dual Quaternions Geometric Algebra

The addition and subtraction of DQs can be generalised from the operations of dual numbers:

$$\check{\mathbf{q}}_1 \pm \check{\mathbf{q}}_2 = (\mathbf{q}_{r_1} \pm \mathbf{q}_{r_2}) + (\mathbf{q}_{d_1} \pm \mathbf{q}_{d_2})\epsilon \quad (3.15)$$

In a similar fashion as Eq. 3.48 for dual numbers the multiplication of two DQs can be given as:

$$\check{\mathbf{q}}_1 \check{\otimes} \check{\mathbf{q}}_2 = \mathbf{q}_{r_1} \otimes \mathbf{q}_{r_2} + (\mathbf{q}_{r_1} \otimes \mathbf{q}_{d_2} + \mathbf{q}_{d_1} \otimes \mathbf{q}_{r_2})\epsilon \quad (3.16)$$

$$\check{\mathbf{q}}_2 \check{\odot} \check{\mathbf{q}}_1 = \mathbf{q}_{r_2} \odot \mathbf{q}_{r_1} + (\mathbf{q}_{d_2} \odot \mathbf{q}_{r_1} + \mathbf{q}_{d_1} \odot \mathbf{q}_{r_2})\epsilon \quad (3.17)$$

Using the quaternion product property,

$$\mathbf{q}_1 \otimes \mathbf{q}_2 = \mathbf{q}_2 \odot \mathbf{q}_1 \quad (3.18)$$

We can see that it also applies to the dual quaternion products:

$$\check{\mathbf{q}}_1 \check{\otimes} \check{\mathbf{q}}_2 = \check{\mathbf{q}}_2 \check{\odot} \check{\mathbf{q}}_1 \quad (3.19)$$

We can represent Eq. 3.16 and 3.17 in a matrix form as:

$$\check{\mathbf{q}}_1 \check{\otimes} \check{\mathbf{q}}_2 = \begin{bmatrix} [\mathbf{q}_{r_1} \otimes] & 0_{4 \times 4} \\ [\mathbf{q}_{d_1} \otimes] & [\mathbf{q}_{r_1} \otimes] \end{bmatrix} \begin{pmatrix} \mathbf{q}_{r_2} \\ \mathbf{q}_{d_2} \end{pmatrix} \quad (3.20)$$

$$\check{\mathbf{q}}_2 \check{\odot} \check{\mathbf{q}}_1 = \begin{bmatrix} [\mathbf{q}_{r_2} \odot] & 0_{4 \times 4} \\ [\mathbf{q}_{d_2} \odot] & [\mathbf{q}_{r_2} \odot] \end{bmatrix} \begin{pmatrix} \mathbf{q}_{r_1} \\ \mathbf{q}_{d_1} \end{pmatrix} \quad (3.21)$$

An inverse of the dual quaternion exists if $\check{\mathbf{q}}_r \neq 0$ and is given as

$$\check{\mathbf{q}}^{-1} = \mathbf{q}_r^{-1}(1 - \mathbf{q}_d \mathbf{q}_r^{-1}\epsilon) \quad (3.22)$$

3.2.2. Dual Quaternion Conjugates

DQs can have three possible conjugates, since they have two quaternion elements.

$$\check{\mathbf{q}}^* = \mathbf{q}_r - \mathbf{q}_d\epsilon \quad (3.23)$$

$$\check{\mathbf{q}}^* = \mathbf{q}_r^* + \mathbf{q}_d^*\epsilon \quad (3.24)$$

$$\check{\mathbf{q}}^* = \mathbf{q}_r^* - \mathbf{q}_d^*\epsilon \quad (3.25)$$

Conjugates of the above conjugates in the same fashion gives the DQ itself. As 8-tuples, the above conjugates can be represented in the same order as:

$$\check{\mathbf{q}}^* = (q_{r_1}, q_{r_2}, q_{r_3}, q_{r_4}, -q_{d_1}, -q_{d_2}, -q_{d_3}, -q_{d_4})^T$$

$$\check{\mathbf{q}}^* = (-q_{r_1}, -q_{r_2}, -q_{r_3}, q_{r_4}, -q_{d_1}, -q_{d_2}, -q_{d_3}, q_{d_4})^T$$

$$\check{\mathbf{q}}^* = (-q_{r_1}, -q_{r_2}, -q_{r_3}, q_{r_4}, q_{d_1}, q_{d_2}, q_{d_3}, -q_{d_4})^T$$

Multiplication of the DQ with its conjugates need to be examined in order to realise which conjugate would prove to be useful

$$\begin{aligned} \check{\mathbf{q}} \otimes \check{\mathbf{q}}^* &= (\mathbf{q}_r + \mathbf{q}_d\epsilon)(\mathbf{q}_r - \mathbf{q}_d\epsilon) \\ &= \mathbf{q}_r \otimes \mathbf{q}_r + (\mathbf{q}_d \otimes \mathbf{q}_r - \mathbf{q}_r \otimes \mathbf{q}_d)\epsilon \end{aligned} \quad (3.26)$$

All the cross products in this product cancel out. Since $\mathbf{q}_r \otimes \mathbf{q}_r$ is not scalar and $\mathbf{q}_d \otimes \mathbf{q}_r \neq \mathbf{q}_r \otimes \mathbf{q}_d$, this conjugate multiplication is not really useful and we move to the product of the next conjugate with the DQ.

$$\begin{aligned} \check{\mathbf{q}} \otimes \check{\mathbf{q}}^* &= (\mathbf{q}_r + \mathbf{q}_d\epsilon)(\mathbf{q}_r^* + \mathbf{q}_d^*\epsilon) \\ &= \mathbf{q}_r \otimes \mathbf{q}_r^* + (\mathbf{q}_r \otimes \mathbf{q}_d^* + \mathbf{q}_d \otimes \mathbf{q}_r^*)\epsilon \end{aligned} \quad (3.27)$$

In this case $\mathbf{q}_r \otimes \mathbf{q}_r^*$ is scalar as seen from quaternion multiplication. The dual part of the product also comes out to be scalar once it is expanded and the quaternion products are established.

$$\begin{aligned} \check{\mathbf{q}} \otimes \check{\mathbf{q}}^* &= \|\mathbf{q}_r\|^2 + 2(q_{r_1}q_{d_1} + q_{r_2}q_{d_2} + q_{r_3}q_{d_3} + q_{r_4}q_{d_4})\epsilon \\ &= \|\mathbf{q}_r\|^2 + 2(q_{r_4}q_{d_4} + \mathbf{q}_r \cdot \mathbf{q}_d)\epsilon \end{aligned} \quad (3.28)$$

This shows that this product is nothing but a dual number. If \mathbf{q}_r and \mathbf{q}_d that is the real and dual part of the DQ are orthogonal to each other the dual part of the above result equates to zero. In such a case the

multiplication of the DQ and conjugate will be truly scalar. Moving on to the last kind of product of a DQ and its conjugate:

$$\begin{aligned}\check{\mathbf{q}} \otimes \check{\mathbf{q}}^\diamond &= (\mathbf{q}_r + \mathbf{q}_d \epsilon)(\mathbf{q}_r^* - \mathbf{q}_d^* \epsilon) \\ &= \mathbf{q}_r \otimes \mathbf{q}_r^* + (\mathbf{q}_d \otimes \mathbf{q}_r^* - \mathbf{q}_r \otimes \mathbf{q}_d^*)\epsilon \\ &= \|\mathbf{q}_r\|^2 + 2(q_{r4} \mathbf{q}_{d1:3} - q_{d4} \mathbf{q}_{r1:3} + \mathbf{q}_{r1:3} \times \mathbf{q}_{d1:3})\epsilon\end{aligned}\quad (3.29)$$

This results in a dual quaternion since even though the real part is scalar, it could represent a real quaternion and the dual part represents a pure quaternion.

The conjugates of the the product of two DQs can be proved by mathematical treatment to be the product of the individual conjugates in reverse order.

$$\begin{aligned}(\check{\mathbf{q}} \otimes \check{\mathbf{q}})^* &= \check{\mathbf{q}}^* \otimes \check{\mathbf{q}}^* \\ (\check{\mathbf{q}} \otimes \check{\mathbf{q}})^* &= \check{\mathbf{q}}^* \otimes \check{\mathbf{q}}^* \\ (\check{\mathbf{q}} \otimes \check{\mathbf{q}})^\diamond &= \check{\mathbf{q}}^\diamond \otimes \check{\mathbf{q}}^\diamond\end{aligned}$$

3.2.3. Unit Dual Quaternion

A DQ can be called a unit DQ if it satisfies the condition that its product with the second conjugate is 1.

$$\check{\mathbf{q}} \otimes \check{\mathbf{q}}^* = 1 \quad (3.30)$$

which implies,

$$q_{r1}^2 + q_{r2}^2 + q_{r3}^2 + q_{r4}^2 = 1, \quad (3.31)$$

$$q_{r1} q_{d1} + q_{r2} q_{d2} + q_{r3} q_{d3} + q_{r4} q_{d4} = 0. \quad (3.32)$$

The real part of the DQ must be a unit quaternion and it must be orthogonal to the dual part (quaternion) of the DQ. This also leads to the inverse of the DQ being equal to its conjugate.

$$\check{\mathbf{q}}^{-1} = \check{\mathbf{q}}^* \quad (3.33)$$

The consequence of the conditions in Eqs. 3.74 and 3.75 are that the DOFs are reduced from eight to six, as it should be exactly for a rigid body in 3D.

3.3. Dual Quaternion Attitude and Position Representation

We have discussed all the properties of dual numbers and dual quaternions in the above section. These will be used in this section to establish how they can be used to represent the attitude and position of an SC with respect to a reference frame.

3.3.1. Rigid Displacement

Considering a vector \mathbf{r} rotating and translating through 3D space. The rotation can be taken care of by a rotation matrix C and the translation is equivalent to the vector \mathbf{t} . The vector after displacement can be therefore given by, $\mathbf{r}' = Cr + \mathbf{t}$. Using dual quaternions both these motions can be represented by a dual quaternion. This makes the representation compact and results in easier computation.

The real part and dual part of the DQ are both quaternions. If the dual part is zero that is $\check{\mathbf{q}} = \mathbf{q}_r + 0 \epsilon$ and \mathbf{q}_r is a unit quaternion, the DQ enables 3D rotation with the unit quaternion. This can be proved by using a unit quaternion $\check{\mathbf{p}}$ representing a vector that is to be rotated about the DQ $\check{\mathbf{q}}$.

$$\begin{aligned}\check{\mathbf{q}} \otimes \check{\mathbf{p}} \otimes \check{\mathbf{q}}^\diamond &= \mathbf{q}_r(1 + (p_1 i + p_2 j + p_3 k)\epsilon)\mathbf{q}_r^* \\ &= \mathbf{q}_r \mathbf{q}_r^* + \mathbf{q}_r(p_1 i + p_2 j + p_3 k)\epsilon \mathbf{q}_r^* \\ &= 1 + \mathbf{q}_r(p_1 i + p_2 j + p_3 k)\epsilon \mathbf{q}_r^*\end{aligned}\quad (3.34)$$

The second term can be seen as the operation used in quaternions for rotation and hence it can be proved that a DQ can be used to rotate a vector in 3D. For translation, a unit DQ $\check{\mathbf{q}} = 1 + \mathbf{t}/2 \epsilon$ whose dual part is given by a pure quaternion \mathbf{t} representing the vector of translation can be used to achieve the required motion.

In analogy with quaternions that use half angles for rotation, half of the translation quaternion is used for complete translation (Kavan et al. 2007). Using the same expression as earlier

$$\begin{aligned}\check{\mathbf{q}} \otimes \check{\mathbf{p}} \otimes \check{\mathbf{q}}^\diamond &= \left(1 + \frac{\mathbf{t}}{2} \epsilon\right) \left(1 + (p_1 i + p_2 j + p_3 k) \epsilon\right) \left(1 - \frac{\mathbf{t}^*}{2} \epsilon\right) \\ &= \left(1 + \frac{\mathbf{t}}{2} \epsilon\right) \left(1 - \frac{\mathbf{t}^*}{2} \epsilon\right) + \left(1 + \frac{\mathbf{t}}{2} \epsilon\right) \mathbf{p} \epsilon \left(1 - \frac{\mathbf{t}^*}{2} \epsilon\right) \\ &= 1 + \mathbf{t} \epsilon + \mathbf{p} \epsilon \\ &= 1 + ((p_1 + t_1) i + (p_2 + t_2) j + (p_3 + t_3) k) \epsilon\end{aligned}\quad (3.35)$$

which proves that a unit dual quaternion can be used for translation. Combining the unit dual quaternions for rotation and translation for a single dual quaternion to represent both motions at once:

$$\check{\mathbf{q}} = \left(1 + \frac{\mathbf{t}}{2} \epsilon\right) \mathbf{q}_r = \mathbf{q}_r + \frac{\mathbf{t}}{2} \mathbf{q}_r \epsilon \quad (3.36)$$

$$\check{\mathbf{q}} = \mathbf{q}_r + \mathbf{q}_d \epsilon \quad (3.37)$$

As seen in the section of quaternions, unit quaternions for rotation can be represented using half angles and for translation a vector in Cartesian coordinates:

$$\mathbf{q}_r = \cos \frac{\theta}{2} + \hat{\mathbf{n}} \sin \frac{\theta}{2} \quad (3.38)$$

$$\mathbf{t} = t_1 i + t_2 j + t_3 k \quad (3.39)$$

Using the above quaternions in the DQ established in Eq. 3.80

$$\begin{aligned}\check{\mathbf{q}} &= \mathbf{q}_r + (-\mathbf{t} \cdot \mathbf{q}_r + q_{r4} \mathbf{t} + \mathbf{t} \times \mathbf{q}_r) \frac{\epsilon}{2} \\ \check{\mathbf{q}} &= \cos \frac{\theta}{2} + \hat{\mathbf{n}} \sin \frac{\theta}{2} + \left(-\sin \frac{\theta}{2} (\mathbf{t} \cdot \hat{\mathbf{n}}) + \cos \frac{\theta}{2} \mathbf{t} + \sin \frac{\theta}{2} (\mathbf{t} \times \hat{\mathbf{n}}) \right) \frac{\epsilon}{2}\end{aligned}\quad (3.40)$$

It can be easily proved that the DQ representing both motions is itself a unit quaternion:

$$\begin{aligned}\check{\mathbf{q}} \otimes \check{\mathbf{q}}^* &= \left(\mathbf{q}_r + \mathbf{t} \mathbf{q}_r \frac{\epsilon}{2} \right) \left(\mathbf{q}_r^* + (\mathbf{t} \mathbf{q}_r)^* \frac{\epsilon}{2} \right) \\ &= \mathbf{q}_r \mathbf{q}_r^* + \left(\mathbf{q}_r (\mathbf{t} \mathbf{q}_r)^* + \mathbf{t} \mathbf{q}_r \mathbf{q}_r^* \right) \frac{\epsilon}{2} \\ &= 1 + \left(\mathbf{q}_r \mathbf{q}_r^* \mathbf{t}^* + \mathbf{t} \right) \frac{\epsilon}{2} \\ &= 1 + \left(\mathbf{t}^* + \mathbf{t} \right) \frac{\epsilon}{2} \\ &= 1\end{aligned}\quad (3.41)$$

As discussed in Section 3.3.3, the above product being 1 is the condition for the DQ to be a unit DQ and also the property $\check{\mathbf{q}}^{-1} = \check{\mathbf{q}}^*$ is applicable for the unit DQ. With the above generalizations, the rotation and translation unit quaternions can be figured out from any unit DQ.

Earlier in this section we proved the use of separate unit DQs to rotate and translate a vector. We use the same operation with the combined unit DQ and the vector to get the final DQ after motion.

$$\begin{aligned}\check{\mathbf{q}} \otimes \check{\mathbf{p}} \otimes \check{\mathbf{q}}^\diamond &= \left(\mathbf{q}_r + \mathbf{t} \mathbf{q}_r \frac{\epsilon}{2} \right) (1 + \mathbf{p} \epsilon) \left(\mathbf{q}_r^* - (\mathbf{t} \mathbf{q}_r)^* \frac{\epsilon}{2} \right) \\ &= \mathbf{q}_r \mathbf{q}_r + (\mathbf{q}_r \mathbf{p} \mathbf{q}_r^* + \frac{1}{2} \mathbf{t} \mathbf{q}_r \mathbf{q}_r^* - \frac{1}{2} \mathbf{q}_r \mathbf{q}_r^* \mathbf{t}^*) \epsilon \\ &= 1 + (\mathbf{q}_r \mathbf{p} \mathbf{q}_r^* + \mathbf{t}) \epsilon\end{aligned}\quad (3.42)$$

The above transformation takes care of rotation first and then translation. In case translation is done before rotation the DQ $\check{\mathbf{q}} = \mathbf{q}_r + \mathbf{q}_r \frac{\mathbf{t}}{2} \epsilon$ should be used in the same operation as above which gives the result:

$$\check{\mathbf{q}} \otimes \check{\mathbf{p}} \otimes \check{\mathbf{q}}^\diamond = 1 + \mathbf{q}_r (\mathbf{p} + \mathbf{t}) \mathbf{q}_r^* \epsilon \quad (3.43)$$

For a sequence of transformations on the vector \mathbf{p} :

$$\mathbf{p}' = \check{\mathbf{q}}_n \otimes (\check{\mathbf{q}}_{n-1} \otimes \dots (\check{\mathbf{q}}_1 \otimes \check{\mathbf{p}} \otimes \check{\mathbf{q}}_1^\diamond) \dots \otimes \check{\mathbf{q}}_{n-1}^\diamond) \otimes \check{\mathbf{q}}_n^\diamond \quad (3.44)$$

A single DQ representing all the transformations as $\check{\mathbf{Q}} = \check{\mathbf{q}}_n \otimes \check{\mathbf{q}}_{n-1} \otimes \dots \otimes \check{\mathbf{q}}_2 \check{\mathbf{q}}_1$ is used and hence:

$$\mathbf{p}' = \check{\mathbf{Q}} \otimes \check{\mathbf{p}} \otimes \check{\mathbf{Q}}^\diamond \quad (3.45)$$

Differentiation

For a DQ, differentiation is carried out separately on the real and dual parts:

$$\dot{\check{\mathbf{q}}} = \dot{\mathbf{q}}_r + \frac{1}{2}(\dot{\mathbf{t}}\mathbf{q}_r + \mathbf{t}\dot{\mathbf{q}}_r) \quad (3.46)$$

where, $\dot{\mathbf{q}}_r = \frac{1}{2}\boldsymbol{\omega}\mathbf{q}_r$, $\boldsymbol{\omega}$ being the angular velocity vector and hence a pure quaternion. $\dot{\mathbf{t}} = \mathbf{v}$, where \mathbf{v} is the velocity vector and therefore also a pure quaternion. The differentiation of DQ thus becomes:

$$\dot{\check{\mathbf{q}}} = \frac{1}{2}\boldsymbol{\omega}\mathbf{q}_r + \left(\frac{1}{2}\mathbf{v}\mathbf{q}_r + \frac{1}{4}\mathbf{t}\boldsymbol{\omega}\mathbf{q}_r\right)\epsilon \quad (3.47)$$

3.4. Screw Motion with Dual Quaternions

In the previous sections, we have discussed on how a unit DQ can be used for the representation of the rotational and translational motion of a vector. In this section, we will discuss rigid transformations of lines using DQs. Any rigid displacement is equivalent to screw motion, that is when the rotation is taking place about an axis and/or the object is moving along the axis.

3.4.1. Plücker Coordinates

Plücker coordinates were introduced in geometry in the 19th century by Julius Plücker to assign six homogeneous coordinates to each line in a prospective 3D Euclidean space. In 3D space, a line is determined by the coordinates of two points on the line or by two planes that contain the line. A vector displacement from one distinct point to another distinct point on the line would represent the direction of the line and its magnitude would be nonzero. If a particle moves along this line, it would have a moment about the origin of the reference frame being used.

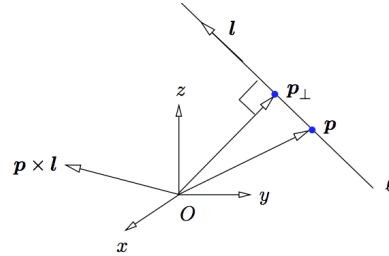


Figure 3.1: Plücker coordinates (Jia 2013)

In Figure 3.1 \mathbf{p} be the position vector of a point on the line with respect to the reference frame and \mathbf{l} be the vector representing the direction of the line. The momentum of an object moving along the line can then be given by a momentum vector: $\mathbf{m} = \mathbf{p} \times \mathbf{l}$. The Plücker coordinates are then given as (\mathbf{l}, \mathbf{m}) . The coordinate \mathbf{m} is independent of the point \mathbf{p} since any point on the line will give the same moment vector. Consider the point \mathbf{p}' on the Figure 3.1. Since it is on the same line as \mathbf{p} , it satisfies the condition $\mathbf{p}' - \mathbf{p} = \lambda\mathbf{l}$ for a certain value of λ . We can prove the independency of \mathbf{m} of the point on the line as follows:

$$\begin{aligned} \mathbf{p}' \times \mathbf{l} &= (\mathbf{p} + (\mathbf{p}' - \mathbf{p})) \times \mathbf{l} \\ &= \mathbf{p} \times \mathbf{l} + (\mathbf{p}' - \mathbf{p}) \times \mathbf{l} \\ &= \mathbf{m} + \lambda\mathbf{l} \times \mathbf{l} \\ &= \mathbf{m} \end{aligned} \quad (3.48)$$

The distance of the line from the origin can simply be given by $\|m\|/\|l\|$. These coordinates are also known as homogeneous coordinates because they are scalable which means that (l, m) and (cl, cm) represent the same line.

When two particular constraints are applied, two variables are lost from the coordinates making the line having four DOFs in space. One of them being that the line is a unit vector ($\|l\| = 1$) and the second being the dot product of the line and moment vector equates to zero ($l \cdot m = l \cdot (p \times l) = 0$). Under these conditions, the moment vector becomes the moment of the line due to a unit force acting on point p on the line in the direction of the unit vector \hat{l} with respect to the origin. Also the magnitude of the moment vector becomes the distance to closest point on the line from the origin. Referring to Figure 3.2 we see that,

$$\begin{aligned} p_{\perp} &= p - p \cos \theta \\ &= (\hat{l} \cdot \hat{l}) - (\hat{l} \cdot p) \hat{l} \\ &= \hat{l} \times (p \times \hat{l}) \\ &= \hat{l} \times m \\ &= m \end{aligned} \quad (3.49)$$

Therefore, $\|p_{\perp}\| = \|m\|$ for a line represented by a unit vector \hat{l} . A line with Plücker coordinates (\hat{l}, m) can be represented by a DQ as:

$$\check{l} = \hat{l} + m \epsilon \quad (3.50)$$

If this line undergoes rigid transformation by rotation and then translation to get a line \check{l}' , a DQ with the required rotation q_r and translation t can be used to achieve it. The DQ for transformation is given as $\check{q} = q_r + t q_r \frac{\epsilon}{2}$.

$$\check{l}' = \check{q} \otimes \check{l} \otimes \check{q}^* \quad (3.51)$$

It is to be noticed that the operation involves the second conjugate as discussed in the subsection conjugates in the section of dual quaternions. It is not the third conjugate as used in the previous transformations in the previous sections due to the difference in the DQ forms of a point and a line (Jia 2013). The operation for transformation yields the following result:

$$\check{l}' = q_r \hat{l} q_r^* + \left(\frac{1}{2} q_r \hat{l} q_r^* t^* + q_r m q_r^* + \frac{1}{2} t q_r \hat{l} q_r^* \right) \epsilon \quad (3.52)$$

The above result can be verified easily and for the proof please refer to Jia 2013 in the references.

3.4.2. Screw Displacement

Mozzi-Chasles' theorem states that any rigid displacement is equivalent to rotation about a certain line called the screw axis, followed or preceded by a translation along the same axis. The screw axis can be represented by the coordinates (\hat{l}, m) . From Figure 3.2, the body is rotated by an angle θ and translated by the vector t . The distance traversed by the body along the direction of the line \hat{l} is given by $d = t \cdot \hat{l}$. The screw motion is thus parameterized by \hat{l} , m , θ and d .

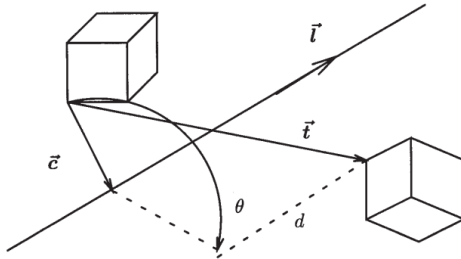


Figure 3.2: The geometry of a screw: every motion can be modeled as a rotation with angle θ about an axis at \vec{c} , with direction \hat{l} and a subsequent translation d along the axis (Daniilidis 1999)

The transformation is performed by the DQ, $\check{q} = q_r + q_d \epsilon$. As can be seen from the Figure 3.2 the rotation axis is the unit vector \hat{l} and the angle of rotation θ , hence

$$q_r = \cos \frac{\theta}{2} + \hat{l} \sin \frac{\theta}{2} \quad (3.53)$$

and

$$\mathbf{q}_d = \frac{1}{2} \mathbf{t} \mathbf{q}_r \quad (3.54)$$

The moment vector has been derived by Daniilidis 1999 and is of the resulting form:

$$\begin{aligned} \mathbf{m} &= \frac{1}{2} \left(\mathbf{t} \times \hat{\mathbf{l}} + \hat{\mathbf{l}} \times (\mathbf{t} \times \hat{\mathbf{l}}) \cot \frac{\theta}{2} \right) \\ &= \frac{1}{2} \left(\mathbf{t} \times \hat{\mathbf{l}} + (\mathbf{t} - d \hat{\mathbf{l}}) \cot \frac{\theta}{2} \right) \end{aligned} \quad (3.55)$$

Multiplying both sides of Eq. 3.96 with $\sin \frac{\theta}{2}$, we get:

$$\begin{aligned} \sin \frac{\theta}{2} \mathbf{m} &= \frac{1}{2} \left((\mathbf{t} \times \hat{\mathbf{l}}) \sin \frac{\theta}{2} + (\mathbf{t} - d \hat{\mathbf{l}}) \cos \frac{\theta}{2} \right) \\ &= \frac{1}{2} \mathbf{t} \cos \frac{\theta}{2} - \frac{d}{2} \hat{\mathbf{l}} \cos \frac{\theta}{2} + \frac{1}{2} (\mathbf{t} \times \hat{\mathbf{l}}) \sin \frac{\theta}{2} \end{aligned} \quad (3.56)$$

Combining Eqs. 3.94, 3.95 and 3.96

$$\begin{aligned} \frac{1}{2} \mathbf{t} \mathbf{q}_r &= \frac{1}{2} \mathbf{t} \left(\cos \frac{\theta}{2} + \hat{\mathbf{l}} \sin \frac{\theta}{2} \right) \\ &= \frac{1}{2} \mathbf{t} \cos \frac{\theta}{2} - \frac{1}{2} \mathbf{t} \cdot \hat{\mathbf{l}} \sin \frac{\theta}{2} + \frac{1}{2} \mathbf{t} \times \hat{\mathbf{l}} \sin \frac{\theta}{2} \\ &= -\frac{d}{2} \sin \frac{\theta}{2} + \sin \frac{\theta}{2} \mathbf{m} + \frac{d}{2} \hat{\mathbf{l}} \cos \frac{\theta}{2} \end{aligned} \quad (3.57)$$

The DQ for transformation now becomes:

$$\begin{aligned} \check{\mathbf{q}} &= \left(\cos \frac{\theta}{2} + \hat{\mathbf{l}} \sin \frac{\theta}{2} \right) + \left(-\frac{d}{2} \sin \frac{\theta}{2} + \sin \frac{\theta}{2} \mathbf{m} + \frac{d}{2} \hat{\mathbf{l}} \cos \frac{\theta}{2} \right) \epsilon \\ &= \left(\cos \frac{\theta}{2} - \frac{d \epsilon}{2} \sin \frac{\theta}{2} \right) + \left(\sin \frac{\theta}{2} (\hat{\mathbf{l}} + \mathbf{m} \epsilon) + \frac{d \epsilon}{2} \cos \frac{\theta}{2} (\hat{\mathbf{l}} + \mathbf{m} \epsilon) \right) \\ &= \left(\cos \frac{\theta}{2} - \frac{d}{2} \sin \frac{\theta}{2} \epsilon \right) + \left(\sin \frac{\theta}{2} + \frac{d}{2} \cos \frac{\theta}{2} \epsilon \right) (\hat{\mathbf{l}} + \mathbf{m} \epsilon) \end{aligned} \quad (3.58)$$

Using the Taylor series for expansion of trigonometric functions of dual numbers from Eq. 3.52

$$\sin \frac{\theta + d \epsilon}{2} = \sin \frac{\theta}{2} + \frac{d}{2} \cos \frac{\theta}{2} \epsilon \quad (3.59a)$$

$$\cos \frac{\theta + d \epsilon}{2} = \cos \frac{\theta}{2} - \frac{d}{2} \sin \frac{\theta}{2} \epsilon \quad (3.59b)$$

The DQ using the above results becomes more compact:

$$\begin{aligned} \check{\mathbf{q}} &= \cos \frac{\theta + d \epsilon}{2} + \sin \frac{\theta + d \epsilon}{2} (\hat{\mathbf{l}} + \mathbf{m} \epsilon) \\ \check{\mathbf{q}} &= \cos \frac{\bar{\theta}}{2} + \bar{\mathbf{l}} \sin \frac{\bar{\theta}}{2} \end{aligned} \quad (3.60)$$

where, $\bar{\theta}$ and $\bar{\mathbf{l}}$ are introduced as dual angle and dual vector. As can be seen this resembles the form of the rotation quaternion. The DQ $\check{\mathbf{q}}$ is a unit DQ which can be proved with conjugate multiplication as done before. This succinct form of DQ enables another property as a definition of powers ($\tau \geq 0$) of the DQ itself.

$$\check{\mathbf{q}}^\tau = \cos \frac{\tau \bar{\theta}}{2} + \bar{\mathbf{l}} \sin \frac{\tau \bar{\theta}}{2} \quad (3.61)$$

This means that with re-multiplication of the line DQ with the same quaternion the rotation can be scaled as many times as the power of the transformation DQ which is intuitive.

3.4.3. Screw Linear Interpolation

Spherical linear interpolation (SLERP) carried out by quaternions for smooth motion between two transforms has been extended to DQ operations as screw linear interpolation (ScLERP). It helps achieve smooth interpolation between rotational and translational transforms. In SLERP, the quaternion for one transformation quaternion to another is achieved by (Kavan et al. 2007):

$$SLERP(\tau; \mathbf{q}_1, \mathbf{q}_2) = \mathbf{q}_1 \otimes (\mathbf{q}_1^* \otimes \mathbf{q}_2)^\tau \quad \tau \in [0, 1] \quad (3.62)$$

Similarly in ScLERP,

$$ScLERP(\tau; \check{\mathbf{q}}_1, \check{\mathbf{q}}_2) = \check{\mathbf{q}}_1 \otimes (\check{\mathbf{q}}_1^* \otimes \check{\mathbf{q}}_2)^\tau \quad \tau \in [0, 1] \quad (3.63)$$

The DQs are represented as:

$$\check{\mathbf{q}}_1 = \mathbf{q}_{r_1} + \frac{1}{2} \mathbf{t}_1 \mathbf{q}_{r_1} \epsilon \quad (3.64)$$

$$\check{\mathbf{q}}_2 = \mathbf{q}_{r_2} + \frac{1}{2} \mathbf{t}_2 \mathbf{q}_{r_2} \epsilon \quad (3.65)$$

The ScLERP operation results in:

$$\begin{aligned} \check{\mathbf{q}}_1^* \otimes \check{\mathbf{q}}_2 &= \left(\mathbf{q}_{r_1}^* + \frac{1}{2} (\mathbf{t}_1 \mathbf{q}_{r_1})^* \epsilon \right) \otimes \left(\mathbf{q}_{r_2} + \frac{1}{2} \mathbf{t}_2 \mathbf{q}_{r_2} \epsilon \right) \\ &= \left(\mathbf{q}_{r_1}^* - \frac{1}{2} \mathbf{q}_{r_1}^* \mathbf{t}_1 \epsilon \right) \otimes \left(\mathbf{q}_{r_2} + \frac{1}{2} \mathbf{t}_2 \mathbf{q}_{r_2} \epsilon \right) \\ &= \mathbf{q}_{r_1}^* \mathbf{q}_{r_2} + \frac{1}{2} \left(-\mathbf{q}_{r_1}^* \mathbf{t}_1 \mathbf{q}_{r_2} + \mathbf{q}_{r_1}^* \mathbf{t}_2 \mathbf{q}_{r_2} \right) \epsilon \\ &= \mathbf{q}_{r_1}^* \mathbf{q}_{r_2} + \frac{1}{2} \left(\mathbf{q}_{r_1}^* (\mathbf{t}_2 - \mathbf{t}_1) \mathbf{q}_{r_2} \right) \epsilon \end{aligned} \quad (3.66)$$

As can be seen the new dual quaternion transforms the DQ from $\check{\mathbf{q}}_1$ to $\check{\mathbf{q}}_2$. Using the screw coordinates and Eq. 3.110 for higher powers of the DQ, we get the ScLERP operation as:

$$ScLERP(\tau; \check{\mathbf{q}}_1, \check{\mathbf{q}}_2) = \left(\mathbf{q}_{r_1} + \frac{1}{2} \mathbf{t}_1 \mathbf{q}_{r_1} \right) \otimes \left(\cos \frac{\tau \bar{\theta}}{2} + \hat{\mathbf{l}} \sin \frac{\tau \bar{\theta}}{2} \right) \quad \tau \in [0, 1] \quad (3.67)$$

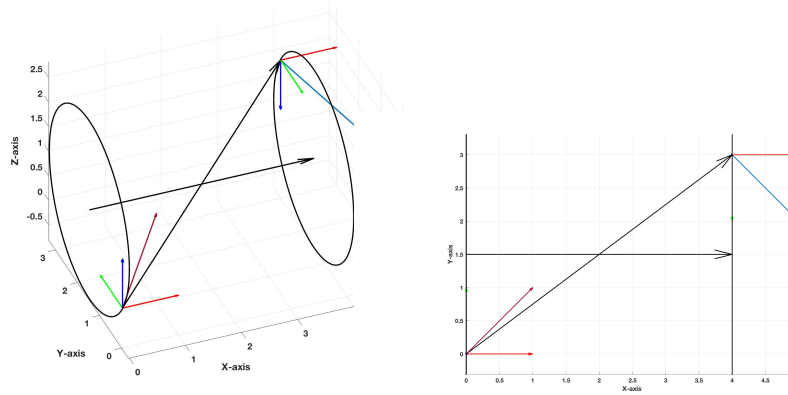
The above result can be further expanded using the Eq. 3.107 to be written in terms of the screw coordinates $\hat{\mathbf{l}}$, \mathbf{m} , θ and d . ScLERP guarantees the shortest path and a constant speed interpolation. This can be seen in the above result since the vector $\hat{\mathbf{l}}$ is independent of the τ times the half dual angle and therefore the screw motion is constant. The angle of rotation as well as the translation both linearly depend on τ , the interpolation parameter. ScLERP is found to be independent of the choice of the coordinate system. For more details about the proof please refer to the work done by Kavan et al. 2007. Therefore ScLERP is analogous to SLERP and does interpolation for rigid transformations whereas the latter does it for rotations.

3.5. DQ Example

In this section we present with a simple example of rotating a vector using DQ cross product from Eq. 3.42. Consider the initial reference frame, A to be located at the origin and the other reference frame, B at $\mathbf{r}_A = [4 \ 3 \ 2]^T$ and to be rotated by 180° about the X-axis giving it the new attitude quaternion, $\mathbf{q}_{B/A} = [1 \ 0 \ 0 \ 0]^T$. Let the vector, $\mathbf{v}_A = [1 \ 1 \ 1]^T$. We need to rotate and translate this vector to be represented in the B frame.

Firstly, we need to construct the DQ for transformation.

$$\begin{aligned} \mathbf{q}_d &= \frac{1}{2} \mathbf{q}_{B/A} \otimes \mathbf{r}_A = \frac{1}{2} \begin{bmatrix} q_4 & q_3 & -q_2 & q_1 \\ -q_3 & q_4 & q_1 & q_2 \\ q_2 & -q_1 & q_4 & q_3 \\ -q_1 & -q_2 & -q_3 & q_4 \end{bmatrix} \begin{pmatrix} r_x \\ r_y \\ r_z \\ 0 \end{pmatrix}; \\ &= \frac{1}{2} \begin{bmatrix} 0 & 0 & 0 & 1 \\ 0 & 0 & 1 & 0 \\ 0 & -1 & 0 & 0 \\ -1 & 0 & 0 & 0 \end{bmatrix} \begin{pmatrix} 4 \\ 3 \\ 2 \\ 0 \end{pmatrix} = \begin{pmatrix} 0 \\ -1 \\ 1.5 \\ -2 \end{pmatrix} \end{aligned}$$



(a) DQ rotation and translation example of a vector

(b) 2D X-Y plane view of the rotated and translated vector

The DQ and its conjugate therefore become

$$\check{q}_{B/A} = \begin{pmatrix} 1 \\ 0 \\ 0 \\ 0 \\ 0 \\ -1 \\ 1.5 \\ -2 \end{pmatrix}, \quad \check{q}_{B/A}^{\diamond} = \begin{pmatrix} -1 \\ 0 \\ 0 \\ 0 \\ 0 \\ -1 \\ 1.5 \\ 2 \end{pmatrix}$$

To get the transformed vector, v_B , we use the operation,

(3.68)

4

Asteroid and Spacecraft Orbital and Attitude Dynamics

This chapter discusses the kinematics and dynamics involved with the motion of the asteroid and the SC. The dynamics of motion deal with the motion of the body caused by forces or moments acting on it. Gravitational forces due to the central body or a perturbing third body, aerodynamic forces of lift and drag due to atmospheres, electromagnetic/radiative forces due to solar pulses or winds act on both the asteroid and SC. Also propulsive forces due to the engine act on the SC. Kinematics provide with the position and attitude of the asteroid or SC with respect to a frame of reference, due to velocities caused by the above-mentioned forces acting on them. Since small solar system bodies do not have an atmosphere or strong magnetic dipoles, the atmospheric drag/lift and magnetic forces will be excluded from the external environment of the SC. The SC is subjected to multiple perturbations due to the irregular gravity field of the small body, solar tides and SRP. In this chapter, we will discuss the kinematics and dynamics of motion; their mathematical representation for the asteroid and SC due to various forces acting on them and the required frames of reference.

4.1. Reference Frames

In order to represent the motions of the asteroid and spacecraft, appropriate frames of reference are required. The reference frames to be used are either pseudo-inertial or non inertial and right-handed. The SC position and attitude can be defined inertially as well as relatively with respect to the target body with the help of these frames. The reference frames help in carrying out operations to help orient the SC towards the target/sun/earth for various mission requirements. The conversions from one frame of reference to another has also been discussed below. Figure 4.3 represents the different reference frames required for the mission.

Heliocentric frame - Ecliptic J2000 (H)

This frame of reference is defined by the ecliptic plane of the Earth. The X axis of the frame is towards the vernal equinox, Z axis along the angular momentum axis of the orbital plane of the Earth and Y axis completes the right-handed set of the system. This frame is a pseudo inertial reference frame.

Asteroid Orbital frame at Pericentre(P)

This frame of reference is fixed to the target rotating body, with centre at the target's centre of mass (com), axes fixed inertially where the Z-axis coincides with its axis of rotation, the X-axis along the nodal line of its orbital plane and Y axis completes the right-handed set. It is, therefore, a non-rotating and non-accelerating frame.

Asteroid Orbital frame (L)

This frame of reference is defined by the orbital plane of the target body. The Kepler elements of this orbit are given with respect to the Heliocentric reference frame. The X axis of this frame is along the direction of motion of the asteroid, Z axis is towards the zenith i.e. always points towards the sun and Y axis completes the right-handed set such that it is along the negative angular momentum axis of the orbital plane. This is a rotating, non-inertial frame of reference.

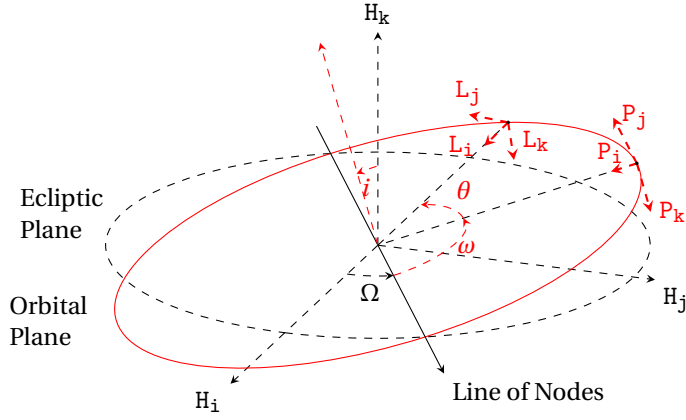


Figure 4.1: Representation of Reference frames

Asteroid Inertial frame (I)

This frame of reference is fixed to the target rotating body, with centre at the target's centre of mass (com), axes fixed inertially where the Z-axis coincides with its axis of rotation, the X-axis along the nodal line of its orbital plane and Y axis completes the right-handed set. It is, therefore, a non-rotating and non-accelerating frame.

Asteroid Rotating frame (A)

This reference frame also has its centre at the target's com but its axes are not inertially fixed and rotate along with the body such that they coincide with the principal moments of inertia of the target, where the Z-axis coincides with its axis of rotation. This is therefore a rotating and non-inertial frame of reference.

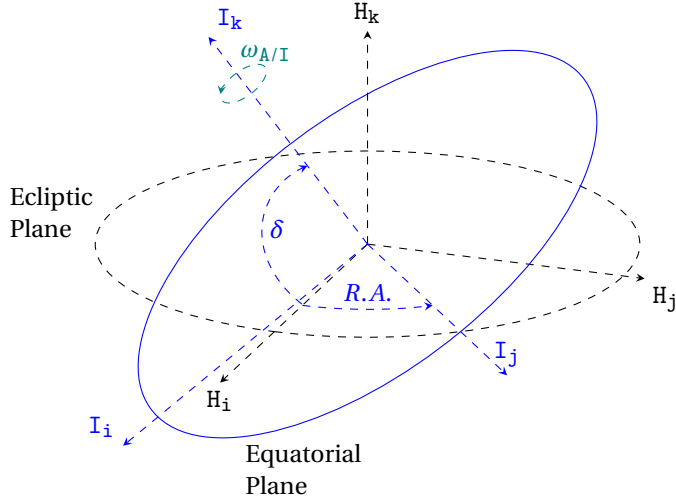


Figure 4.2: Representation of Reference frames

Body reference frame (B)

This reference frame is centred at the com of the SC, with axes along the principal moments of inertia of the SC. Since the SC can change its attitude as required this frame of reference is not inertially fixed and therefore is a non-inertial reference frame.

SC Orbital frame (S)

This frame is the local vertical local horizontal reference frame with its origin at the SC's COM. The Z-axis of this frame is directed towards the asteroid COM or nadir direction, while X-axis is along the direction of motion of the SC about the asteroid and Y-axis completes the right-handed triad such that it is along the orbital angular momentum axis. This is also a non-inertial reference frame since it is not inertially fixed in space.

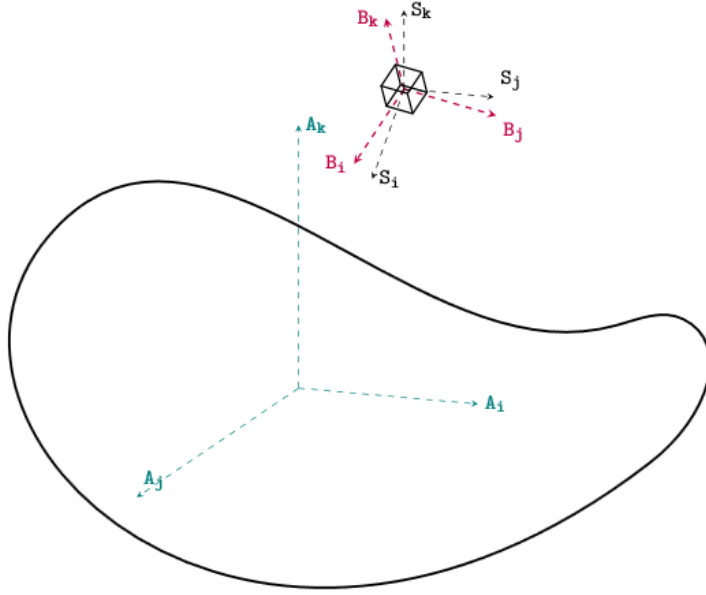


Figure 4.3: Representation of Reference frames

4.2. Attitude Representation Methods

In this section, we will discuss the most common methods of representing the orientation of an SC. We will briefly go through the direction cosine matrices, Euler's Eigenaxis rotation, quaternions and Rodrigues parameters before getting into dual quaternion representation of SC attitude and its transformations.

4.2.1. Direction Cosine Matrices (DCMs) and Euler Angles

A direction cosine matrix or rotation matrix or coordinate transformation matrix as the name suggests is a matrix whose multiplication with a vector rotates the vector whilst preserving its length. The elements of a DCM are the cosines of the unsigned angles between the reference frames that need to be rotated to each other. Consider the asteroid reference frame (A) and the body reference frame (B) as shown in Figure 4.4.

They can be represented respectively in the vector form by their coordinate axes as:

$$\mathbf{a} = \hat{a}_1 + \hat{a}_2 + \hat{a}_3 \quad (4.1)$$

$$\mathbf{b} = \hat{b}_1 + \hat{b}_2 + \hat{b}_3 \quad (4.2)$$

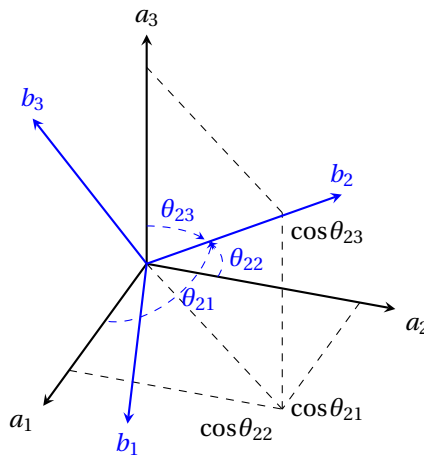


Figure 4.4: Directions Cosines Visualised

The body reference frame in terms of the rotating reference frame can be expressed as follows:

$$\hat{b}_1 = C_{11}\hat{a}_1 + C_{12}\hat{a}_2 + C_{13}\hat{a}_3 \quad (4.3)$$

$$\hat{b}_2 = C_{21}\hat{a}_1 + C_{22}\hat{a}_2 + C_{23}\hat{a}_3 \quad (4.4)$$

$$\hat{b}_3 = C_{31}\hat{a}_1 + C_{32}\hat{a}_2 + C_{33}\hat{a}_3 \quad (4.5)$$

As can be seen from Figure the constants C_{ij} are the cosines of the angles between the axes of frame A with each axis of frame B. Therefore the reference frame B can be given in terms of reference frame A as:

$$\begin{pmatrix} \hat{b}_1 \\ \hat{b}_2 \\ \hat{b}_3 \end{pmatrix} = \begin{bmatrix} C_{11} & C_{12} & C_{13} \\ C_{21} & C_{22} & C_{23} \\ C_{31} & C_{32} & C_{33} \end{bmatrix} \begin{pmatrix} \hat{a}_1 \\ \hat{a}_2 \\ \hat{a}_3 \end{pmatrix} = \begin{bmatrix} \cos \theta_{11} & \cos \theta_{12} & \cos \theta_{13} \\ \cos \theta_{21} & \cos \theta_{22} & \cos \theta_{23} \\ \cos \theta_{31} & \cos \theta_{32} & \cos \theta_{33} \end{bmatrix} \begin{pmatrix} \hat{a}_1 \\ \hat{a}_2 \\ \hat{a}_3 \end{pmatrix} = \mathbf{C}_{B/A} \begin{pmatrix} \hat{a}_1 \\ \hat{a}_2 \\ \hat{a}_3 \end{pmatrix} \quad (4.6)$$

The matrix $\mathbf{C}_{B/A}$ is called the direction cosine matrix and it orthonormal in nature and hence has the following properties:

$$\begin{aligned} \det \mathbf{C}_{B/A} &= 1 \\ \mathbf{C}_{B/A}^{-1} &= \mathbf{C}_{A/B} = \mathbf{C}_{B/A}^T \\ \mathbf{C}_{B/A} \mathbf{C}_{B/A}^T &= I_3 \end{aligned} \quad (4.7)$$

The disadvantage of using a DCM directly is that nine parameters need to be known, where only three are required for rotating the reference frame. Therefore we require six constraints for using a DCM. Euler angle rotation or sequential rotations are used in order to get the DCM without requiring constraints.

To achieve the reference frame B from the frame A, we implement two intermediate frames A' and A'' with orthogonal unit vectors $(\hat{a}'_1 \hat{a}'_2 \hat{a}'_3)$ and $(\hat{a}''_1 \hat{a}''_2 \hat{a}''_3)$ respectively. The sequence is represented as: A → A', A' → A'' and finally A'' → B where the first rotation is about the axis \hat{a}_1 by an angle of θ_3 , then about \hat{a}'_2 by an angle of θ_2 and the end about \hat{a}''_3 by θ_1 . The angles θ_1 , θ_2 and θ_3 are called the Euler angles and the DCMs for these rotations can be given below:

$$\mathbf{C}_{A'/A} = \begin{bmatrix} \cos \theta_3 & \sin \theta_3 & 0 \\ -\sin \theta_3 & \cos \theta_3 & 0 \\ 0 & 0 & 1 \end{bmatrix} \quad (4.8)$$

$$\mathbf{C}_{A''/A'} = \begin{bmatrix} \cos \theta_2 & 0 & -\sin \theta_2 \\ 0 & 1 & 0 \\ \sin \theta_2 & 0 & \cos \theta_2 \end{bmatrix} \quad (4.9)$$

$$\mathbf{C}_{B/A'} = \begin{bmatrix} 1 & 0 & 0 \\ 0 & \cos \theta_1 & \sin \theta_1 \\ 0 & -\sin \theta_1 & \cos \theta_1 \end{bmatrix} \quad (4.10)$$

Combining these sequential rotations gives us the DCM for direct rotation from frame A to frame B by multiplying the three earlier DCMs given by Eqs. 4.8, 4.9 and 4.10 :

$$\begin{pmatrix} \hat{b}_1 \\ \hat{b}_2 \\ \hat{b}_3 \end{pmatrix} = \mathbf{C}_{B/A''} \begin{pmatrix} \hat{a}''_1 \\ \hat{a}''_2 \\ \hat{a}''_3 \end{pmatrix} = \mathbf{C}_{B/A''} \mathbf{C}_{A''/A'} \begin{pmatrix} \hat{a}'_1 \\ \hat{a}'_2 \\ \hat{a}'_3 \end{pmatrix} = \mathbf{C}_{B/A''} \mathbf{C}_{A''/A'} \mathbf{C}_{A'/A} \begin{pmatrix} \hat{a}_1 \\ \hat{a}_2 \\ \hat{a}_3 \end{pmatrix} \quad (4.11)$$

Therefore, $\mathbf{C}_{B/A} = \mathbf{C}_{B/A''} \mathbf{C}_{A''/A'} \mathbf{C}_{A'/A}$. Sequential rotations are not commutative since matrix multiplication is not commutative. Hence they need to be followed in a specific defined order. Considering the three axes of a frame there are 12 possible sequences to achieve a particular orientation. Considering X, Y & Z as the axes, the sequences are: XYZ, XZY, YZX, YXZ, ZYX, ZXY and XYX, XZX, YXY, YZY, ZXZ, ZYZ. The first six are called Tait-Bryan angles and next six are called proper Euler angles.

DCMs using Euler angle rotations are the simplest method of incorporating a rotation between coordinate systems or reference frames and it can also be used for translation, scaling and projection as well. One major disadvantage of this method is the singularities at $\theta_2 = 90^\circ/270^\circ$ and $\theta_2 = 0^\circ/180^\circ$ for the first and second set of sequences respectively at the second axis of rotation. It is known as the gimbal lock and is caused due to infinite angular derivatives at those angles. At these angles one of the two rotated axes replaces the other as it was in its previous orientation. Therefore it is difficult to understand if the SC has achieved the desired new orientation after the rotation.

4.2.2. Euler's Eigenaxis Rotation and Quaternions

A Euler axis or eigenaxis is fixed to the body and is stationary with respect to an inertial frame, that is its orientation relative to the body frame and inertial frame remains unchanged throughout the motion of the SC. Rotating about such an axis an SC can change from its present attitude to any required attitude as shown in Figure 4.5.

Considering the same two axes as before, body reference frame (B) and the inertial reference frame (A) with the Euler axis (\mathbf{e}):

$$\mathbf{e} = e_1 \hat{a}_1 + e_2 \hat{a}_2 + e_3 \hat{a}_3 \quad (4.12)$$

$$= e_1 \hat{b}_1 + e_2 \hat{b}_2 + e_3 \hat{b}_3 \quad (4.13)$$

where e_1, e_2, e_3 are constrained by $e_1^2 + e_2^2 + e_3^2 = 1$. Therefore with DCM it can be represented as Wie 2001:

$$\begin{pmatrix} e_1 \\ e_2 \\ e_3 \end{pmatrix} = \begin{pmatrix} \hat{a}_1 \\ \hat{a}_2 \\ \hat{a}_3 \end{pmatrix} \cdot [\hat{b}_1 \quad \hat{b}_2 \quad \hat{b}_3] \begin{pmatrix} e_1 \\ e_2 \\ e_3 \end{pmatrix} \quad (4.14)$$

Rotating frame A such that \hat{a}_1 aligns with the direction of the axis \mathbf{e} . Now the DCM for this conversion to a new frame A' can be given as:

$$\begin{pmatrix} \hat{a}'_1 \\ \hat{a}'_2 \\ \hat{a}'_3 \end{pmatrix} = \mathbf{C}_{A'/A} \begin{pmatrix} \hat{a}_1 \\ \hat{a}_2 \\ \hat{a}_3 \end{pmatrix} = \begin{bmatrix} e_1 & e_2 & e_3 \\ C_{21} & C_{22} & C_{23} \\ C_{31} & C_{32} & C_{33} \end{bmatrix} \begin{pmatrix} \hat{a}_1 \\ \hat{a}_2 \\ \hat{a}_3 \end{pmatrix} \quad (4.15)$$

Now rotating both frames A and A' about the axis \mathbf{e} by and angle θ , the frame A aligns with frame B whereas frame A' forms a new frame A''. In this situation the relative orientation of A'' to B is the same as A' to A. Therefore, $\mathbf{C}_{A'/A} = \mathbf{C}_{A''/B}$.

$$\mathbf{C}_{B/A} = \mathbf{C}_{B/A''} \mathbf{C}_{A''/A'} \mathbf{C}_{A'/A} = \mathbf{C}_{A'/A}^T \mathbf{C}_{A''/A'} \mathbf{C}_{A''/B} \quad (4.16)$$

Using the values of the DCMs:

$$\mathbf{C}_{B/A} = \begin{bmatrix} \cos \theta + e_1^2(1 - \cos \theta) & e_1 e_2(1 - \cos \theta) + e_3 \sin \theta & e_1 e_3(1 - \cos \theta) - e_2 \sin \theta \\ e_2 e_1(1 - \cos \theta) + e_3 \sin \theta & \cos \theta + e_2^2(1 - \cos \theta) & e_2 e_3(1 - \cos \theta) + e_1 \sin \theta \\ e_3 e_1(1 - \cos \theta) + e_2 \sin \theta & e_3 e_2(1 - \cos \theta) - e_1 \sin \theta & \cos \theta + e_3^2(1 - \cos \theta) \end{bmatrix} \quad (4.17)$$

The DCM can also be represented as:

$$\mathbf{C}_{B/A} = I \cos \theta + (1 - \cos \theta) \mathbf{e} \mathbf{e}^T - [\mathbf{e} \times] \sin \theta \quad (4.18)$$

Using Eqs. 4.15 and 4.17, it can be found that:

$$\mathbf{e} = \begin{pmatrix} e_1 \\ e_2 \\ e_3 \end{pmatrix} = \frac{1}{2 \sin \theta} \begin{pmatrix} C_{23} - C_{32} \\ C_{31} - C_{13} \\ C_{12} - C_{21} \end{pmatrix} \quad (4.19)$$

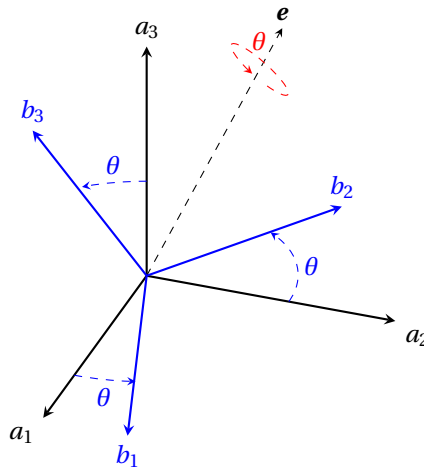


Figure 4.5: Euler's Eigenaxis Rotation

And the angle θ about the Euler axis \mathbf{e} for the rotation of frame A to B can be found by:

$$\cos \theta = \frac{1}{2}(C_{11} + C_{22} + C_{33} - 1) = \frac{1}{2}(\text{tr}C - 1) \quad (4.20)$$

Conversion of the frame obtained from above, that is B to R both with respect to B taken about two Euler axes \mathbf{e}_1 and \mathbf{e}_2 respectively, can be done by:

$$\mathbf{C}_{B/R}(\mathbf{e}, \theta) = \mathbf{C}_{R/A}(\mathbf{e}_2, \theta_2) \mathbf{C}_{B/A}(\mathbf{e}_1, \theta_1) \quad (4.21)$$

The equivalent angle θ with the half angle theorem can be proved to be:

$$\cos \frac{\theta}{2} = \cos \frac{\theta_1}{2} \cos \frac{\theta_2}{2} - \sin \frac{\theta_1}{2} \sin \frac{\theta_2}{2} \cos \gamma \quad (4.22)$$

where, γ is the angle between the two eigenaxes.

The initial introduction of quaternions by Sir William Rowan Hamilton in 1866 brought forward a new compact mathematical representation of concepts like rotation in three dimensions (McDonald 2010). A quaternion represents two things, the three axes about which rotation occurs and the amount of rotation to be done. The general form in which quaternions are expressed is given as:

$$\mathbf{q} = q_1 \mathbf{i} + q_2 \mathbf{j} + q_3 \mathbf{k} + q_4 \quad (4.23)$$

where \mathbf{q} is a quaternion, $q_1, q_2, q_3, q_4 \in \mathbb{R}$ and i, j and k are imaginary numbers having the following properties:

$$ij = k, jk = i, ki = j \quad (4.24)$$

$$ji = -k, kj = -i, ik = -j \quad (4.25)$$

and

$$i^2 = j^2 = k^2 = ijk = -1 \quad (4.26)$$

When Hamilton introduced quaternions, vector notation was yet to be introduced and hence the quaternions we use for attitude analysis are conceptually different. Quaternions can be represented as ordered pairs as follows:

$$\mathbf{q} = \begin{pmatrix} \mathbf{q}_{1:3} \\ q_4 \end{pmatrix} \quad \text{where, } \mathbf{q}_{1:3} = \begin{pmatrix} q_1 \\ q_2 \\ q_3 \end{pmatrix} \quad (4.27)$$

where, $\mathbf{q}_{1:3}$ represents the vector part and q_4 the scalar part. The product of two quaternions as introduced by Hamilton can be given as:

$$\bar{\mathbf{q}}\mathbf{q} = \bar{q}_4 q_4 - \bar{\mathbf{q}}_{1:3} \cdot \mathbf{q}_{1:3} + \bar{q}_4 \mathbf{q}_{1:3} + q_4 \bar{\mathbf{q}}_{1:3} + \bar{\mathbf{q}}_{1:3} \times \mathbf{q}_{1:3} \quad (4.28)$$

The two most important operations with quaternions are a two different products of a pair of quaternions $\bar{\mathbf{q}}$ and \mathbf{q} (Markley and Crassidis 2013):

$$\bar{\mathbf{q}} \otimes \mathbf{q} = \begin{pmatrix} q_4 \bar{\mathbf{q}}_{1:3} + \bar{q}_4 \mathbf{q}_{1:3} - \bar{\mathbf{q}}_{1:3} \times \mathbf{q}_{1:3} \\ \bar{q}_4 q_4 - \bar{\mathbf{q}}_{1:3} \cdot \mathbf{q}_{1:3} \end{pmatrix} \quad (4.29)$$

$$\bar{\mathbf{q}} \odot \mathbf{q} = \begin{pmatrix} q_4 \bar{\mathbf{q}}_{1:3} + \bar{q}_4 \mathbf{q}_{1:3} + \bar{\mathbf{q}}_{1:3} \times \mathbf{q}_{1:3} \\ \bar{q}_4 q_4 - \bar{\mathbf{q}}_{1:3} \cdot \mathbf{q}_{1:3} \end{pmatrix} \quad (4.30)$$

From the above definitions we notice that,

$$\bar{\mathbf{q}} \otimes \mathbf{q} = \mathbf{q} \odot \bar{\mathbf{q}} \quad (4.31)$$

The second product is equivalent to the one Hamilton introduced but the first product is the most used for analysis of the attitude of the SC. It represents a similar composition of rotations as we obtain from a DCM. To achieve a quaternion from quaternions of two different frame conversions say $\mathbf{q}_{B/A}$ and $\mathbf{q}_{A/R}$, the product $\mathbf{q}_{B/A} \otimes \mathbf{q}_{A/R} = \mathbf{q}_{A/R} \odot \mathbf{q}_{B/A}$ results in $\mathbf{q}_{B/R}$. These products can be represented by matrix multiplication:

$$\mathbf{q} \otimes \bar{\mathbf{q}} = [\mathbf{q} \otimes] \bar{\mathbf{q}} = \bar{\mathbf{q}} \odot \mathbf{q} \quad (4.32)$$

$$\mathbf{q} \odot \bar{\mathbf{q}} = [\mathbf{q} \odot] \bar{\mathbf{q}} = \bar{\mathbf{q}} \otimes \mathbf{q} \quad (4.33)$$

where,

$$[\mathbf{q} \otimes] = \begin{bmatrix} q_4 I_3 - [\mathbf{q}_{1:3} \times] & \mathbf{q}_{1:3} \\ -\mathbf{q}_{1:3}^T & q_4 \end{bmatrix} \quad (4.34)$$

$$[\mathbf{q} \odot] = \begin{bmatrix} q_4 I_3 + [\mathbf{q}_{1:3} \times] & \mathbf{q}_{1:3} \\ -\mathbf{q}_{1:3}^T & q_4 \end{bmatrix} \quad (4.35)$$

Here, $[\mathbf{q}_{1:3} \times]$ denotes a cross product matrix. A general vector cross product matrix is shown as:

$$[\mathbf{q}_{1:3} \times] = \begin{bmatrix} 0 & -q_3 & q_2 \\ q_3 & 0 & -q_1 \\ -q_2 & q_1 & 0 \end{bmatrix} \quad (4.36)$$

Quaternions are also known as Euler parameters. Considering the rotation of the Euler eigenaxis \mathbf{n} about an arbitrary axis fixed in both the reference frames I and B by an angle θ , Euler parameters/quaternions can be defined as:

$$\mathbf{q}(\mathbf{n}, \theta) = \begin{pmatrix} \sin \frac{\theta}{2} \mathbf{n} \\ \cos \frac{\theta}{2} \end{pmatrix} \quad (4.37)$$

Since the rotation axis is represented by a unit vector, the quaternion defined by this should have a norm of one i.e. $\|\mathbf{q}\| = 1$ and it is known as a unit quaternion. The Euler's parameters are constrained by the relation:

$$\mathbf{q}^T \mathbf{q} + q_4^2 = q_1^2 + q_2^2 + q_3^2 + q_4^2 = 1 \quad (4.38)$$

Using the above results, the DCM can be parameterized with quaternions as follows:

$$\mathbf{C}(\mathbf{q}, q_4) = (q_4^2 - \|\mathbf{q}_{1:3}\|^2) I_3 - 2q_4 [\mathbf{q}_{1:3} \times] + 2\mathbf{q}_{1:3} \mathbf{q}_{1:3}^T \quad (4.39)$$

$$= \begin{bmatrix} 1 - 2(q_2^2 + q_3^2) & 2(q_1 q_2 + q_3 q_4) & 2(q_1 q_3 - q_2 q_4) \\ 2(q_2 q_1 - q_3 q_4) & 1 - 2(q_1^2 + q_3^2) & 2(q_2 q_3 + q_1 q_4) \\ 2(q_3 q_1 + q_2 q_4) & 2(q_3 q_2 - q_1 q_4) & 1 - 2(q_1^2 + q_2^2) \end{bmatrix} \quad (4.40)$$

Quaternions are restricted by an Euler eigenaxis rotation angle range of $-180^\circ \leq \theta \leq +180^\circ$. This puts a constraint on continuous attitude tracking.

4.2.3. Rodrigues Parameters

Rodrigues parameters came as a solution to the constraint over the range of angles for the Euler-eigenaxis rotation. The initial solution was called the Classical Rodrigues Parameters (CRP). The constraint applied to the fourth element of the quaternion (Schaub and Junkins 2009):

$$q_4 = \sqrt{1 - q_1^2 - q_2^2 - q_3^2} = \cos \frac{\theta}{2} \quad (4.41)$$

With this the CRPs are defined as below:

$$\begin{pmatrix} \tau_1 \\ \tau_2 \\ \tau_3 \end{pmatrix} = \begin{pmatrix} q_1/q_4 \\ q_2/q_4 \\ q_3/q_4 \end{pmatrix} = \begin{pmatrix} e_1 \tan \theta/2 \\ e_2 \tan \theta/2 \\ e_3 \tan \theta/2 \end{pmatrix} \quad (4.42)$$

As can be seen that the above equations contain the holonomic constraint but introduce a singularity at $\theta = \pm 180^\circ$. To remove this the denominator of the CRPs are added by 1 and the singularity moves to $\theta = \pm 360^\circ$ which signifies a full rotation. These new parameters are called Modified Rodrigues Parameters (MRPs).

$$\begin{pmatrix} \sigma_1 \\ \sigma_2 \\ \sigma_3 \end{pmatrix} = \begin{pmatrix} q_1/(1+q_4) \\ q_2/(1+q_4) \\ q_3/(1+q_4) \end{pmatrix} = \begin{pmatrix} e_1 \tan \theta/4 \\ e_2 \tan \theta/4 \\ e_3 \tan \theta/4 \end{pmatrix} \quad (4.43)$$

It is possible to modify the MRPs so that the singularity is shifted even more ahead to something like $\theta = \pm 720^\circ$, but they reintroduce singularities in the kinematic equation at $\theta = \pm 360^\circ$ and also increase the computational load since the kinematics is defined by higher order polynomials and is no longer a simple set off second-order polynomials. Hence MRPs are the present most convenient method of attitude representation. All singularities can be avoided if the shadow parameter technique is employed.

4.2.4. Dual Quaternions

As discussed in the previous section a dual quaternion can be used to transform a vector from one orientation to another. Here we will discuss how that is to be used to for representation of the position and attitude (pose) of an SC. As establish the DQ for transformation is given by, $\check{\mathbf{q}} = \mathbf{q}_r + \mathbf{q}_d \epsilon$. The real part of the DQ represents the attitude of the SC. For the position of the SC, the dual part has to include the position vector in terms of a pure quaternion from the frame of origin to the required frame of transformation.

The DQ has to be a unit quaternion which means it has to have a norm of 1 to represent the pose. There are two constraints that must be met by for the DQ to have a norm of 1:

$$\begin{aligned}\|\mathbf{q}_r\| &= 1 \\ \mathbf{q}_r \cdot \mathbf{q}_d &= 0\end{aligned}$$

The norm of the rotational quaternion should be 1 and the translation and rotational quaternions should be orthogonal to each other. Due to these two constraints, two DOFs are lost and we are left with six parameters out of eight, which is the number of parameters required to represent the pose of a SC.

The SC's orientation is defined with respect to a particular reference frame. If its attitude is represented in a frame B with respect to a frame A, it can be given by the unit quaternion $\mathbf{q}_{B/A}$ and its position vector can be represented with respect to frame B by a pure quaternion \mathbf{r}_B . Hence the DQ for the SC orientation would come together as:

$$\check{\mathbf{q}}_{B/A} = \mathbf{q}_{B/A} + \frac{1}{2} \mathbf{r}_B \otimes \mathbf{q}_{B/A} \epsilon \quad (4.44)$$

To use the position vector with respect to the frame A, we simply need to use the operation for the transformation of quaternions:

$$\mathbf{r}_A = \mathbf{q}_{A/B} \otimes \mathbf{r}_B \otimes \mathbf{q}_{A/B}^* \quad (4.45)$$

Since the rotation quaternions are unit in nature, to get the product for transforming the translation quaternion we multiply the dual part by $\mathbf{q}_{A/B}^* \otimes \mathbf{q}_{A/B} = I_4$, since they are unit quaternions of rotation. Also $\mathbf{q}_{B/A}$ can be written as $\mathbf{q}_{A/B}^*$. Hence we can write Eq. 3.91 as,

$$\begin{aligned}\check{\mathbf{q}}_{B/A} &= \mathbf{q}_{B/A} + \frac{1}{2} \mathbf{q}_{A/B}^* \otimes \mathbf{q}_{A/B} \otimes \mathbf{r}_B \otimes \mathbf{q}_{B/A} \epsilon \\ &= \mathbf{q}_{B/A} + \frac{1}{2} \mathbf{q}_{A/B}^* \otimes \mathbf{q}_{A/B} \otimes \mathbf{r}_B \otimes \mathbf{q}_{A/B}^* \epsilon \\ &= \mathbf{q}_{B/A} + \frac{1}{2} \mathbf{q}_{B/A} \otimes \mathbf{r}_A \epsilon\end{aligned} \quad (4.46)$$

This shows the reversibility of multiplicands in the dual part gives the same DQ with a change in the reference frame of the translation vector. Therefore from any DQ, the rotation and position quaternion can be obtained as:

$$\mathbf{q}_{B/A} = \mathbf{q}_r \quad (4.47)$$

$$\mathbf{r}_B = 2\mathbf{q}_d \otimes \mathbf{q}_r^* \quad (4.48)$$

$$\mathbf{r}_A = 2\mathbf{q}_r^* \otimes \mathbf{q}_d \quad (4.49)$$

4.3. Reference Frame Transformations

In this section we will discuss the conversion of reference frames from one form to another as required during various phases of the mission.

Heliocentric - Asteroid Orbital (H – L)

Initially we convert the H-frame to the asteroid centred frame at the perigee of the orbit P and then this frame is rotated about the the P_z axis by the true anomaly of the asteroid position in the orbit. This gives us the asteroid orbital L-frame. To convert from the H-frame to P-frame, we need a ZXZ rotation sequence with the Euler angles of argument of perigee, inclination of the orbit to the ecliptic and the right ascension of ascending node i.e. $[\omega + \frac{\pi}{2}, i, \Omega]$. Hence a position vector in the P-frame can be given with the help of the DCM matrix $\mathbf{C}_{P/H}$ as:

$$\mathbf{r}_P = \mathbf{C}_{P/H} \mathbf{r}_H \quad (4.50)$$

And the DCM $\mathbf{C}_{P/H}$ can be given as:

$$\begin{pmatrix} P_i \\ P_j \\ P_k \end{pmatrix} = \begin{bmatrix} \cos(\omega + \frac{\pi}{2})\cos\Omega - \sin(\omega + \frac{\pi}{2})\sin\Omega\cos i & \cos(\omega + \frac{\pi}{2})\sin\Omega + \sin(\omega + \frac{\pi}{2})\cos\Omega\sin i & \sin(\omega + \frac{\pi}{2})\sin i \\ -\sin(\omega + \frac{\pi}{2})\cos\Omega - \cos(\omega + \frac{\pi}{2})\sin\Omega\cos i & -\sin(\omega + \frac{\pi}{2})\sin\Omega + \cos(\omega + \frac{\pi}{2})\cos\Omega\cos i & \cos(\omega + \frac{\pi}{2})\sin i \\ \sin\Omega\sin i & -\cos\Omega\sin i & \cos i \end{bmatrix} \begin{pmatrix} H_i \\ H_j \\ H_k \end{pmatrix} \quad (4.51)$$

The DCM can be converted to the rotation quaternion $\mathbf{q}_{P/H}$ with the help of the Eq. 4.40. and the frame conversion from the P-frame to the L-frame:

$$\mathbf{q}_{L/H} = \mathbf{q}_{L/P} \otimes \mathbf{q}_{P/H} = \mathbf{q}(P_k, \theta) \otimes \mathbf{q}_{P/H} \quad (4.52)$$

where, θ is the true anomaly of the asteroid and therefore this quaternion needs to be updated with time as the asteroid orbits the sun.

Heliocentric - Asteroid Inertial (H – I)

The orientation of the asteroid rotation axis or in other words its axial tilt is given by the right ascension, λ and declination, β from the H-frame. Hence it can be directly transformed from the heliocentric frame. Since this is a non-rotating inertial frame, it can be obtained directly from the P-frame. A sequence of rotations, first about the k -axis of the P-frame by the right ascension and then about the i -axis of the transformed frame by the

$$\mathbf{q}_{I/H} = \mathbf{q}(I_i, \beta) \otimes \mathbf{q}(H_k, \lambda) \quad (4.53)$$

Asteroid Inertial - Asteroid Rotating (I – A)

Transforming from the inertial frame to the rotating frame is simply the rotating the inertial frame about its K -axis at the rotation rate of the asteroid.

$$\mathbf{q}_{A/I} = \mathbf{q}(I_k, (\omega_{A/I} t)) \quad (4.54)$$

Heliocentric - Asteroid Rotating (H – A)

This transformation can simply be obtained from the previous two transformations as follows:

$$\mathbf{q}_{A/H} = \mathbf{q}(I_k, (\omega_{A/I} t)) \otimes \mathbf{q}(I_i, \beta) \otimes \mathbf{q}(H_k, \lambda) \quad (4.55)$$

Asteroid Inertial - SC orbital (I – S)

Similar to the transformation from heliocentric to asteroid orbital frame the transformation from I-frame to S-frame can be carried out with the Euler angles $[\omega_S + \frac{\pi}{2}, i_S, \Omega_S]$.

$$\begin{pmatrix} S_P_i \\ S_P_j \\ S_P_k \end{pmatrix} = \begin{bmatrix} \cos(\omega_S + \frac{\pi}{2})\cos\Omega_S - \sin(\omega_S + \frac{\pi}{2})\sin\Omega_S\cos i_S & \cos(\omega_S + \frac{\pi}{2})\sin\Omega_S + \sin(\omega_S + \frac{\pi}{2})\cos\Omega_S\sin i_S & \sin(\omega_S + \frac{\pi}{2})\sin i_S \\ -\sin(\omega_S + \frac{\pi}{2})\cos\Omega_S - \cos(\omega_S + \frac{\pi}{2})\sin\Omega_S\cos i_S & -\sin(\omega_S + \frac{\pi}{2})\sin\Omega_S + \cos(\omega_S + \frac{\pi}{2})\cos\Omega_S\cos i_S & \cos(\omega_S + \frac{\pi}{2})\sin i_S \\ \sin\Omega_S\sin i_S & -\cos\Omega_S\sin i_S & \cos i_S \end{bmatrix} \begin{pmatrix} I_i \\ I_j \\ I_k \end{pmatrix} \quad (4.56)$$

The DCM can be converted to the rotation quaternion $\mathbf{q}_{P/H}$ with the help of the Eq. 4.40. and the frame conversion from the S_P -frame to the S-frame:

$$\mathbf{q}_{S/I} = \mathbf{q}_{S/S_P} \otimes \mathbf{q}_{S_P/I} = \mathbf{q}(S_P_k, \theta_S) \otimes \mathbf{q}_{S_P/I} \quad (4.57)$$

where, θ_S is the true anomaly of the SC.

Asteroid Rotating - SC orbital (A – S)

The S - frame can be obtained from the A - frame as given in Eq. 4.58

$$\mathbf{q}_{S/A} = \mathbf{q}_{S/I} \otimes \mathbf{q}_{I/A} = \mathbf{q}_{S/I} \otimes \mathbf{q}_{A/I}^* = \mathbf{q}_{S/I} \otimes \mathbf{q}^*(I_k, (\omega_{A/I} t)) \quad (4.58)$$

SC orbital - Body reference (S – B)

The orientation of the body reference frame of the SC is calculated with the help of the navigation system and then it can be obtained with respect to the SC orbital reference frame. The attitude controller is used to achieve the required orientation of the SC (B - frame) as per the mission objectives. The transformation can simply be given with DCM as given in Eq.4.59 and Eq. 4.40 can be used to get the quaternion, $\mathbf{q}_{B/S}$ from it.

$$\begin{pmatrix} B_i \\ B_j \\ B_k \end{pmatrix} = \begin{bmatrix} \cos \theta_{11} & \cos \theta_{12} & \cos \theta_{13} \\ \cos \theta_{21} & \cos \theta_{22} & \cos \theta_{23} \\ \cos \theta_{31} & \cos \theta_{32} & \cos \theta_{33} \end{bmatrix} \begin{pmatrix} S_i \\ S_j \\ S_k \end{pmatrix} \quad (4.59)$$

Asteroid Rotating - Body reference (A – B)

Using the quaternions $\mathbf{q}_{B/S}$ and $\mathbf{q}_{S/A}$ given in Eqs. 4.58 and 4.59 the required quaternion $\mathbf{q}_{B/A}$ can be obtained for operating the SC as per the mission objectives and requirements.

$$\mathbf{q}_{B/A} = \mathbf{q}_{B/S} \otimes \mathbf{q}_{S/A} = \mathbf{q}_{B/S} \otimes \mathbf{q}_{S/I} \otimes \mathbf{q}^*(I_k, (\omega_{A/I} t)) \quad (4.60)$$

4.4. Translational Motion (Orbital Motion)

Once the SC has been transferred to its operational orbit, it must be maintained in the orbit with certain accuracy to carry out the different scientific objectives. The maintaining of the orbit needs to be done at minimum or acceptable expenditure of propellant. Assuming that the SC has an appropriate mass that does not affect the motion of the small body it orbits, we can establish its equation of motion.

Due to the presence of perturbing forces, the orbital motion cannot be characterized as Keplerian and is an evolving orbit called an osculating orbit. The equation of the orbital motion of the SC about the small body in the inertial frame fixed to the COM of the small body can, therefore, be given as (Sidi 1997):

$$\ddot{\mathbf{r}}_{B/I}^I = \mathbf{a}_{GG} + \mathbf{a}_D \quad (4.61)$$

where, as established in the earlier chapters, \mathbf{a}_{GG} and \mathbf{a}_D are the accelerations due to the polyhedron gravity field and the perturbing forces caused by the 3rd body perturbation of the sun and the solar radiation pressure in the inertial frame of reference. The perturbing accelerations are appreciably smaller than the gravitational acceleration. Newton's laws hold true for inertial frames and therefore we need to define the equations of motions based on them in inertial frames. We will establish all the dynamics of motion involved in the inertial frame. This also makes it easier to program and debug it.

4.4.1. Kinematics

The kinematic equation for the translational motion of the SC in the inertial frame can be written as (Razgus, Mooij, and Choukroun 2017):

$$\dot{\mathbf{r}}^I = \mathbf{v}_{B/I}^I \quad (4.62)$$

where \mathbf{r} , \mathbf{v} , \mathbf{g} and \mathbf{a}_D are the position, velocity, gravitational acceleration and perturbing acceleration due to disturbing non-gravitational forces with respect to the inertial frame respectively.

4.4.2. Dynamics

The dynamic motion of the SC can be given by:

$$m\ddot{\mathbf{v}}_{B/I}^I = \mathbf{F}^I \quad (4.63)$$

$$\ddot{\mathbf{v}}_{B/I}^I = \mathbf{a}_{GG}^I + \mathbf{a}_D^I \quad (4.64)$$

where m and F_I are the mass of the SC and total force acting on the SC with respect to the inertial frame respectively.

4.5. Rotational Motion

In this section, we will discuss the concepts of angular velocity or angular rate vector and present the kinematics and dynamics of the rotational motion of the SC about itself or the body reference frame. Quaternion representation of the kinematics and attitude dynamics are advantageous as compared to DCMs since they involve lesser multiplications and to Rodrigues parameters and modified Rodrigues parameters by not resulting in bulky expressions (Razgus 2017).

4.5.1. Kinematics

The angular velocity of the body frame with respect to the inertial frame ($\omega^{B/I}$) can be given by the equation below. Let $\omega_1, \omega_2, \omega_3$ be the components of the angular velocity of the spacecraft in the body reference frame.

$$\omega_{B/I}^B = \omega_1 \mathbf{b}_1 + \omega_2 \mathbf{b}_2 + \omega_3 \mathbf{b}_3 = [\mathbf{b}_1 \quad \mathbf{b}_2 \quad \mathbf{b}_3] \begin{pmatrix} \omega_1 \\ \omega_2 \\ \omega_3 \end{pmatrix} \quad (4.65)$$

The kinematic differential equation in terms of Euler angles is given as (Wie 2001):

$$\begin{pmatrix} \dot{\theta}_1 \\ \dot{\theta}_2 \\ \dot{\theta}_3 \end{pmatrix} = \frac{1}{\cos\theta_2} \begin{bmatrix} \cos\theta_2 & \sin\theta_1\sin\theta_2 & \cos\theta_1\sin\theta_2 \\ 0 & \cos\theta_1\cos\theta_2 & -\sin\theta_1\cos\theta_2 \\ 0 & \sin\theta_1 & \cos\theta_1 \end{bmatrix} \begin{pmatrix} \omega_1 \\ \omega_2 \\ \omega_3 \end{pmatrix} \quad (4.66)$$

The kinematic equation using Euler angles becomes singular when $\theta_2 = \pi/2$. It can also be represented as (Markley and Crassidis 2013):

$$\dot{\mathbf{C}}_{B/I} = -[\boldsymbol{\omega}_{B/I}^B \times] \mathbf{C}_{B/I} \quad (4.67)$$

where $\mathbf{C}_{B/I}$ is the attitude matrix of the body frame with respect to the inertial frame of reference. Using quaternions we have described the DCM matrix in Eq. (3.36). Using that the kinematics equation can be written as:

$$\dot{\mathbf{q}}_{B/I} = \frac{1}{2} \boldsymbol{\omega}_{B/I}^B \otimes \mathbf{q}_{B/I} = \frac{1}{2} \boldsymbol{\Omega}(\boldsymbol{\omega}_{B/I}^B) \mathbf{q}_{B/I} \quad (4.68)$$

where $\boldsymbol{\Omega}$ is expressed as:

$$\boldsymbol{\Omega} = \begin{bmatrix} -[\boldsymbol{\omega} \times] & \boldsymbol{\omega} \\ -\boldsymbol{\omega}^T & 0 \end{bmatrix} = \begin{bmatrix} 0 & \omega_3 & -\omega_2 & \omega_1 \\ -\omega_3 & 0 & \omega_1 & \omega_2 \\ \omega_2 & -\omega_1 & 0 & \omega_3 \\ -\omega_1 & -\omega_2 & -\omega_3 & 0 \end{bmatrix} \quad (4.69)$$

As can be seen the kinematic equation with quaternions is in a linear relationship with the quaternion itself and does not have any trigonometric functions. It hence provides a less cumbersome and more appealing way of attitude representation.

4.5.2. Attitude Dynamics

The rotational equation of a rigid body about the origin of the inertial frame can be given as:

$$\int \mathbf{r}_B \times \ddot{\mathbf{r}}_I dm = \mathbf{T}_B \quad (4.70)$$

where, \mathbf{r}_B and \mathbf{r}_I are the position vectors of the SC with respect to the body frame and the inertial frame of reference respectively, m is the mass of the SC and \mathbf{T}_B is the sum of all torques acting on the SC: disturbance and control torques. This equation can be further resolved and be written as (Wie 2001):

$$\dot{\mathbf{H}}_B + \boldsymbol{\omega}_{B/I}^B \times \mathbf{H}_B = \mathbf{T}_B \quad (4.71)$$

where, \mathbf{H}_B is the absolute angular momentum of the body about the origin of the body reference frame and \mathbf{r}_{c_B} is the position vector of the COM of the SC with respect to the body reference frame. The inertia matrix of the SC about the body-fixed reference frame can be given as:

$$\mathbf{J} = \begin{bmatrix} J_{11} & J_{12} & J_{13} \\ J_{21} & J_{22} & J_{23} \\ J_{31} & J_{32} & J_{33} \end{bmatrix} \quad (4.72)$$

Substituting $\mathbf{H}_B = \mathbf{J}\boldsymbol{\omega}_{B/I}^B$ and Eq. (5.11) in Eq. (5.10), the rotational equations of motion or dynamics of the SC can be given as:

$$\mathbf{J}\dot{\boldsymbol{\omega}}_{B/I}^B + \boldsymbol{\omega}_{B/I}^B \times \mathbf{J}\boldsymbol{\omega}_{B/I}^B = \mathbf{T}^B = \mathbf{T}_C^B + \mathbf{T}_D^B \quad (4.73)$$

where, \mathbf{T}_{C_B} and \mathbf{T}_{D_B} are the control and disturbance torques respectively.

4.6. Asteroid Dynamics

Depending on the requirement of simulation time, the orbit of the asteroid around the sun might be needed or not. For a short duration of simulation, this movement can be assumed to be negligible. The angular velocity of the asteroid is assumed to be constant in both direction and magnitude, without the presence of precession and nutation of the rotation axis. The angular velocity of the asteroid with respect to the inertial frame of reference can be given as:

$$\boldsymbol{\omega}_{A/I}^A = \text{constant} \quad (4.74)$$

Kinematics of the asteroid can be given in a similar fashion as the SC kinematics:

$$\dot{\mathbf{q}}_{A/I} = \frac{1}{2} \boldsymbol{\Omega}(\boldsymbol{\omega}_{A/I}^A) \mathbf{q}_{A/I} \quad (4.75)$$

4.7. Relative Dynamics and Kinematics

The kinematics and dynamics discussed above are all in the inertial frame of reference. The navigation filter in Razgus, Mooij, and Choukroun 2017 deals with relative states and hence the EOMs need to be defined with respect to the asteroid rotating frame. Therefore, the state has to be defined by \mathbf{r}_A , \mathbf{v}_A and $\mathbf{q}_{B/A}$, $\omega_{B/A}^B$. The relative position can be given by:

$$\mathbf{r}^A = \mathbf{C}_{A/I} \mathbf{r}^I \quad (4.76)$$

where, $\mathbf{C}_{A/I}$ can be expressed using the quaternion $\mathbf{q}_{A/I}$ as

$$\mathbf{C}(\mathbf{q}, q_4) = (q_4^2 - \|\mathbf{q}_{1:3}\|^2) I_3 - 2q_4 [\mathbf{q}_{1:3} \times] + 2\mathbf{q}_{1:3} \mathbf{q}_{1:3}^T \quad (4.77)$$

$$= \begin{bmatrix} 1 - 2(q_2^2 + q_3^2) & 2(q_1 q_2 + q_3 q_4) & 2(q_1 q_3 - q_2 q_4) \\ 2(q_2 q_1 - q_3 q_4) & 1 - 2(q_1^2 + q_3^2) & 2(q_2 q_3 + q_1 q_4) \\ 2(q_3 q_1 + q_2 q_4) & 2(q_3 q_2 - q_1 q_4) & 1 - 2(q_1^2 + q_2^2) \end{bmatrix} \quad (4.78)$$

4.7.1. Translational Motion

The relative translational kinematic equation can be obtained by taking the derivative of the relative position vector, $\mathbf{r}^s ad A$,

$$\begin{aligned} \dot{\mathbf{r}}^A &= \mathbf{C}_{A/I} \dot{\mathbf{r}}^I - \omega_{A/I}^A \times \mathbf{C}_{A/I} \mathbf{r}^I \\ \mathbf{v}_{B/A}^A &= \mathbf{C}_{A/I} \dot{\mathbf{r}}^I - \omega_{A/I}^A \times \mathbf{r}^A \end{aligned} \quad (4.79)$$

The relative translational dynamic equation can be obtained by taking the derivative of the relative velocity vector, \mathbf{v}_A ,

$$\dot{\mathbf{v}}_{B/A}^A = \mathbf{C}_{A/I} \ddot{\mathbf{r}}^I - \omega_{A/I}^A \times \mathbf{C}_{A/I} \dot{\mathbf{r}}^I - \dot{\omega}_{A/I}^A \times \mathbf{C}_{A/I} \mathbf{r}^I + \omega_{A/I}^A \times \omega_{A/I}^A \times \mathbf{C}_{A/I} \mathbf{r}^I - \omega_{A/I}^A \times \mathbf{C}_{A/I} \dot{\mathbf{r}}^I \quad (4.80)$$

The term with $\dot{\omega}_{A/I}^A$ is omitted since the asteroid rotation rate is assumed to be constant causing the angular acceleration to be zero. Now replacing $\mathbf{C}_{A/I} \mathbf{r}_I$ and $\mathbf{C}_{A/I} \dot{\mathbf{r}}_I$ from Eqs. 5.76 and 5.79, we get

$$\mathbf{a}_{B/A}^A = \mathbf{C}_{A/I} \ddot{\mathbf{r}}^I - 2\omega_{A/I}^A \times (\mathbf{v}_{B/A}^A + \omega_{A/I}^A \times \mathbf{r}^A) + \omega_{A/I}^A \times \omega_{A/I}^A \times \mathbf{r}^A \quad (4.81)$$

The relative translational dynamic equation can therefore be given as,

$$\mathbf{a}_{B/A}^A = \mathbf{C}_{A/I} \ddot{\mathbf{r}}^I - 2\omega_{A/I}^A \times \mathbf{v}_{B/A}^A - \omega_{A/I}^A \times \omega_{A/I}^A \times \mathbf{r}^A \quad (4.82)$$

4.7.2. Rotational Motion

The relative attitude quaternion can be given as,

$$\mathbf{q}_{B/A} = \mathbf{q}_{B/I} \otimes \mathbf{q}_{A/I}^* \quad (4.83)$$

and the relative angular rate,

$$\omega_{B/A}^B = \omega_{B/I}^B - \mathbf{C}_{B/A} \omega_{A/I}^A \quad (4.84)$$

where, $\mathbf{C}_{B/A}$ can be obtained from $\mathbf{q}_{B/A}$. For the attitude kinematics, the derivative of the relative quaternion, $\dot{\mathbf{q}}_{B/A}$ is taken with the help of quaternion derivative properties **quat paper**

$$\begin{aligned} \dot{\mathbf{q}}_{B/A} &= \dot{\mathbf{q}}_{B/I} \otimes \mathbf{q}_{A/I}^* + \mathbf{q}_{B/I} \otimes \dot{\mathbf{q}}_{A/I}^* \\ \dot{\mathbf{q}}_{B/A} &= \frac{1}{2} \omega_{B/I}^B \otimes \mathbf{q}_{B/I} \otimes \mathbf{q}_{A/I}^* + \mathbf{q}_{B/I} \otimes \frac{1}{2} \omega_{I/A}^I \otimes \mathbf{q}_{I/A} \end{aligned} \quad (4.85)$$

From properties of angular velocities we know that,

$$\omega_{I/A}^I = -\omega_{A/I}^I = -\mathbf{q}_{I/A} \otimes \omega_{A/I}^A \otimes \mathbf{q}_{I/A}^* \quad (4.86)$$

Substituting this new representation in Eq. 5.85

$$\begin{aligned} \dot{\mathbf{q}}_{B/A} &= \frac{1}{2} \omega_{B/I}^B \otimes \mathbf{q}_{B/A} - \frac{1}{2} \mathbf{q}_{B/I} \otimes \mathbf{q}_{I/A} \otimes \omega_{A/I}^A \otimes \mathbf{q}_{I/A}^* \otimes \mathbf{q}_{I/A} \\ \dot{\mathbf{q}}_{B/A} &= \frac{1}{2} \omega_{B/I}^B \otimes \mathbf{q}_{B/A} - \frac{1}{2} \mathbf{q}_{B/A} \otimes \omega_{A/I}^A \end{aligned} \quad (4.87)$$

From Eq.5.84 we get,

$$\omega_{A/I}^A = \mathbf{q}_{B/A}^* \otimes (\omega_{B/I}^B - \omega_{B/A}^B) \otimes \mathbf{q}_{B/A} \quad (4.88)$$

Using the above equation in Eq. 5.87

$$\dot{\mathbf{q}}_{B/A} = \frac{1}{2} \omega_{B/I}^B \otimes \mathbf{q}_{B/A} - \frac{1}{2} \mathbf{q}_{B/A} \otimes \mathbf{q}_{B/A}^* \otimes (\omega_{B/I}^B - \omega_{B/A}^B) \otimes \mathbf{q}_{B/A} \quad (4.89)$$

Therefore the relative attitude kinematics equation becomes,

$$\dot{\mathbf{q}}_{B/A} = \frac{1}{2} \omega_{B/A}^B \otimes \mathbf{q}_{B/A} \quad (4.90)$$

For relative attitude dynamics we need to differentiate the Eq. 5.84

$$\dot{\omega}_{B/A}^B = \dot{\omega}_{B/I}^B - C_{B/A} \dot{\omega}_{A/I}^A + \omega_{B/A}^B \times C_{B/A} \omega_{A/I}^A \quad (4.91)$$

Substituting for $\dot{\omega}_{B/I}^B$ from the attitude dynamics given in Eq. 5.73

$$\begin{aligned} \dot{\omega}_{B/A}^B &= J^{-1}(\mathbf{T}^B - \omega_{B/I}^B \times J\omega_{B/I}^B) - C_{B/A} \dot{\omega}_{A/I}^A + \omega_{B/A}^B \times C_{B/A} \omega_{A/I}^A \\ &= J^{-1}(\mathbf{T}^B - (\omega_{B/A}^B + C_{B/A} \omega_{A/I}^A) \times J(\omega_{B/A}^B + C_{B/A} \omega_{A/I}^A)) - C_{B/A} \dot{\omega}_{A/I}^A + \omega_{B/A}^B \times C_{B/A} \omega_{A/I}^A \\ &= J^{-1}(\mathbf{T}^B - \omega_{B/A}^B \times J\omega_{B/A}^B - C_{B/A} \omega_{A/I}^A \times JC_{B/A} \omega_{A/I}^A) + \omega_{B/A}^B \times C_{B/A} \omega_{A/I}^A \end{aligned} \quad (4.92)$$

The relative attitude dynamic equation is therefore given as below.

$$\dot{\omega}_{B/A}^B = J^{-1}(\mathbf{T}^B - \omega_{B/A}^B \times J\omega_{B/A}^B - \omega_{A/I}^A \times J\omega_{A/I}^A) - \omega_{A/I}^A \times \omega_{B/A}^B \quad (4.93)$$

4.8. Dual Quaternion Dynamics and Kinematics

To implement the inertial and relative kinematics and dynamics in the guidance algorithms, we need to convert the EOMs to the form of dual quaternions. In this section we derive the complete inertial and relative EOMS using DQs.

4.8.1. DQ Inertial EOMS

The derivations of the kinematic and dynamic equations of the SC in dual quaternion form can be found in Lee and Mesbahi 2015 and Filipe and Tsiotras 2013. They kinematic equation can be given as:

$$\dot{\check{\mathbf{q}}}_{B/I} = \frac{1}{2} \check{\mathbf{q}}_{B/I} \check{\otimes} \check{\omega}_{B/I}^B \quad (4.94)$$

where the dual quaternion and dual velocity are as below,

$$\check{\mathbf{q}}_{B/I} = \mathbf{q}_{B/I} + \frac{1}{2} \mathbf{r}^I \odot \mathbf{q}_{B/I} \epsilon, \quad \check{\omega}_{B/I}^B = (\omega_{B/I}^B \mathbf{v}_{B/I}^B)$$

The dynamic equation is as follows:

$$\check{\mathbf{J}} \check{\dot{\omega}}_{B/I}^B + \check{\omega}_{B/I}^B \check{\times} \check{\mathbf{J}} \check{\omega}_{B/I}^B = \check{\mathbf{F}}^B \quad (4.95)$$

where the matrix for inertia, J and mass, m combined and that for force, F and torque, T combined are,

$$\check{\mathbf{J}} = \left[\begin{array}{cc|cc} 0_{3 \times 3} & 0 & mI_3 & 0 \\ 0 & 0 & 0 & 1 \\ \hline J & 0 & 0_{3 \times 3} & 0 \\ 0 & 1 & 0 & 0 \end{array} \right], \quad \check{\mathbf{F}}^B = \begin{pmatrix} \mathbf{F}^B \\ 0 \\ \mathbf{T}^B \\ 0 \end{pmatrix}$$

with the translational and rotational dynamic EOMs as follows,

$$\begin{aligned} \mathbf{F}^B &= m\dot{\mathbf{v}}_{B/I}^B + \omega_{B/I}^B \times m\mathbf{v}_{B/I}^B \\ \mathbf{T}^B &= \mathbf{J}\dot{\omega}_{B/I}^B + \omega_{B/I}^B \times \mathbf{J}\omega_{B/I}^B \end{aligned}$$

These equations will be used to represent the SC orbital and attitude dynamics in the inertial frame fixed to the asteroid centre while developing the G&C algorithms using dual quaternions. These equations can be converted to obtain the relative state of the SC with respect to the rotating centre fixed frame at the target body.

4.8.2. DQ Relative Kinematics

The DQ representation of the body frame, B with respect to the asteroid rotating frame, A is $\dot{\mathbf{q}}_{B/A} = \mathbf{q}_{B/A} + \frac{\epsilon}{2} \mathbf{q}_{B/A} \otimes \mathbf{r}^A$ with reference to discussions in Chapter 4. Differentiating this with respect of time we get,

$$\begin{aligned}\dot{\mathbf{q}}_{B/A} &= \dot{\mathbf{q}}_{B/A} + \frac{\epsilon}{2} \left(\dot{\mathbf{q}}_{B/A} \otimes \mathbf{r}^A + \mathbf{q}_{B/A} \otimes \dot{\mathbf{r}}_{B/A}^A \right) \\ &= \frac{1}{2} \boldsymbol{\omega}_{B/A}^B \otimes \mathbf{q}_{B/A} + \frac{\epsilon}{2} \left(\frac{1}{2} \boldsymbol{\omega}_{B/A}^B \otimes \mathbf{q}_{B/A} \otimes \mathbf{r}^A + \mathbf{q}_{B/A} \otimes \mathbf{v}_{B/A}^A \right)\end{aligned}\quad (4.96)$$

Rearranging Eq. 8.43 in the matrix form we get,

$$\dot{\mathbf{q}}_{B/A} = \frac{1}{2} \begin{bmatrix} [\boldsymbol{\omega}_{B/A}^B \otimes] & 0_{4 \times 4} \\ [\mathbf{v}_{B/A}^A \otimes] & [\boldsymbol{\omega}_{B/A}^B \otimes] \end{bmatrix} \left(\frac{1}{2} \mathbf{q}_{B/A} \otimes \mathbf{r}^A \right) \quad (4.97)$$

For convenience, representing the velocity in the B frame we get

$$\mathbf{q}_{B/A} \otimes \mathbf{v}_{B/A}^A = \mathbf{q}_{B/A} \otimes \mathbf{v}_{B/A}^A \otimes \mathbf{q}_{B/A}^* \otimes \mathbf{q}_{B/A} = \mathbf{v}_{B/A}^B \otimes \mathbf{q}_{B/A} \quad (4.98)$$

Therefore Eq. 8.44 can be rewritten as,

$$\dot{\mathbf{q}}_{B/A} = \frac{1}{2} \begin{bmatrix} [\boldsymbol{\omega}_{B/A}^B \otimes] & 0_{4 \times 4} \\ [\mathbf{v}_{B/A}^B \otimes] & [\boldsymbol{\omega}_{B/A}^B \otimes] \end{bmatrix} \left(\frac{1}{2} \mathbf{q}_{B/A} \otimes \mathbf{r}^A \right) \quad (4.99)$$

Introducing a new variable as dual velocity,

$$\check{\boldsymbol{\omega}}_{B/A}^B = \boldsymbol{\omega}_{B/A}^B + \epsilon \mathbf{v}_{B/A}^B \quad (4.100)$$

Therefore the combined translational and rotational kinematics can be represented in the DQ form as follows,

$$\dot{\mathbf{q}}_{B/A} = \frac{1}{2} \check{\boldsymbol{\omega}}_{B/A}^B \check{\otimes} \check{\mathbf{q}}_{B/A} \quad (4.101)$$

where, $\check{\otimes}$ represents the DQ product and can be written in the form,

$$[\check{\boldsymbol{\omega}}_{B/A}^B \check{\otimes}] = \begin{bmatrix} [\boldsymbol{\omega}_{B/A}^B \otimes] & 0_{4 \times 4} \\ [\mathbf{v}_{B/A}^B \otimes] & [\boldsymbol{\omega}_{B/A}^B \otimes] \end{bmatrix} \quad (4.102)$$

4.8.3. DQ Relative Dynamics

Eqs. 5.82 and 5.93, give the formulation for relative translational and rotational dynamics. Reiterating them here,

$$\begin{aligned}\mathbf{a}_{B/A}^A &= \mathbf{C}_{A/I} \ddot{\mathbf{r}}^I - 2\boldsymbol{\omega}_{A/I}^A \times \mathbf{v}_{B/A}^A - \boldsymbol{\omega}_{A/I}^A \times \boldsymbol{\omega}_{A/I}^A \times \mathbf{r}^A \\ \dot{\boldsymbol{\omega}}_{B/A}^B &= \mathbf{J}^{-1} (\mathbf{T}^B - \boldsymbol{\omega}_{B/A}^B \times \mathbf{J} \boldsymbol{\omega}_{B/A}^B - \boldsymbol{\omega}_{A/I}^B \times \mathbf{J} \boldsymbol{\omega}_{A/I}^B) + \boldsymbol{\omega}_{B/A}^B \times \boldsymbol{\omega}_{A/I}^B\end{aligned}\quad (4.103)$$

where the translational dynamics can be rewritten as,

$$\mathbf{a}_{B/A}^A = \left(\frac{\mathbf{F}^A}{m} + \mathbf{g}^A \right) - 2\boldsymbol{\omega}_{A/I}^A \times \mathbf{v}_{B/A}^A - \boldsymbol{\omega}_{A/I}^A \times \boldsymbol{\omega}_{A/I}^A \times \mathbf{r}^A \quad (4.104)$$

Now since the dual velocity is in the B frame, we need to convert the translational dynamics to B frame

$$\mathbf{v}_{B/A}^B = \mathbf{C}_{B/A} \mathbf{v}_{B/A}^A \quad (4.105)$$

Differentiating Eq. 5.105, the translational dynamics in the B frame can therefore be given as,

$$\begin{aligned}\mathbf{a}_{B/A}^B &= \mathbf{C}_{B/A} \dot{\mathbf{v}}_{B/A}^A - \boldsymbol{\omega}_{B/A}^B \times \mathbf{C}_{B/A} \mathbf{v}_{B/A}^A \\ \mathbf{a}_{B/A}^B &= \mathbf{C}_{B/A} \left(\frac{\mathbf{F}^A}{m} + \mathbf{g}^A + \mathbf{a}_D^A - 2\boldsymbol{\omega}_{A/I}^A \times \mathbf{v}_{B/A}^A - \boldsymbol{\omega}_{A/I}^A \times \boldsymbol{\omega}_{A/I}^A \times \mathbf{r}^A \right) - \boldsymbol{\omega}_{B/A}^B \times \mathbf{C}_{B/A} \mathbf{v}_{B/A}^A\end{aligned}\quad (4.106)$$

Rearranging Eqs. 5.103 and 5.106 we get,

$$\mathbf{F}^B + m\mathbf{g}^B + m\mathbf{a}_D^B = m\dot{\mathbf{v}}_{B/A}^B + \boldsymbol{\omega}_{B/A}^B \times m\mathbf{v}_{B/A}^B + \boldsymbol{\omega}_{A/I}^B \times \boldsymbol{\omega}_{A/I}^B \times m\mathbf{r}^B + 2m\boldsymbol{\omega}_{A/I}^B \times \mathbf{v}_{B/A}^B \quad (4.107)$$

$$\mathbf{r}_{ex} \times \mathbf{F}^B + \mathbf{T}_D^B = \mathbf{J}\dot{\omega}_{B/A}^B + (\omega_{B/A}^B + \omega_{A/I}^B) \times \mathbf{J}(\omega_{B/A}^B + \omega_{A/I}^B) + \mathbf{J}\omega_{A/I}^B \times \omega_{B/A}^B \quad (4.108)$$

For DQ dynamics, we need to combine Eqs. 5.107 and 5.108 such that it incorporates the dual velocity defined in the earlier subsection of DQ relative kinematics. using the following matrix representations.

$$\check{\mathbf{F}}^B = \begin{pmatrix} \mathbf{F}^B + mg^B + ma_D^B \\ 0 \\ \mathbf{r}_{ex} \times \mathbf{F}^B + \mathbf{T}_D^B \\ 0 \end{pmatrix}, \check{\mathbf{J}} = \left[\begin{array}{ccc|c} 0_{3 \times 3} & 0 & mI_3 & 0 \\ 0 & 0 & 0 & 1 \\ \hline \mathbf{J} & 0 & 0_{3 \times 3} & 0 \\ 0 & 1 & 0 & 0 \end{array} \right] \quad (4.109)$$

After some rearranging, we can have the dynamics in the form,

$$\check{\mathbf{F}}^B = \check{\mathbf{J}}\dot{\omega}_{B/A}^B + (\check{\omega}_{B/A}^B + \check{\omega}_{A/I}^B) \check{\times} \check{\mathbf{J}}(\check{\omega}_{B/A}^B + \check{\omega}_{A/I}^B) + \check{\mathbf{J}}\check{\omega}_{A/I}^B \check{\times} \check{\omega}_{B/A}^B + \check{\omega}_{A/I}^B \check{\times} \check{\omega}_{A/I}^B \check{\times} \mathbf{A} \quad (4.110)$$

where,

$$\check{\omega}_{A/I}^B = \begin{pmatrix} \omega_{A/I}^B \\ \mathbf{v}_{A/I}^B \end{pmatrix}, \quad [\check{\omega}_{A/I}^B \check{\times}] = \begin{bmatrix} [\omega_{A/I}^B \times] & 0_{4 \times 4} \\ [\mathbf{v}_{A/I}^B \times] & [\omega_{A/I}^B \times] \end{bmatrix} \quad (4.111)$$

$\mathbf{v}_{A/I}^B$ is zero since the origins of the frames A and I are the centre of the asteroid. The matrix \mathbf{A} is given by the quaternion product given in Eq. ,

$$\mathbf{A} = \begin{pmatrix} 0_{3 \times 1} \\ 0 \\ 2\mathbf{q}_d \mathbf{q}_{B/A}^* \\ 0 \end{pmatrix} \quad (4.112)$$

4.9. State Vectors

In the thesis we work with three state vectors: one that is represented with respect to the asteroid centered inertial frame (I), the second and third with respect to the asteroid centered rotating frame (A). They can be given as follows:

$$\mathbf{X}_I = \begin{pmatrix} m \\ \mathbf{r}^I \\ \mathbf{v}^I \\ \omega_{B/I}^B \\ \mathbf{q}_{B/I} \\ \mathbf{q}_{A/I} \end{pmatrix}, \quad \mathbf{X}_A = \begin{pmatrix} m \\ \mathbf{r}^A \\ \mathbf{v}_{B/A}^B \\ \omega_{B/A}^B \\ \mathbf{q}_{B/A} \end{pmatrix}, \quad \check{\mathbf{X}}_A = \begin{pmatrix} m \\ \check{\mathbf{q}}_{B/A} \\ \check{\omega}_{B/A}^B \end{pmatrix} \quad (4.113)$$

where, m is the total mass of the SC at any instant of time.

The dynamics use the inertial state vector to avoid additional accelerations due to the non inertial asteroid rotating frame. The inertial state vector from the dynamics will be converted to the relative state using DCM or quaternion transformation.

4.10. External Disturbances

In this section, we enlist all the possible disturbances to the SC when it is performing its mission objectives. Of these disturbing forces, we will exclude thermal recoil forces since modelling them requires the knowledge specific SC structural and material design and also its magnitude is very less as compared to the other perturbances. We will also exclude mass expulsion disturbances since the sources can be identified by experimentation during verification and validation testing of the systems onboard the SC before the mission and can be accounted for in the SC model. The flexibility of the SC can be modelled by a simple mass-spring system and also the slosh dynamics and these will be added in the recommendations from this thesis since the main objectives of the thesis can be satisfied without the inclusion of these. The main focus in this thesis is given to the gravity gradient, solar radiation pressure and third body gravitational perturbation.

The SC orbit environment has to be characterized accurately since it is one of the crucial requirements for its GNC. The environment around and about the asteroids lead to a number of external torques that need to be modelled for accurate measurements and observations. In the following subsections we will discuss the mathematical models for the polyhedron gravity field of the asteroid, the gravity gradient torque, the solar radiation pressure, the third body perturbation due to the sun and the torques caused by them. These need to be accounted for while developing the GNC system of the SC for a mission to an asteroid and we include them in our guidance algorithms to be developed in later chapters.

4.10.1. Small Body Gravity Field

Modelling the gravitational field of an irregular shaped small body is an extremely challenging astrodynamics problem. There are three fundamentally different ways of approaching this problem. The first approach involves using a series expansion to approximate the gravitational potential for example using external spherical harmonics (Takahashi and Scheeres 2014). In this approach, series coefficients are evaluated as integrals over the volume of the body and in case of a constant density body, it is reduced to integrals over just the surface of the body. This approach has more disadvantages due to higher truncation error when the gravity field is evaluated close to the model's radius of convergence, inside the Brillouin sphere¹ the harmonic expansion fails to converge and it cannot say whether the field point is inside or outside the body and a separate algorithm is required to detect this crucial geometric information.

The second approach is mass concentration where the target body is filled with point masses on an evenly spaced grid till the total mass of the body is realised (Geissler et al. 1996). This method proves to be less accurate than the harmonic approach even though it does not diverge and will converge to the true gravity field. It is limited by the number of point masses since its computationally difficult and still has significant errors with large numbers of mascons. Also, it does not provide whether the field is inside or outside the body same as the harmonic approach.

The third approach is the constant density polyhedron, where direct computation of the gravitational potential is done using a finite number of polyhedral definitions (Werner and Scheeres 1997). For the given shape and density this gravity field is exact and the errors can be reduced to the shape determination and level of chosen discretization. This model is valid up to the surface of the body and has no region of divergence. It, therefore, helps in studying dynamics of particles launched from the surface. A polyhedron algorithm can detect whether the field point is inside or outside the polyhedron by evaluating the Laplacian of the gravitational potential. Razgus 2017 uses this model in his work to describe the gravitational fields of Itokawa. The gravitational potential of a constant density polyhedron at a field point \mathbf{r} is given as follows:

$$U_p(\mathbf{r}) = \frac{1}{2} G \rho \sum_{e \in \text{edges}} \mathbf{r}_e^T \mathbf{E}_e \mathbf{r}_e \cdot L_e - \frac{1}{2} G \rho \sum_{f \in \text{faces}} \mathbf{r}_f^T \mathbf{F}_f \mathbf{r}_f \cdot \omega_f \quad (4.114)$$

where, G is the gravitational constant, ρ is the mean asteroid density (assumed to be constant), r_e and r_f are distances from a field point to an edge and a face respectively, E_e is a dyadic matrix of an edge and F_f is an outer product of a face normal. They can be calculated as follows:

$$\mathbf{E}_e = \mathbf{n}_A (\mathbf{n}_{12}^A)^T + \mathbf{n}_B (\mathbf{n}_{21}^B)^T \quad (4.115)$$

$$\mathbf{F}_f = \mathbf{n}_f (\mathbf{n}_f)^T \quad (4.116)$$

where, \mathbf{n}_A , \mathbf{n}_B and \mathbf{n}_f are unit vectors normal to the faces A, B and a general face respectively. The unit vectors \mathbf{n}_{12}^A and \mathbf{n}_{21}^B are normal to the edge. They are associated with the face normal. These vectors are represented in the Figure 4.7a. Using the position vectors from the asteroid frame to the face's vertices as shown in Figure 4.7b, these normals can be calculated as follows:

$$\mathbf{n}_f = \frac{(\mathbf{r}_2 - \mathbf{r}_1) \times (\mathbf{r}_3 - \mathbf{r}_2)}{\|(\mathbf{r}_2 - \mathbf{r}_1) \times (\mathbf{r}_3 - \mathbf{r}_2)\|} \quad (4.117)$$

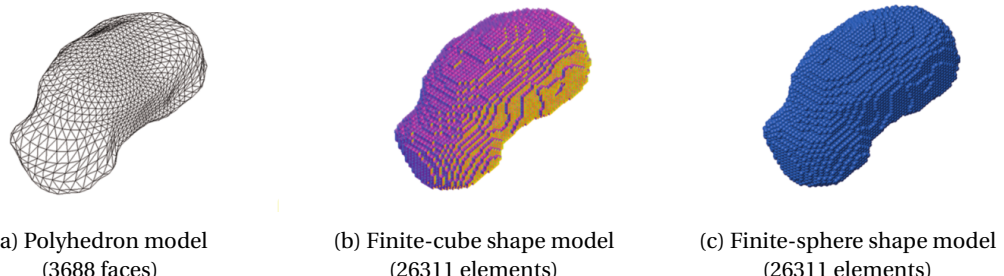


Figure 4.6: Different types of shape models for Itokawa (Park, Werner, and Bhaskaran 2010)

¹A Brillouin sphere is a minimum sphere that circumscribes the body

$$\hat{\mathbf{n}}_{12}^A = \frac{(\mathbf{r}_1 - \mathbf{r}_2) \times \mathbf{n}_A}{\|(\mathbf{r}_1 - \mathbf{r}_2) \times \mathbf{n}_A\|} \quad (4.118)$$

$$\hat{\mathbf{n}}_{21}^B = \frac{(\mathbf{r}_2 - \mathbf{r}_1) \times \mathbf{n}_B}{\|(\mathbf{r}_2 - \mathbf{r}_1) \times \mathbf{n}_B\|} \quad (4.119)$$

The vectors from the SC/field point to the vertices of the face (\mathbf{r}_i , \mathbf{r}_j , \mathbf{r}_k) can be defined as follows:

$$\mathbf{r}_i = \mathbf{r}_1 - \mathbf{r}_A \quad (4.120)$$

$$\mathbf{r}_j = \mathbf{r}_2 - \mathbf{r}_A \quad (4.121)$$

$$\mathbf{r}_k = \mathbf{r}_3 - \mathbf{r}_A \quad (4.122)$$

where, \mathbf{r}_A is the position vector of the SC/field point in the asteroid frame. The vectors have magnitudes r_i , r_j , r_k respectively. Using these definitions the dimensionless factors L_e and ω_f , which are the potential of a wire and the pre-face factor respectively are given as below:

$$L_e = \ln \frac{r_i + r_j + e_{ij}}{r_i + r_j - e_{ij}} \quad (4.123)$$

$$\omega_f = 2 \arctan \frac{\mathbf{r}_i \cdot \mathbf{r}_j \times \mathbf{r}_k}{r_i r_j r_k + r_i (\mathbf{r}_j \cdot \mathbf{r}_k) + r_j (\mathbf{r}_k \cdot \mathbf{r}_i) + r_k (\mathbf{r}_i \cdot \mathbf{r}_j)} \quad (4.124)$$

The vectors \mathbf{r}_e and \mathbf{r}_f from Eq.4.1 are arbitrary vectors from the SC to an edge and a face respectively. They are defined as follows,

$$\mathbf{r}_e = \frac{\mathbf{r}_i + \mathbf{r}_j}{2} \quad (4.125)$$

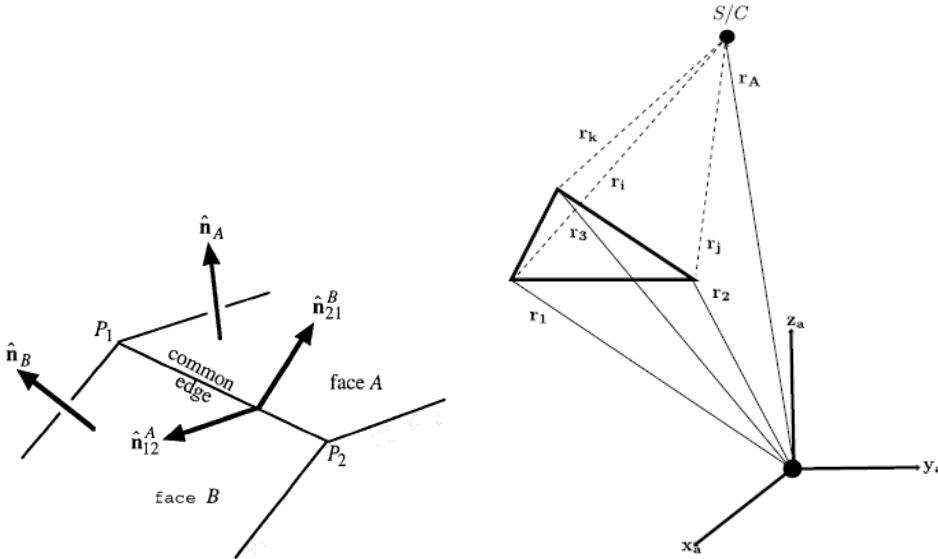
$$\mathbf{r}_f = \frac{\mathbf{r}_i + \mathbf{r}_j + \mathbf{r}_k}{3} \quad (4.126)$$

such that they lie in the middle of an edge and a triangular face.

The potential gradient or the acceleration due to gravity (\mathbf{g}_A) and the Laplacian of the potential which can be used in the know whether the asteroid would crash into the asteroid are then given as follows:

$$\mathbf{g}_A = \nabla U = -G \rho \sum_{e \in \text{edges}} \mathbf{E}_e \mathbf{r}_e L_e + G \rho \sum_{f \in \text{faces}} \mathbf{F}_f \mathbf{r}_f \omega_f \quad (4.127)$$

$$\nabla^2 U = -G \rho \sum_{f \in \text{faces}} \omega_f \quad (4.128)$$



(a) Two face normal and edge normal vectors.
(Werner and Scheeres 1997)

(b) Position vectors to the vertices of a face.
(Razgus 2017)

Figure 4.7: An edge at two faces.

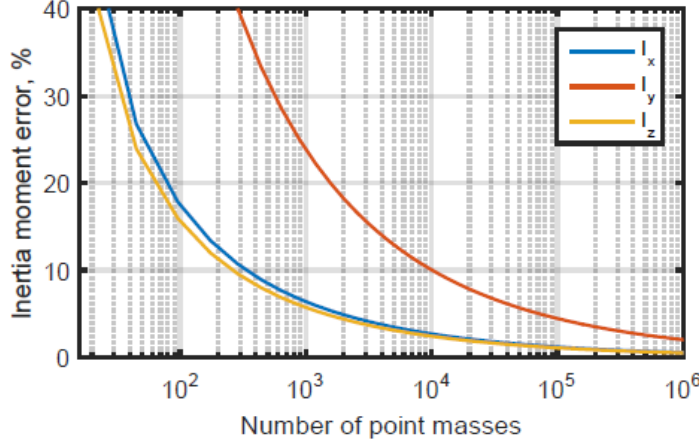


Figure 4.8: Numerical solution for moments of inertia in central gravity model against number of point masses. (Razgus 2017)

Computing the Laplacian provides information on whether the field point is inside, outside, on a face, on a vertex or on an edge (Park, Werner, and Bhaskaran 2010).

$$-\frac{\nabla^2 U(\mathbf{r}_i)}{G \rho} = \begin{cases} 4\pi, & \text{if inside} \\ 0, & \text{if outside} \\ 2\pi, & \text{if on a face} \\ \text{solid angle}, & \text{if on a vertex or on an edge} \end{cases} \quad (4.129)$$

The disadvantage of this method is that it assumes a constant density of the asteroid for the computation and therefore for an object with significant density variation this is not a good model. A finite element approach has been developed to overcome this disadvantage. Optical survey of the asteroid provides a high precision polyhedral shape which is then filled with finite elements like cubes or spheres with distinct density values (Park, Werner, and Bhaskaran 2010). Figs. 4.6a, 4.6b and 4.6b provide the predicted shape model of Itokawa from radar survey and constructed shape models filled with finite elements like cubes and spheres respectively. Once the constructed models are available, the attraction saying whether the SC is inside the Brillouin sphere or the body has a significant density variation can be computed. The true attraction from the polyhedron model is then compared with that based on the finite element model and it is found that the later provides a very good approximation of the polyhedral shape model. But these models increase the computations costs tremendously and can become an ill-conditioned problem based on the finite element size. Hence we will stick with the constant density polyhedron model since it serves the purpose of this assignment with the required level of accuracy.

Gravity Gradient Torque

Due to the irregular shape, non-spherical mass distribution and rotational state of a small body, it does not have a uniform gravity field as we discussed in the previous section. Due to this non-uniform gravity field as well as the orientation of the SC with respect to the small body, different parts of the SC structure will be subjected to different gravitational attractive forces. The SC is therefore subjected to gravity gradient torque which could destabilize it, if unaccounted for. Gravity gradient torques can be utilised to passively stabilize the SC.

The gravity gradient torque can be found by summing the contributions of the gravitational field on various point masses of the SC. For a central gravitational field that is spherically symmetric and the SC as a rigid body, the force on any i^{th} point mass of the SC having n number of point masses, can be given by (Wie 2001):

$$\mathbf{F}_{GG}^i = m_i \mathbf{g}_C^i = -\frac{\mu \mathbf{r}_i m_i}{|\mathbf{r}_i|^3} \quad (4.130)$$

where, \mathbf{g}_C^i is the gravitational acceleration at i^{th} point due to the central gravity field, \mathbf{r}_i is the position vector of the i^{th} point mass with respect to the asteroid reference frame and m_i is the mass of the i^{th} point mass.

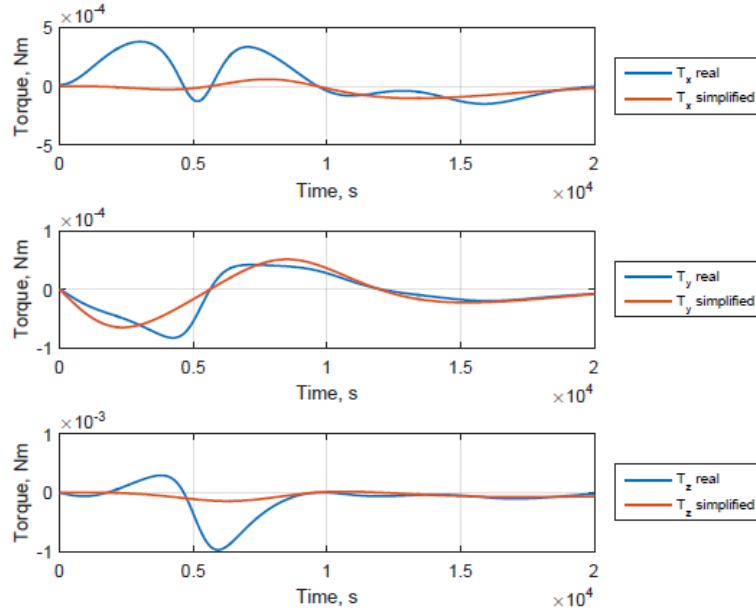


Figure 4.9: Gravity gradient torques from central gravity and polyhedron models compared in Kleopatra's gravity field. (Razgus 2017)

The gravity gradient torque can therefore be given as:

$$\mathbf{T}_{GG} = \sum_{i=1}^n \boldsymbol{\rho}_i \times \mathbf{F}_{GG}^i = -\mu \sum_{i=1}^n \frac{\boldsymbol{\rho}_i \times (\mathbf{r}_c + \boldsymbol{\rho}_i)}{|\mathbf{r}_c + \boldsymbol{\rho}_i|^3} m_i = -\mu \sum_{i=1}^n \frac{\boldsymbol{\rho}_i \times \mathbf{r}_c}{|\mathbf{r}_c + \boldsymbol{\rho}_i|^3} m_i \quad (4.131)$$

where, $\boldsymbol{\rho}_i$ is the position vector of the i^{th} mass point with respect to the SC's COM and \mathbf{r}_c is the vector between the COM of the asteroid and the SC. Using the expansion of $(|\mathbf{r}_c + \boldsymbol{\rho}_i|)^{-3}$ series and approximating it to the first and second order terms we get:

$$\begin{aligned} |\mathbf{r}_c + \boldsymbol{\rho}_i|^{-3} &= r_c^{-3} \left\{ 1 + \frac{2(\mathbf{r}_c \cdot \boldsymbol{\rho}_i)}{r_c^2} + \frac{\boldsymbol{\rho}_i^2}{r_c^2} \right\}^{-\frac{3}{2}} \\ &= r_c^{-3} \left\{ 1 - \frac{3(\mathbf{r}_c \cdot \boldsymbol{\rho}_i)}{r_c^2} \right\} \end{aligned} \quad (4.132)$$

Resubstituting in Eq. 4.10, we get:

$$\mathbf{T}_{GG} = -\frac{3\mu}{r_c^5} \sum_{i=1}^n (\mathbf{r}_c \cdot \boldsymbol{\rho}_i) (\boldsymbol{\rho}_i \times \mathbf{r}_c) m_i \quad (4.133)$$

Further manipulation and simplification of the equation gets us to the result:

$$\mathbf{T}_{GG} = -\frac{3\mu}{r_c^5} \mathbf{r}_c \times \mathbf{J} \cdot \mathbf{r}_c \quad (4.134)$$

where, \mathbf{J} is the inertia moment tensor of the SC. This equation has some simplifications and assumptions that make it unsuitable to be used for asteroids. It assumes a central gravity field with spherical symmetry and also neglects the higher order terms of the gravity field. It can be seen that the components of the acceleration along the axes of the reference frame are not symmetrical or constant. The gradient torque model using the central gravity field can be made more accurate by increasing the number of point masses. But it requires more than ten thousand point masses to get an accuracy close to 10% (Razgus 2017). As seen from Figure 4.8 the moments of inertia calculated for increasing number of point masses shows a decrease in the % error but at the cost of a huge number of computations.

The polyhedron model presented in the previous section provides a better model for the gravity gradient torque for asteroids. Using the result from the polyhedron model for the acceleration due to gravity (Eq. 4.14)

we can rewrite the torque Eq. 4.18 as:

$$\mathbf{T}_{GG} = \sum_{i=1}^n \boldsymbol{\rho}_i \times \mathbf{F}_{GG}^i = \sum_{i=1}^n \boldsymbol{\rho}_i \times m_i \mathbf{g}_A^i \quad (4.135)$$

where \mathbf{g}_A^i represents the gravitational acceleration at the i^{th} point mass from the polyhedron model. In the report by Razgus 2017, the gravity gradient torque achieved from the central gravity field and polyhedron field have been compared and plotted for Kleopatra as can be seen in Figure 4.9. It can be seen from the figure that the central gravity field fails to incorporate higher order couplings and/or non central gravity field terms. Even though a similar trend is observed the magnitudes are way off.

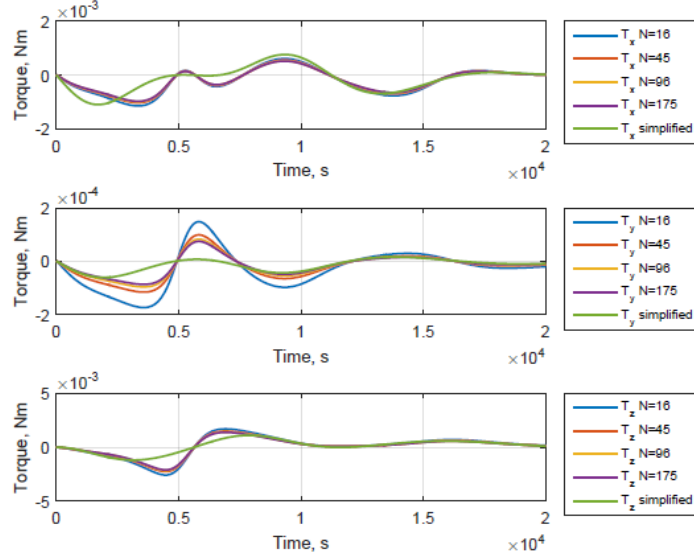


Figure 4.10: Gravity gradient torques from increasing point masses polyhedron model (Razgus 2017)

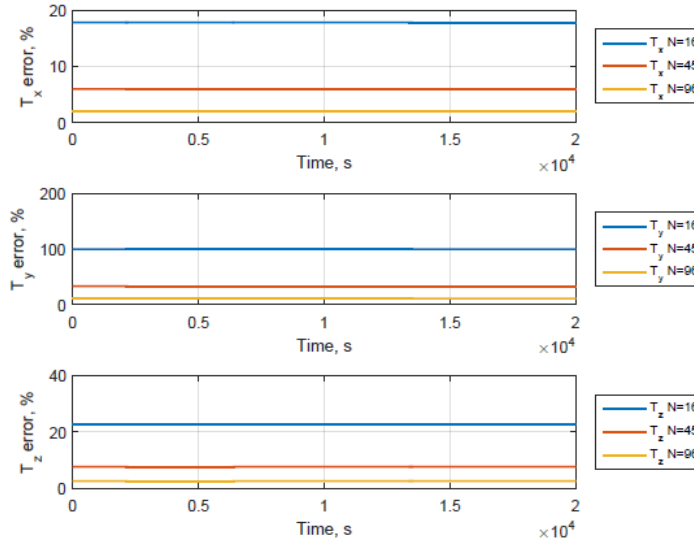


Figure 4.11: Percentage errors in gravity gradient torques from a various number of point mass polyhedron models compared with the $n=175$ model. (Razgus 2017)

Razgus 2017 has also presented the comparison between GG torques using the polyhedron acceleration due to gravity for increasing number of point masses and the results are plotted in Figure 4.10. Relative errors

between the models are compared using the formula:

$$T = \frac{T_{real} - T_N}{T_{real}} \times 100\% \quad (4.136)$$

where, T_{real} represents the most accurate representation of the GG torques and T_N represents the GG torques from the lower value of point masses model of the SC. Another observation made from these empirical calculations as seen in Figure 4.11 is that the error between the real torque model and another lower-numbered point mass model remains constant throughout. Although it seems intuitive it lacks background theory as to why it should remain constant. But this proves useful since once the comparison has been made, computations can be reduced to the lower point masses model and it can be simply corrected for the constant error.

4.10.2. Third Body Gravitational Perturbation

A celestial body or object is under the influence of gravitational attraction of other celestial bodies. The gravitational forces of bodies besides the central body leads to perturbation in the motion of the body under their influence. In case of an SC revolving about an asteroid, this could cause a significant disturbance due to the SC's low mass as well as the weak and irregular gravity field of the asteroid. The magnitude of this force varies depending on the distance of the perturbing celestial body as well as its mass, as is known from the Newtonian gravitational attraction. In the solar system, the sun proves as the biggest source of perturbing accelerations. Since we are considering NEAs and asteroids in the MAB, the gravitational forces of Earth, Mars or Jupiter could also prove to be significant perturbing forces. In Figure 4.12 the relative positions of the asteroid as the central body, the SC and the perturbing body with respect to the asteroid reference frame have been represented.

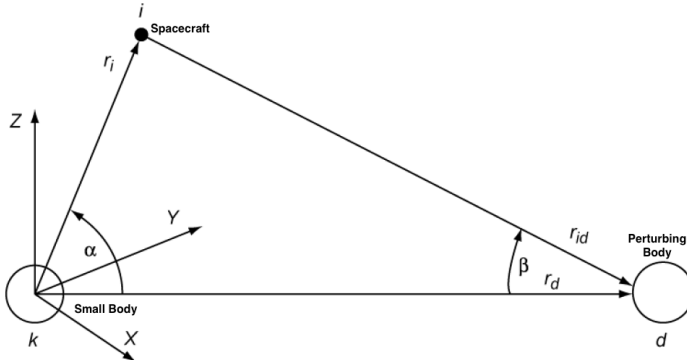


Figure 4.12: Relative positions of the SC, small body and the perturbing body. (Wakker 2015)

For a single perturbing body, we can treat the system as a three body problem to find the relative acceleration of the SC with respect to the asteroid due to the perturbing force. The total acceleration of the SC can be given as (Wakker 2015):

$$\mathbf{a}_T = \frac{d^2 \mathbf{r}_i}{dt^2} = -G \frac{m_i + m_k}{r_i^3} \mathbf{r}_i + G \sum_{d \neq i, k} m_d \left(\frac{\mathbf{r}_d - \mathbf{r}_i}{r_{id}^3} - \frac{\mathbf{r}_d}{r_d^3} \right) \quad (4.137)$$

where, m_i , m_d , m_k are the masses of the SC, perturbing body and asteroid respectively and r_i , r_d are the position vectors of the SC and the perturbing body with respect to the asteroid reference frame respectively. The first term on the right hand side of the Eq. 4.24 represents the acceleration due to a central gravity field of the asteroid and the second term represents the acceleration due to the perturbing body. The perturbing

acceleration due to a single body is therefore:

$$\begin{aligned}\mathbf{a}_P &= -G m_d \left(\frac{\mathbf{r}_d - \mathbf{r}_i}{r_{id}^3} - \frac{\mathbf{r}_d}{r_d^3} \right) \\ &= -G m_d \sqrt{\left(\frac{\mathbf{r}_{id}}{r_{id}^3} - \frac{\mathbf{r}_d}{r_d^3} \right) \cdot \left(\frac{\mathbf{r}_{id}}{r_{id}^3} - \frac{\mathbf{r}_d}{r_d^3} \right)} \\ &= -G m_d \sqrt{\frac{1}{r_{id}^4} + \frac{1}{r_d^4} + \frac{2\cos\beta}{r_{id}^2 r_d^2}}\end{aligned}\quad (4.138)$$

From the Figure 4.12 we get:

$$\cos\beta = \frac{r_d - r_i \cos\alpha}{r_{id}}; \quad r_{id}^2 = r_i^2 + r_d^2 - 2r_i r_d \cos\alpha \quad (4.139)$$

Using Eq. 4.26 and substituting in Eq. 4.25:

$$\mathbf{a}_P = -G \frac{m_d}{r_d^2} \sqrt{1 + \frac{1}{(1 - 2\gamma \cos\alpha + \gamma^2)^2} - \frac{2(1 - \gamma \cos\alpha)}{(1 - 2\gamma \cos\alpha + \gamma^2)^{3/2}}} \quad (4.140)$$

where, $\gamma = r_i/r_d$. Now for the case of an SC orbiting a celestial body, $r_d > r_i$ and therefore γ is always less than 1 but varies between a certain range with the motion of the SC and the asteroid. It can be seen from the Figure 4.12, α varies from 0° to 360° and from analysis of the Eq. 4.27 that the maximum perturbing accelerations occur at the angles 0° & 180° whereas the minimum accelerations occur at 90° & 270° which is intuitive.

The scalar potential representing this acceleration can be introduced as:

$$U_P = -G m_d \left(\frac{1}{r_{id}} - \frac{\mathbf{r}_i \cdot \mathbf{r}_d}{r_d^3} \right) \quad (4.141)$$

such that,

$$\mathbf{a}_P = \nabla U_P \quad (4.142)$$

If there are a number of bodies perturbing the SC, the potentials can be found for each individual body and then summed up to give the total perturbing acceleration (Scheeres 2012). Since this is already in the asteroid reference frame the perturbing torque can be given by:

$$\mathbf{T}_P = \mathbf{r}_i \times \mathbf{F}_P = \mathbf{r}_i \times m_i \mathbf{a}_P = \mathbf{r}_i \times m_i \sum_{d \neq i, k} \nabla U_P^d \quad (4.143)$$

Using Eq. 4.27 and comparing perturbing accelerations due to the sun or other planets, it can be seen that the ratio m_d/r_d^2 is approximately 10^4 to 10^6 times more for the sun as compared to any solar system planets. Therefore for simplicity the system can be considered as a three body system with just the sun as a source of the perturbing force.

4.10.3. Solar Radiation Pressure

SRP is another contributor to the disturbance torque on the SC. This force is, of course, zero when the SC is in the shadow of the target body. For most applications, onboard movable surfaces are commanded from the ground station rather than autonomous real-time control by the onboard computer. For this, the SC's surface is modelled to a collection of N plates of a particular surface area A , having specular reflection coefficient as α_r , diffuse reflection coefficient as α_d and absorption coefficient α_a . Let e_\odot be the vector from the plate to the sun, n be the normal vector from the plate and r be the position vector from the com of the SC to the point of pressure on the plate, all in the B frame. The angle between the normal vector from the plane and the vector from the plane to the sun is given by:

$$\cos \theta = \mathbf{n} \cdot \mathbf{e}_\odot \quad (4.144)$$

With this the force due to SRP acting on individual illuminated plates on the SC (Markley and Crassidis 2013) is as follows:

$$\mathbf{F}_{SRP}^i = -P_\odot A_i \cos \theta_i \left[2 \left(\frac{\alpha_d^i}{3} + \alpha_r^i \cos \theta_i \right) \mathbf{n}_i + (1 - \alpha_r^i) \mathbf{e}_{\odot,i} \right] \quad (4.145)$$

where, P_{\odot} is the solar radiation pressure. The total torque acting on the SC due to this force can be further given by:

$$\mathbf{T}_{SRP} = \sum_{i=1}^N \mathbf{r}_i \times \mathbf{F}_{SRP}^i \quad (4.146)$$

This has been established with respect to the body reference frame (B) and may need to be converted to different reference frames as per requirement.

4.10.4. Disturbances in the B Frame

In the earlier subsections we have discussed the various disturbing accelerations that need to be included in the mathematical model. In this section we will establish all of the accelerations and torques in the B frame to include them in the relative dynamics for the dual quaternion form.

Gravity

$$\mathbf{g}_A = -G \rho \sum_{e \in edges} \mathbf{E}_e \mathbf{r}_e L_e + G \rho \sum_{f \in faces} \mathbf{F}_f \mathbf{r}_f \omega_f \quad (4.147)$$

$$\mathbf{g}_B = \mathbf{q}_{B/A} \otimes {}^* \mathbf{g}_A \otimes \mathbf{q}_{B/A}^* \quad (4.148)$$

Solar Radiation Pressure

3^{rd} Body Perturbation

5

Fundamentals of Autonomous Guidance and Control

The trajectory planning, sensing and control of the SC is carried out by the onboard GNC to achieve SC manoeuvres and target pointing as required by the mission objectives. In the previous chapter, we discussed the the kinematics and dynamics of the SC, which dictate how the SC moves in space in response to different external forces or disturbances acting on it. The GNC system is responsible for the safe steering of the SC in response to the dynamics and kinematics. Simply put the navigation subsystem answers "*Where am I?*", the guidance subsystem "*Where am I going?*" and the control subsystem "*How do I get there?*". This chapter discusses the subsystems of guidance and control in further detail as applicable to the mission plan for this thesis.

For an asteroid mission the onboard G&C needs to deal with a highly dynamic and perturbed environment while meeting autonomy requirements to perform time urgent operations, complex fault responses and stringent pointing requirements. Mapping (Proximity operations) and touch and go (TAG) descent in these low gravity, atmosphereless small solar system objects are the future mission prospects as discussed in the second chapter. A six DOF G&C with non-linear trajectory optimization and adaptive filtering to respond to internal and external dynamic events enables the autonomy of the SC along with the target relative navigation. In this chapter, we will discuss the requirements for the mission phases of mapping and descent and the preliminary concepts required for *Motion Planning* and *Convex Optimization* to develop an autonomous guidance system using quaternions and dual quaternions.

5.1. Elements of GNC System

The GNC system as discussed is an advanced system that enables the SC to perform the required mission safely and precisely. In this section we discuss the fundamental components of GNC focusing on both orbiting and descent guidance. We will first define the function of the three subsystems and how they interact with each other and formulate a general guidance problem each for mapping and descent phases.

5.1.1. Definitions of Guidance, Navigation and Control

To develop a guidance algorithm, a clear and basic understanding of the three subsystems is necessary. Definitions for them have been adapted from ECSS-E-60A ([ecss2004](#)) and their interpretation for the mapping and descent phase have been elaborated. In the definitions, controller is synonymous with the GNC system.

Guidance function of the controller to define the current or future desired state.

It is a mathematical blackbox that calculates and commands the required acceleration profile for the SC to have the required attitude orientation and trajectory as per the mission phase. It enables the SC to achieve the desired end conditions.

Navigation function of the controller to determine the current or future estimated state from measured state.
The state is measured by means of onboard sensors like horizon or star sensors, cameras, sun sensors, IMUs (gyroscopes and accelerometers). The estimated state is obtained by means of navigation filters like the extended Kalman filter.

Control function of the controller to derive control commands to match the current or future estimated state with the desired state.

It is the onboard processing and routing of commands from guidance and navigation to activate actuators like thrusters, reaction wheels, control moment gyroscopes or aerodynamic surfaces for achieving reactive forces on the vehicle. This helps achieve the required spatial alignment and stabilization of the vehicle.

5.1.2. GNC Architecture and System Interaction

A basic GNC architecture has been shown in the Figure 5.1. This architecture is tailored as per the mission requirements of the SC. The guidance and control form a part of the mission vehicle management (MVM) also known as the control manager. It is responsible for appropriate mode selection of the GNC system. Modes here refer to different mission phase requirements, for example —. It is also bears the responsibility for the safety of the SC by fault identification, detection and recovery (FDIR) and to also put the GNC into its nominal or redundant mode. It therefore also selects the GNC hardware that need to run in these specific modes.

On an actual SC the attitude controller is responsible for the attaining the required SC attitude. It utilizes the reference state from the guidance and the measured state from the navigation and the difference between the two is converted to commands for the actuators like reaction control wheels or thrusters to execute. But this command has to be within the capabilities of the actuators. There needs to be proper selection of the combination of thrusters. The thrust vector can be controlled by using different combination of thrusters or a gimballed thrusters and the thrust magnitude by throttle control or switching the thrusters on and off.

The navigation system hardware measures the real state of the SC in the presence of disturbances. It measures the real position, velocity, attitude and angular rates of the SC. Meanwhile the navigation filter estimates all these optimally. These are then provided in the feedback loop of the GNC system to make the necessary adjustments or corrections in the next iteration or time step. The measurements are prone to noise in the instruments due to various reasons and the estimate can only be obtained with a certain accuracy. Hence navigation errors are unavoidable and their impact on the achievable guidance precision and precision in the command execution need to be kept in consideration.

As can be seen the guidance system provides the command to point the SC in the required direction or to follow a certain trajectory by using the best possible estimate of the current state of the SC. In this fashion it guides the SC through space and time from the current state to the desired state.

5.1.3. Separating Guidance from Navigation

The discussion in the above subsection brings us to the question if the guidance and control logic can be developed by treating them as a separate entity from navigation. Pfeiffer 1968 discusses the consequences and assumptions for separating the guidance and navigation as presently is the practice of developing guidance algorithms. The navigation system as we discussed is prone to measurement noises and also the real system undergoes disturbances which cannot be perfectly modelled and hence there is process noise. Even though the measurement and process noise is taken care of in the navigation filters, its not perfect and as a result the

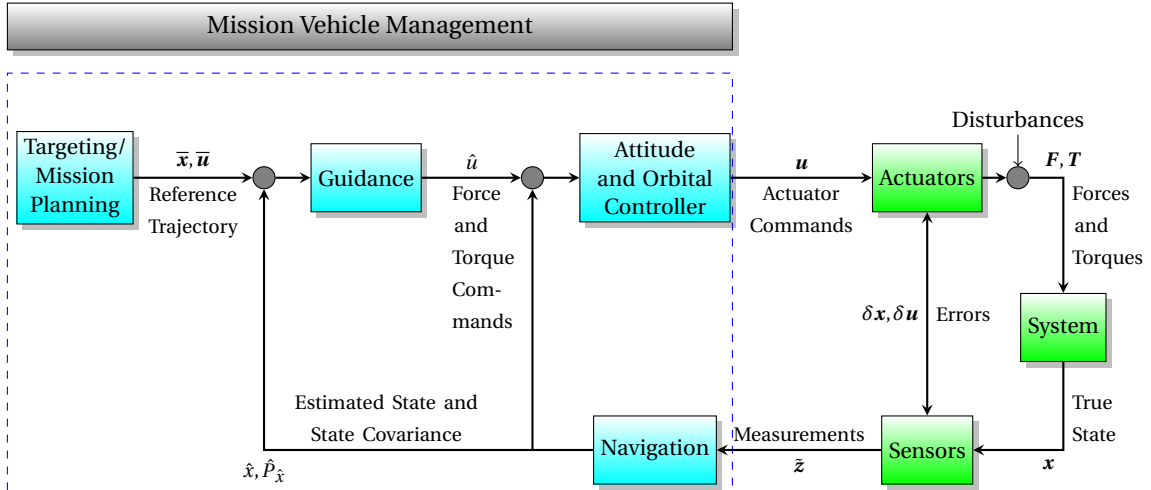


Figure 5.1: GNC System Architecture and Interaction

state is not known perfectly and cannot simply be defined by the position, velocity and system parameter vectors. The state needs to be defined additionally with statistical moments of distribution of these parameters which leads to the problem becoming a stochastic control problem. Developing a deterministic guidance for such a problem would therefore be incorrect.

To develop a guidance algorithm separately from the navigation as a deterministic optimizer, certain assumptions need to be made. Pfeiffer 1968 discusses that in case that the random navigation errors and random systematic errors are small, stochastic guidance analysis is not required. Also in case the execution of the guidance is with continuous thrust, stochastic treatment is not required. However in case of sequence of small thrust operations at unspecified times we cannot assume the problem to be deterministic. For the descent phase since we deal with continuous thrust we can develop the guidance as deterministic.

Although we assume the guidance problems to be deterministic, sensitivity analysis will be performed at the end of the thesis with the help of the relative navigation system developed by Razgus 2017. Therefore we can quantify the impact of the precision of the navigation on guidance. Therefore the cost of assuming the problems to be deterministic can be found out. A benefit of this is that the guidance algorithms could be tuned to be more robust and less sensitive to navigation errors.

5.1.4. General Guidance Problem

In this section we provide the general 3DOF guidance problem for both the phases of mapping and guidance. In the mapping phase guidance plays the role of designing the optimal trajectory to maximise asteroid observation by the SC and for the descent phase guidance has the task of computing a suitable acceleration profile so the SC can achieve the desired end state or conditions. Hence the mapping guidance problem will be posed as the initial value problem (IVP) whereas the descent phase as a two-point boundary-value problem (TPBVP). The two problems are illustrated in Figure 5.2 and stated below as Problem 1 and Problem 2.

► PROBLEM 1a: Mapping phase general guidance problem

Given: Initial states at time $t = t_0$

$$\mathbf{r}(t_0) = \mathbf{r}_0, \quad \mathbf{v}(t_0) = \mathbf{v}_0 \quad (5.1)$$

where $\mathbf{r}(t)$ is the position at time t and $\mathbf{v}(t)$ the velocity, find an acceleration profile and thus a trajectory

$$\mathbf{a}(t) = \frac{\mathbf{T}(t)}{m(t)}, \forall t \in [t_0, t_f] \quad (5.2)$$

where $\mathbf{a}(t)$ is the acceleration, $\mathbf{T}(t)$ is the thrust, $m(t)$ is the instantaneous spacecraft mass, and t_f is the final time, such that the spacecraft reaches a final state

$$\mathbf{r}(t_f) = \mathbf{r}_f, \quad \mathbf{v}(t_f) = \mathbf{v}_f \quad (5.3)$$

with some given constraints

$$\begin{aligned} \mathbf{g} &\leq 0 \\ \mathbf{h} &= 0 \end{aligned} \quad (5.4)$$

This problem is usually solved analytically during mission planning and the mission profile is already onboard the SC to follow through directly. In this thesis we will extend on the novel method *-sampling based motion planning-* to enable the SC solve this problem autonomously in real time.

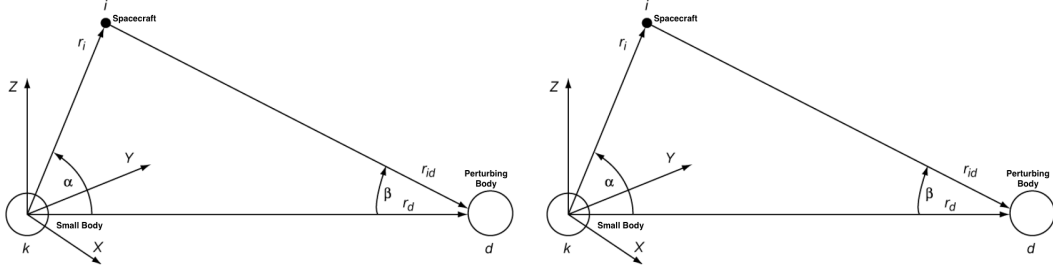


Figure 5.2: Guidance problems for mapping (IPBVP) and descent (TVP). Simplified representative sketch.

► PROBLEM 2a: Descent phase general guidance problem (fixed time)

Given: Initial state at time $t = t_0$

$$\mathbf{r}(t_0) = \mathbf{r}_0, \quad \mathbf{v}(t_0) = \mathbf{v}_0, \quad m(t_0) = m_0 \quad (5.5)$$

where $\mathbf{r}(t)$, $\mathbf{v}(t)$ and $m(t)$ are the position, velocity and mass of the SC at time t . The objective is to find an acceleration profile which in turn results in a trajectory

$$\mathbf{a}(t) = \frac{\mathbf{T}(t)}{m(t)}, \quad \forall t \in [t_0, t_f] \quad (5.6)$$

where $\mathbf{a}(t)$, $\mathbf{T}(t)$ and $m(t)$ are the acceleration, thrust and instantaneous SC mass at time t and t_f is the final time. The final state of the spacecraft is therefore given by,

$$\mathbf{r}(t_f) = \mathbf{r}_f, \quad \mathbf{v}(t_f) = \mathbf{v}_f, \quad t_f \text{ given} \quad (5.7)$$

The system is defined by some constraints which could be on the state or control as below,

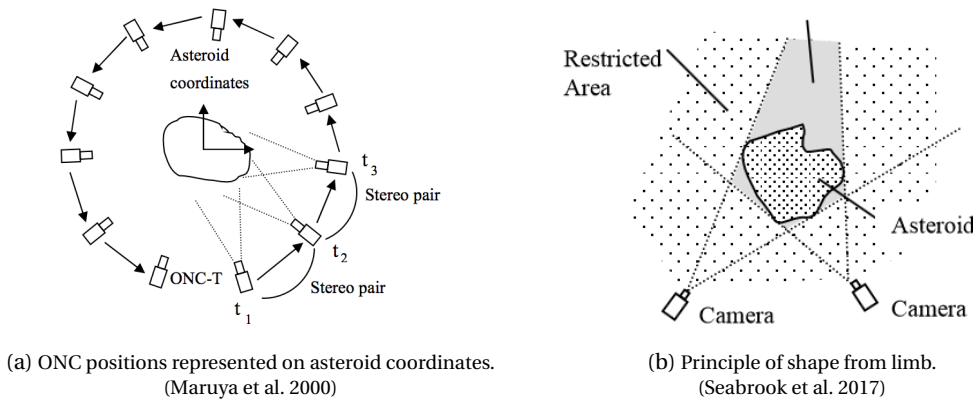
$$\begin{aligned} \mathbf{g} &\leq 0 \\ \mathbf{h} &= 0 \end{aligned} \quad (5.8)$$

This problem has been solved using many different methods but the most promising method so far has been that of convex optimization. In this thesis we will work with a novel hybrid approach of an extension of this method -*successive convexification*- and -*dual quaternions*- to analyse the advantages and disadvantages of such a combination for autonomous SC operation in real time.

5.2. Technological Considerations for Autonomous G&C

The orbits of asteroids, their detection and visualisation as well as other physical properties are presently studied with the help of ground based telescopes or Earth satellites or flyby spacecrafcts. After an asteroid has been studied, mission profiles are designed ensuring safety in missions and predetermined trajectories and mission completion times. This makes the mission dependent on human intervention in case of unforeseen circumstances. Due to the massive distance between small bodies and Earth communication delay in real time becomes a bottle neck in critical situations, as we have seen in the case of the Philae lander for Comet 67P from Rosetta. This has called for the autonomy in future asteroid missions which begins with relative navigation and guidance. This enables the SC to take decisions in case of unforeseen circumstances for ensuring mission safety.

With the previous sections describing the fundamental concepts of guidance and control, it can be seen that the system is very complicated and would have specific technological requirements for performing the mission objectives during the mapping and descent phase. In the mapping phase, the general surface topography needs to be generated in order to select landmarks for the next phase of descent. This calls for certain system requirements to obtain a resolution of the surface images that would suffice for hazard detection. During the TAG sequence, the descent has to be precise for safe sample collection such that it can thrust itself away from the surface afterwards for a successful ascent. The SC should be enabled to evade hazards in



case of undetected hazard in the mapping phase due to limitations on the resolution. We will discuss these concepts in detail in this section.

5.2.1. Reasons for High Resolution Imaging and Precise Ranging

The shape of the asteroid are based on observations from Earth satellites or ground telescopes, it makes the mapping of the asteroid critical to ensure a safe landing location. Hence to ensure a safe and successful descent to the asteroid an accurate estimation of the relative motion between the SC and asteroid and its shape is required. This requires the SC to be capable of navigating relative to the asteroid. This is achieved with the help of navigation sensors like star trackers (STTs), inertial Reference Units (IRUs), optical navigation cameras (ONCs), LIDAR and Laser range finder (LRF). The actual purpose of all these sensors have been discussed in brief in the Section 5.1.2. Our first mission objective is global mapping of the target asteroid. With the available technologies at present, two methods exist: "optical imaging to estimate the motion and shape of the asteroid (Sawai et al. 2001)" or "shape model construction using laser altimeters (Seabrook et al. 2017)".

Optical Imaging

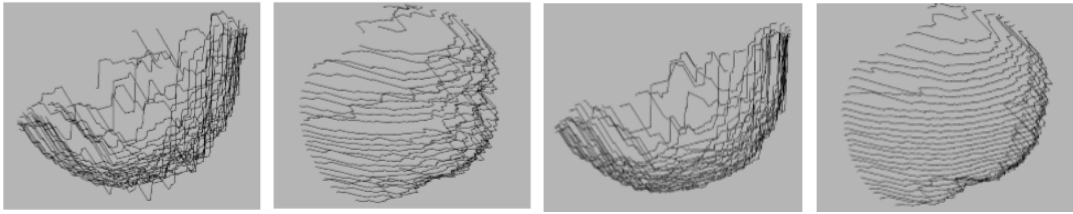
Motion estimation can be carried out by means of Global Control Points (GCPs). The SC uses the ONCs to estimate the asteroid relative motion by tracking feature points (GCPs) on the asteroid surface. The coordinates of the GCPs in the asteroid frame can calculated from the ONC images. Equations that are used to calculate the asteroid motion in terms of the camera coordinates can be found in Maruya et al. 2000.

The 3D model is built using a technique called the *motion stereo method* (Sawai et al. 2001). The ONCs image the asteroid from different viewpoints. The SC maintains a hovering position and uses the asteroid rotation to obtain multi-viewpoint images as shown in Figure 5.3a. Computations for the global mapping are performed on these images using the motion stereo technique which can be found in detail in Sawai et al. 2001 pg. 3. The accuracy of this method is reliant on the surface texture of the asteroid, which means in the absence of distinctive texture, the matching results are erroneous. To achieve the required accuracy in such situations the principle of shape from limb is used. The asteroid image obtained from the ONCs is divided into an asteroid region and background region as shown in Figure 5.3b. The 3D object area containing the asteroid is computed from the asteroid region and the restricted area that holds no intersection with the asteroid from the background region. Since multi-viewpoint images are taken, circumscribed polygons can be obtained from the 3D object areas. Using circumscribed polygons increases the matching accuracy by reducing the matching errors that expand the map. The stability of this technique is high but it fails to prove itself in concave regions.

Another parameter that affects the accuracy of this mapping technique is the asteroid surface reflection. The rotation of the asteroid affects the intensity of the reflected light from its surface since the incidence and emission angles change with its rotation. This leads to the requirement of modelling the reflection. There are two existing models; Hapke and Lambertian, the latter being less precise. The Lambertian model is dependent on only the incidence angle given by the equation:

$$I = k \cos(i) \quad (5.9)$$

where, I , k and i are the intensity of a point, constant coefficient and incidence angle respectively. The Hapke model as described in Hapke 1986 has two specific characteristics that make it more accurate, firstly



(a) Wire frame representation of matching with Lambertian reflection. (Sawai et al. 2001)

(b) Wire frame representation of matching with Hapke reflection. (Sawai et al. 2001)

the intensity curve has its peak at the equivalence of the incidence and emission angles called the *opposition effect* and secondly the change in the intensity which changes in the incidence angle outside the area of the opposition effect is relatively small. The difference in matching accuracy using the two reflection models is shown in Figure 5.4a and 5.4b.

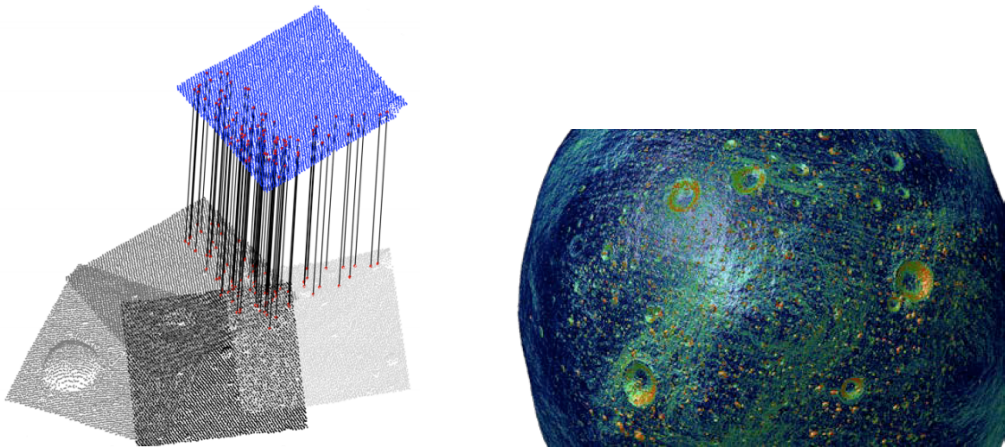
Laser Altimetry

A Laser Ranger (LR) or Light Detection and Ranging (LIDAR) measures the distance to the target by illuminating it with light or laser pulses. This optical remote sensing technique measures the time of flight of the light pulse from the emitter to the target surface and back to the receiver to determine the distance to the target. Laser altimetry is nothing but the same principle and can be used to construct the topographic map of the asteroid. The navigation LIDAR is present in conjunction with the Laser altimeter used for asteroid mapping, which can be used to provide precision ranges as part of the data input for the navigation solution. The laser altimeter is capable of taking high resolution raster scans of the surface. While the SC orbits the target small body, overlapping scans across its entire surface are obtained. This high resolution spatial data set generates a high fidelity shape model of the target body.

The altimeter can send pulses in the required direction by means of an inbuilt scanning mirror. The origin and direction of these pulses as well as the mirror scan patterns can be predetermined, but with autonomous navigation the MVM can be made capable of commanding them based on the current orbit orientation. The images from the received pulses are a set of overlapping raster scans that need to be adjusted in a reasonable amount of time to construct the asteroids shape. For faster computations, keypoints are generated for the matching method to find common features. These keypoints are generally surface features that can be obtained from the point clouds using a mapping tool which is very beneficial since they can be used for hazard avoidance later on during the descent phase. As can be said intuitively this reduces the data points to be processed massively for the point cloud registration process. The first step is to sequentially correct the offsets from the overlapping data using rotational and translational transformations. Using one set of keypoints as a baseline (usually the first data registration) a keypoint shape is generated one cloud at a time. Then the set of keypoints with largest number of feature matches with the baseline is searched. Least squares is used to minimize the distance between the baseline and the current keypoint set to transform them rigidly. This can be seen in Figure 5.5a. All the raster scans with these matching keypoints are exhausted and then the next baseline is chosen. These alignment errors get accumulated and propagated by this sequential method. In order to minimise these errors they are distributed globally and a final registration of each data set position is performed using a General Procrustes Analysis¹ (GPA). This results in data set largely self-consistent while adding the raster scans and building it into a close shaped model. After the errors are minimised the mapping tool is used to construct a grid shaped model. A simulation by OLA; the laser altimeter onboard Osiris-Rex of the asteroid Bennu is shown in Figure 5.5b.

There can be a discrepancy in the measurement due to attenuation or dispersion of the signal due to reflection off dust and irregular surface of small bodies. These errors can be handled with the reflection models, Hapke or Lambertian. Errors in determining the distance also depend on the wavelength, power, pulse width of the laser pulse and other factors like the secular or non-smooth surfaces, measurement error of the rotating mirror angle and the clock error. These errors can be mathematically modelled to be taken care of prior to the mission.

¹GPA is an iterative algorithm that uses reduction in the sum of squared differences between original and adjusted positions.



(a) Point cloud registration (OLA) using sequential keypoint matching. (Seabrook et al. 2017)

(b) A simulated OLA scan of the asteroid surface. (Dickinson et al. 2012)

5.2.2. Reasons for Hazard Detection

Hazard detection and avoidance (HDA) is key to safely landing an SC on the surface of any target body. In the past missions have been lost to landing in hazardous areas and therefore it became a need for any space mission which had the objective of extremely close proximity operations. In case of small body missions the complexity for the HDA increases since apriori surface information of the target body is not available and neither is communication from Earth without delay, unlike Lunar landers or Mars landers. It becomes a need to have an onboard algorithm for the SC to be self aware of the possible hazardous locations and avoid them as sites for landing or descent.

The high resolution images obtained during the asteroid mapping either by optical or laser imaging play a very important role in HDA. As can be seen from the current state of the art instruments resolution of the surface in the range of centimetres can be obtained. This helps provide information about surface features like slopes, boulders, rocks, craters, regolith areas etcetera in real time. A comparison for the various algorithms for crater recognition which can be used in the mapping tool can be found in Woicke et al. 2018 and similar algorithms exist for other surface features as well. The SC is therefore able to characterize the observed surface well before landing or descent and can choose landing sites while mapping itself. This increases the probability of a safe landing before the close proximity of the SC to the asteroid. Although fail safe methods need to be accommodated in the automatic HDA for the SC to be able to avoid a hazardous landing site when it is already on its optimised descent path and re-optimize for a new safe landing site.

5.2.3. Reasons for Precision Descent/Landing

As we have already established, for descent or landing on a small body the autonomous navigational accuracy has to be high. Along with the autonomy for descent/landing, the system must have the flexibility guide the SC to a desired targeted point on the surface with zero velocity or minimal velocity. The most important reason for precision descent is safety of the SC. Descending to or landing on hazardous surface feature would risk failure of the mission. In the case of a TAG descent, the main objective is sample return. This means the SC has to approach the surface safely whilst also being able to leave safely. Such a mission to asteroids in the NEA region (3 AU) entitles the SC to have larger solar panels (length of 14m for Rosetta). As can be seen precision landing becomes a need to avoid any kind of damage to the SC for return.

As discussed in the scientific objectives of a small body mission, a sample return is needed to study the target bodies internal structure and sub surface materials. This would shed light on the formation history of the asteroid while helping understand the processes in the formation stages of the solar system. For sample collection from an asteroid, a site that has regolith or loose rocks will not be chosen since they have undergone weathering due to physical or chemical processes. A site with a conjugated surface is chosen, that has to be loosened by an impactor for the SC to be able to collect samples from deeper regions in the impact area that are still pristine. This requires the SC to precisely descend to a range above the selected impact site. The impact area is usually in the range of a few metres (Tsuda, Yoshikawa, Saiki, et al. 2017) depending on the asteroid size as well as structure. Once the detonation on the target site is achieved and the ejecta has settled or its velocity is low the SC descends to collect the sample. The impact area therefore constraints the descent

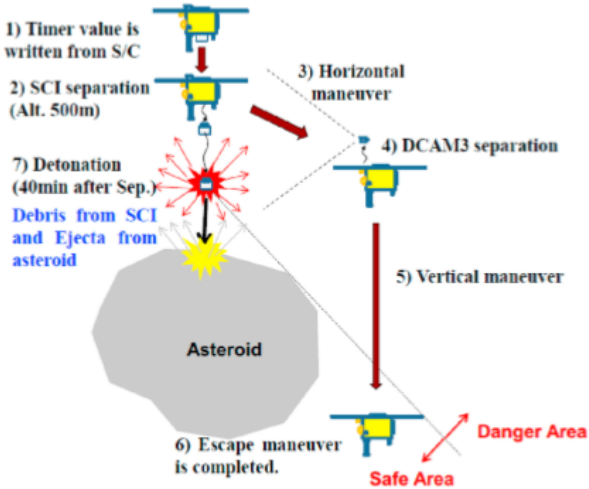


Figure 5.6: Kinetic Impact Operation Sequence of Hayabusa for sample collection. (Tsuda, Yoshikawa, Saiki, et al. 2017)

area of the SC calling for precision. The current Hayabusa 2 mission impact and sample collection profile is shown in Figure 5.6

5.2.4. Relevance to the Guidance System

The technological discussions in the prior subsection do not explicitly discuss their relation to the guidance problem and we will try to establish this in this subsection. High resolution images of the asteroid are reliant on the capability of the optical cameras or laser altimeter and the navigational accuracy similarly precision landing is dependent majorly on navigational accuracy and HDA is dependent on the instruments being used for observation. But these requirements translate to the guidance algorithm in the form of constraints or assumptions that need to be established before solving the optimal control problems of mapping and descent.

- For high resolution imaging, if the mission system design opts for optical imaging, constraints occur on the state space of guidance due to lack of visibility in shadow regions whereas for laser altimetry this constraint need not be forced. Also there has to be a constraint on the altitude of the SC for consistent imaging.
- For generating the image patches or point cloud maps, the vision based technologies must always be pointed towards the target body, which requires a constraint on the attitude of the SC. Also for overlapping image patches or raster scans, the angular rate of the SC attitude has to be constrained below a certain value depending on the instrument specifications.
- For HDA, the guidance algorithm of the SC should incorporate a logic for diversion and re-optimisation of trajectory in case the landing site is found to be dangerous. Since this situation leads to more expense of propellant, the algorithm must also be very efficient.
- For precision descent, the target site should always be in the field of view of the SC which again constrains the attitude while descent. Also the propellant expulsion actuator/s need to be gimballed or the SC attitude changed to obtain required velocities at required distances from the target body.

As we can see, the high resolution imaging, HDA and precision descent directly impact the guidance making it complex and dependent on many computational resources. The developed autonomous guidance should be able to handle these complexities in combination whilst being efficient.

5.3. Global Mapping Phase

In the mapping phase the guidance subsystem has to generate a trajectory or number of trajectories for the SC to follow in order to observe the entire target body. It has to take care of the attitude of the SC such that the target body is never out of sight and within a certain constrained viewing angle for generating an accurate

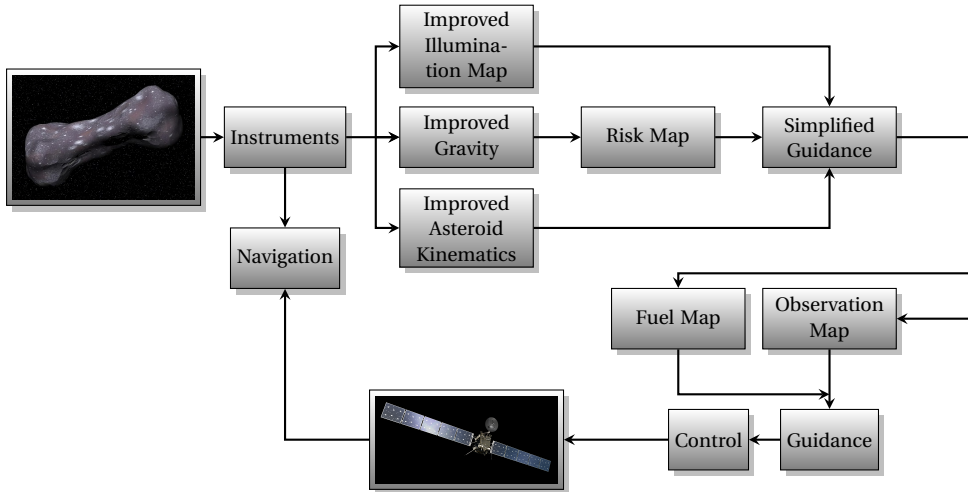


Figure 5.7: Top level GNC architecture for global mapping of the small body

map. Also maintaining the desired altitude is necessary whilst orbiting or performing orbital manoeuvres around the asteroid to generate high resolution maps.

Utashima 1997 in his study has presented with SC orbits possible around asteroids in order to observe them globally with high resolution. There are two types of orbits possible for mapping the asteroid, frozen and polar orbits. Frozen orbits are those whose Keplerian mean elements do not change given that solar radiation pressure is the only disturbance. Two kinds of frozen orbits are possible, one in the orbital plane of the asteroid and the other called the solar plane-of-sky orbit is an orbit that always faces the sun. The prior one is not adequate for high resolution observation whereas the latter can be adequate for very small bodies with radii below 2-3 km. In case the altitudes of these orbits are lowered, they are highly sensitive to the oblateness of the asteroid and the frozen orbits need to be maintained by maneuvers costing $\approx 100 \text{ m/s}$ for a year's worth of maintenance.

Polar orbits on the other hand are best suited for global mapping which negate the effect of the asteroid's oblateness. Also the only maintenance required is to make the eccentricity zero. It has also been proved if the ratio of characteristic angular velocity due to the radiation pressure to that from oblateness multiplied by the limit for eccentricity is less than 1, maintenance is not required at all for polar orbits.

In the recent mission of MUSES-C to Ryugu, the SC hovered at a distance of 20 km from the asteroid for ≈ 20 days to completely map it². In the OSIRIS-Rex mission to Bennu, the detailed survey phase where mapping of the asteroid is planned, the SC conducts hyperbolic flybys with a closest approach of 3.5 km over four specific locations(GalEdd and Cheuvront 2015). Images and laser altimetry from each of these locations for a complete asteroid rotation is conducted. These provide with resolution of the surface features upto $\approx 21 \text{ cm}$ and accuracy of the map within $\approx 5 \text{ m}$ (Beshore et al. 2015). Then it conducts 5km flybys to study the geometry for details of the the surface properties from locations above the equator with independent illumination angles (due to multiple local times of day on the surface). By the end of this phase 12 sampled sites are identified for sample collection.

The mission design of Osiris-Rex provides more autonomy to the SC, to map and select a landing site and in this thesis we will focus on the same. As discussed in the heritage we would approach this problem with *sampling based motion planning optimisation* to reduce the propellant cost and time cost to reduce the period of topographic mapping whilst being within a limited Δv utilisation. We will approach this problem using dual quaternion relative states which has not been done before.

5.3.1. Basic Mapping GNC framework

The basic architecture for the global mapping is presented in Figure 5.7. As shown in the flow, the initial navigation with the help of onboard instruments (Initial Survey phase) provides with better maps of illumination, gravity, rotation, mass, density and size of the asteroid. This is then fed to generate a risk map to prevent escape of the SC from the asteroid gravitational field helping constrain the propellant expulsion actuator from exceeding thrust values. This is fed then to a simplified guidance logic that can be used to generate cost maps

²<http://global.jaxa.jp/projects/sat/hayabusa2/topics.html#topics12394>

of fuel and observation. Once these initial maps are obtained they can be fed to the actual guidance algorithm to calculate trajectories and provide the required control inputs to the actuators. The SC then follows the trajectories, with errors in its state from limitations of modelling various perturbations and actual actuator control outputs. These are estimated by the navigation system and fed back to the MVM to decide on whether new trajectories need to be calculated.

5.3.2. Refined Problem Formulation

With the mission scenario established, the mapping problem is reformulated. The guidance problem for mapping can be defined as:

The guidance problem for global mapping can be defined as finding a number of fuel optimal trajectories from a given initial state (pose and attitude) to observe the entire surface of the asteroid ensuring satisfactory illumination of the patch under observation and avoiding any collision with the asteroid whilst being under a variable gravity field and acted on by disturbances due to solar radiation pressure and 3rd body perturbation.

► PROBLEM 1b: Refined mapping phase 6-DOF guidance optimisation problem

$$\text{minimise } f(\Delta v_{B/I}^I(t)) + f(r^I(t), t_{obs})$$

subject to:

Kinematics:

$$\dot{\mathbf{r}}^I(t) = \mathbf{v}_{B/I}^I(t), \quad \dot{\mathbf{q}}_{B/I}(t) = \frac{1}{2}\boldsymbol{\omega}_{B/I}^B(t) \otimes \mathbf{q}_{B/I}(t)$$

Dynamics:

$$\begin{aligned} \ddot{\mathbf{r}}_{B/I}^I(t) &= \frac{\mathbf{T}^I(t)}{m(t)} + \mathbf{g}_I \\ \dot{\boldsymbol{\omega}}_{B/I}^B(t) &= J^{-1}(\mathbf{r}_B(t) \times \mathbf{T}^B(t) - \boldsymbol{\omega}_{B/I}^B(t) \times J\boldsymbol{\omega}_{B/I}^B(t)) \end{aligned}$$

Control Constraints:

$$\|\Delta \mathbf{v}_{B/I}^I(t)\| \leq \Delta v_{max}$$

Boundary Conditions:

$$\begin{aligned} \mathbf{r}^I(0) &= \mathbf{r}_0^I, \quad \mathbf{v}_{B/I}^I(0) = \mathbf{v}_{B/I_0}^I \\ \mathbf{q}_{B/I}(0) &= \mathbf{q}_{B/I_0}, \quad \boldsymbol{\omega}_{B/I}^B(0) = \boldsymbol{\omega}_{B/I_0}^B \end{aligned}$$

Additional Constraints:

$$M_c = f(n, t_{obs})$$

where, t_{obs} is the time for which a particular patch is observed, n is the number of patches to be observed and M_c is the mission completion status.

5.4. Touch and Go Descent Phase

In the descent phase the guidance subsystem has to generate a trajectory from the last position of the mapping phase to the selected landing site. It also needs to maintain its attitude within certain bounds to make sure that the target body is in sight. The HDA system is still active in this phase to make sure in case of contingency that a retargetting is initiated for the guidance algorithm to reevaluate for a new optimal trajectory. It would generate the required acceleration profiles for this and provide it to the control subsystem to execute them. While generating the acceleration profiles it also needs to take care of the control actuator limitations.

The TAG descent requires a combination of long ascent thrusts while preserving a desired safe attitude to prevent contact with the surface of the target body. These require a tight coupling between the trajectory and attitude control and a six DOF G&C (3 for the position, 3 for the attitude) (Xinfu, Ping, and Binfeng 2017). As discussed in the optimisation algorithm heritage, we would approach this problem with *successive convexification*. Advantages of this method are that it guarantees convergence for a well-posed convex problem, the solution is the global optimum and is a solution to the original problem, a number of efficient solvers have been developed for this kind of problem and constraints and penalties can be imposed. The novel method of this thesis is the combination of the descent problem in the form of a convex problem using dual quaternions with relative states.

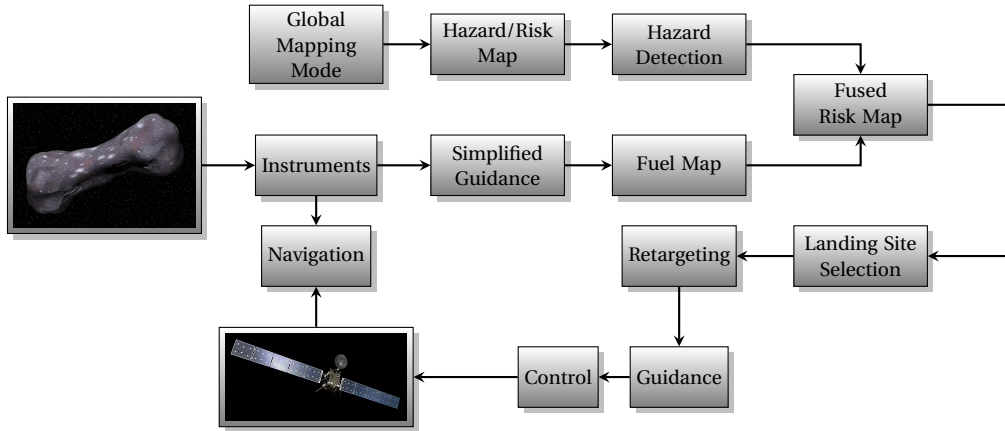


Figure 5.8: Top level GNC architecture for descent to the small body

5.4.1. Basic Descent GNC framework

The basic architecture for the descent is presented in Figure 5.8. As shown in the flow, the detailed survey during global mapping provides with the hazard map and is fed to the HDA system. The onboard instruments enable navigation and together with the hazard map, the simplified guidance provides a fuel map. The fuel map and hazard map are used by the MVM to make the final landing site selection. The HDA is still active after the final landing site selection and retargeting is still possible. The guidance then generates the optimal propellant consumption trajectory from the initial location to final location. From this the control inputs are provided to the thrusters. The true state of the SC is estimated by the navigation.

5.4.2. Refined Problem Formulation

The descent problem is reformulated using the mission scenario. The guidance problem for precision power descent has been phrased by Açıkmese and Ploen 2007 as below:

The powered descent guidance problem for pin-point landing is defined as finding the fuel optimal trajectory that takes a lander with a given initial state (position and velocity) to a prescribed final state in a uniform gravity-field, with magnitude constraints on the available net thrust and various other constraints.

The definition is for a 3DOF problem but holds true for 6 DOF as well. The "uniform gravity-field" refers to a constant gravitational acceleration or a flat-body model but in our case we will replace it with the variable gravity field in the problem formulation in Chapter 7.

► PROBLEM 2b: Refined descent phase 6-DOF guidance optimization problem

minimize $m(t_f)$

subject to:

Kinematics:

$$\dot{\mathbf{r}}_I(t) = \mathbf{v}_I(t), \quad \dot{\mathbf{q}}_{B/I}(t) = \frac{1}{2} \boldsymbol{\omega}_{B/I}^B(t) \otimes \mathbf{q}_{B/I}(t)$$

Dynamics:

$$\begin{aligned} \dot{m}(t) &= -\alpha \| \mathbf{T}_B(t) \|, \quad \dot{\mathbf{v}}_I(t) = \frac{\mathbf{T}_I(t)}{m(t)} + \mathbf{g}_I \\ \dot{\boldsymbol{\omega}}_{B/I}^B(t) &= J^{-1}(\mathbf{r}_B(t) \times \mathbf{T}_B(t) - \boldsymbol{\omega}_{B/I}^B(t) \times J \boldsymbol{\omega}_{B/I}^B(t)) \end{aligned}$$

Control Constraints:

$$T_{min} \leq \| \mathbf{T}_B(t) \| \leq T_{max}$$

Boundary Conditions:

$$\begin{aligned} m(0) &= m_{wet}, \quad \mathbf{r}_I(0) = \mathbf{r}_{I_0}, \quad \mathbf{r}_I(t_f) = \mathbf{r}_{I_f}, \quad \mathbf{v}_I(0) = \mathbf{v}_{I_0}, \quad \mathbf{v}_I(t_f) = \mathbf{v}_{I_f} \\ \mathbf{q}_{B/I}(0) &= \mathbf{q}_{B/I_0}, \quad \mathbf{q}_{B/I}(t_f) = \mathbf{q}_{B/I_f}, \quad \boldsymbol{\omega}_{B/I}^B(0) = \boldsymbol{\omega}_{B/I_0}^B, \quad \boldsymbol{\omega}_{B/I}^B(t_f) = \boldsymbol{\omega}_{B/I_f}^B \end{aligned}$$

Attitude Constraints:

$$\zeta_1 \geq \theta_o \geq \zeta_2$$

where, $\dot{m}(t)$ is the mass flow, α is the thrust-to-mass flow conversion factor, T_{min} and T_{max} are the lower and upper bounds on the magnitude of thrust, ζ_1 and ζ_2 are real numbers and θ_o is the viewing angle between the LOS of the camera and landing site.

6

Sampling Based Motion Planning

The concept of Motion Planning has been developed for robotics and artificial intelligence planning. It is nothing but the name itself means, planning the motion of an object. In a simple scenario it can be defined as figuring out a trajectory that links two static positions while avoiding obstacles. The problem can therefore be charted via discretization and a solution can be found using graph search methods like A^* or Rapidly Exploring Random Trees. This area was fundamentally developed for robotics and now has applications in autonomous ground and air vehicles. The main difference in the focus of robotics was the kinematics of the system whilst the latter applications involve spatiotemporally consistent system dynamics. It was developed likewise on the lines of control theory having feedback policies enabling adaptive response during execution and a focus on stability to ensure that the system dynamics do not drive it out of control.

In recent works an emphasis on optimisation of resource consumption like energy and time has been established. Also uncertainties in the system model or control system can be taken into consideration. Trajectory smoothing can also be applied at the end to satisfy all the constraints of the complete continuous system. It can be seen that with these factors the complexity of even the simple scenario put forth previously is substantially increased. For the mission of asteroid mapping, the trajectory should satisfy observational requirements, whilst satisfying a minimum fuel consumption.

Configuration Space

Reachability

Sampling Based Planning

6.1. Predictive Model

6.2. Abstract Reachability

6.3. Map Computation

6.4. Planning

7

Successive Convex Optimisation

Mathematical optimisation finds the best solution (maxima or minima) out of feasible solutions for a given problem. The standard formulation of an optimisation problem is as follows (Boyd and Vandenberghe 2010)

$$\begin{aligned} & \text{minimise} && f_0(x) \\ & \text{subject to} && g_i(x) \leq b_i, \quad i = 1, \dots, m. \\ & && h_j(x) = c_j, \quad j = 1, \dots, p. \end{aligned} \tag{7.1}$$

where, $x = (x_1, \dots, x_n)$ is the *optimisation variable* of the problem, $f_0 : \mathbb{R}^n \rightarrow \mathbb{R}$ is the *objective* function of the variable which needs to be optimised (minimised in the case above). The objective function is subject to the functions $g_i : \mathbb{R}^n \rightarrow \mathbb{R}$ and $h_i : \mathbb{R}^n \rightarrow \mathbb{R}$ are the *inequality* and *equality* constraints and the constants b_1, \dots, b_m and c_j, \dots, c_p are the bounds on them. The solution of this problem is given by a vector x^* which gives the minimal value of the objective function whilst satisfying all the constraint equations such that,

$$f_0(x^*) \leq f_0(z) \quad \forall z \in \mathbb{R}^n \quad \text{with} \quad g_i(z) \leq b_i \quad \& \quad h_j(z) = c_j \tag{7.2}$$

The optimisation problem is classified as *linear* or *nonlinear* depending on the form of the objective and constraint functions. A linear program has objective and constraint functions that satisfy:

$$g_i(\alpha x + \beta y) = \alpha g_i(x) + \beta g_i(y) \quad \forall x, y \in \mathbb{R}^n \quad \alpha, \beta \in \mathbb{R} \tag{7.3}$$

The small solar system body descent problem is plagued with non-convex constraints as well as nonlinearities due to time varying gravity fields and other perturbing forces. We can therefore no longer apply methods to solve linear problems directly. This chapter walks us through the process of convex optimisation and how it can be utilized by successively convexifying non-linear or non-convex problems. The Figure 7.1 provides with the logical flow of this chapter.

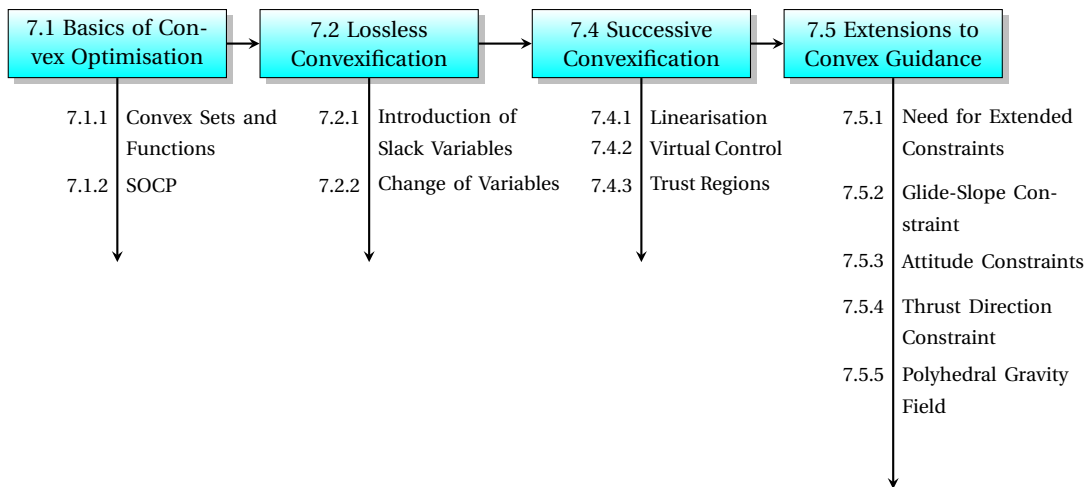


Figure 7.1: Chapter Overview

7.1. Basic Concepts of Convex optimisation

Convex optimisation is a rather young development as compared to well established methods like least squares or linear programming and was explored to the current status mostly in the 20th century. In this short period it has proved its worth with numerous beneficial properties. Açıkmeşe and Ploen 2007 presented their work to find a soft-landing guidance algorithm for a powered descent on Mars implementing convex optimisation. Since then there have been quite a few developments in the treatment of the powered descent problem as discussed in the Chapter 2. We will discuss some basic concepts in this section and work our way towards understanding the presently developed algorithms and finally formulate the problem using successive convexification using dual quaternions.

7.1.1. Convex Sets and Functions

A convex optimisation problem calls for convex objective and constraint functions which means they should be of the form:

$$g_i(\alpha x + \beta y) \leq \alpha g_i(x) + \beta g_i(y) \quad \forall x, y \in \mathbb{R}^n \quad \alpha, \beta \in \mathbb{R} \quad \alpha + \beta = 1, \quad \alpha \geq 0, \beta \geq 0 \quad (7.4)$$

A function is therefore convex if the function of the weighted average is less than or equal to the weighted average of the function. As can be seen from the form of convex objective or constraints, convex problems are nothing but a generalization of linear problems by replacing the equality by inequality and with a restriction on α and β .

Convex sets are fundamental to understanding the theory of convex optimisation and hence will be discussed briefly. First we define a line segment between two points $x_1, x_2 \in \mathbb{R}^n$ and $x_1 \neq x_2$ as:

$$y = \theta x_1 + (1 - \theta) x_2, \quad \theta \in \mathbb{R}, \quad 0 \leq \theta \leq 1 \quad (7.5)$$

An *affine set* is such that a line through any two points in the set lies in the set itself, meaning that a set, $\mathcal{C} \subseteq \mathbb{R}^n$ is an *affine set* if for any $x_1, x_2 \in \mathcal{C}$ and $\theta \in \mathbb{R}$, its true that $\theta x_1 + (1 - \theta) x_2 \in \mathcal{C}$. An affine combination, $\theta_1 x_1 + \dots + \theta_k x_k$, with $\theta_1 + \dots + \theta_k$ lies in \mathcal{C} too. *Convex sets* are in a way extension of affine sets where θ is restricted between 0 and 1 along with $\sum \theta_i = 1$. The set $\mathcal{C} \subseteq \mathbb{R}^n$ is convex for any $x_1, x_2 \in \mathcal{C}$ and $0 \leq \theta \leq 1$ such that $\theta x_1 + (1 - \theta) x_2 \in \mathcal{C}$. "If every point in the set can be seen by every other point in the set, along an unobstructed straight path, its a convex set" (Boyd and Vandenberghe 2010). Figure 7.2 represents geometric examples of convex and non-convex sets. A convex combination can therefore be represented as

$$\theta_1 x_1 + \dots + \theta_k x_k \in \mathcal{C}, \quad x_i \in \mathcal{C}, \quad \theta_i \geq 0, \quad \sum \theta_i = 1, \quad i = 1, \dots, k \quad (7.6)$$

A special kind of convex set is the convex cone, which is used in the formulation of *second order conic programming* which is a method to treat convex optimisation problems. The set \mathcal{C} is a convex cone if for any $x_1, x_2 \in \mathcal{C}$ and $\theta_1, \theta_2 \geq 0$, we have

$$\theta_1 x_1 + \theta_2 x_2 \in \mathcal{C} \quad (7.7)$$

Geometrically the above equation represents a 2D slice of pie, with its apex at 0 and its edges passing through x_1 and x_2 . Figure 7.3 represents this convex cone on the left and also shows an example of a cone that is non-convex on the right since the line passing through x_1 and x_2 does not lie within the set. With this the second-order cone or the *Euclidean*¹ norm cone in can be represented as

$$\begin{aligned} \mathcal{C} &= \{(x, t) \mid \|x\|_2 \leq t\} \subseteq \mathbb{R}^{n+1} \\ &= \left\{ \begin{pmatrix} x \\ t \end{pmatrix} \middle| \begin{pmatrix} x \\ t \end{pmatrix}^T \begin{bmatrix} I_{n \times n} & 0 \\ 0 & -1 \end{bmatrix} \begin{pmatrix} x \\ t \end{pmatrix} \leq 0, \quad t \geq 0 \right\} \end{aligned} \quad (7.8)$$

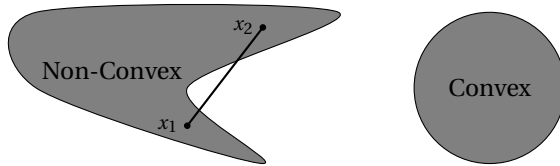


Figure 7.2: Convex and non-convex set examples.

¹Euclidean norm is the second norm given by $\|x_1 - x_2\|_2 = \sqrt{(x_1 - x_2)^T (x_1 - x_2)}$

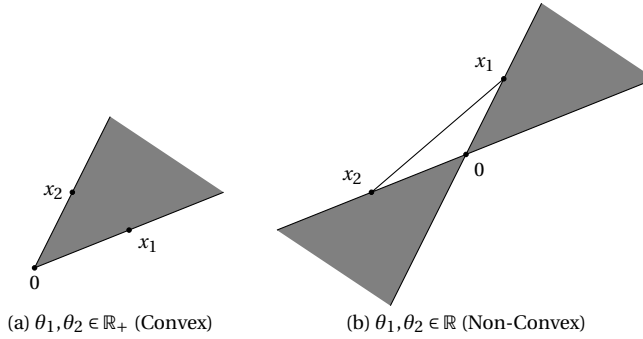


Figure 7.3: Convex and non-convex cone examples.

The second-order cone in \mathbb{R}^3 is also known as *quadratic cone* or *Lorentz cone* or *ice-cream cone* and can be represented as $\mathcal{C} = \{(x_1, x_2, t) \mid \|x_i\|_2 \leq t, i = 1, 2\} \subseteq \mathbb{R}^3$ and is shown in the Figure 7.4.

To formulate an optimisation problem as a convex one, all the functions in the problem must be convex. Problems like the descent guidance do not have convex constraints due to the lower bound on the thrust and also the dynamics governing the motion of the SC is non-linear. Hence it is necessary to be able to convert these to convex functions to be able to solve the problem as a convex optimisation problem. A function, $f: \mathbb{R}^n \rightarrow \mathbb{R}$ is said to be convex if it satisfies the following three conditions:

- (i) $\text{dom } f$ is a convex set
- (ii) All $x, y \in \text{dom } f$
- (iii) $0 \leq \theta \leq 1$

This leads to the inequality $f(+ (1 - \theta)y) \leq \theta f(x) + (1 - \theta)f(y)$ to hold true. Figure 7.5a shows the geometric interpretation of this inequality. As can be seen that for a function to be convex, the line joining any two points of the function in the set must lie above the graph of the function of all the points. Since it cannot be intuitively said if a function is convex or not by simply looking at the inequality function, the way to recognize the function's convexity is that it must fulfill the first and second order necessary conditions.

First Order: If f is differentiable, then f is convex iff $\text{dom } f$ is convex and

$$f(x) \geq f(x_0) + \nabla f(x_0)^T(x - x_0), \quad \forall x, y \in \text{dom } f \quad (7.9)$$

Second Order: If f is twice differentiable, then f is convex iff $\text{dom } f$ is convex and $\nabla^2 f$ is positive semidefinite for all $x \in \text{dom } f$

$$\nabla^2 f \succeq 0 \quad (7.10)$$

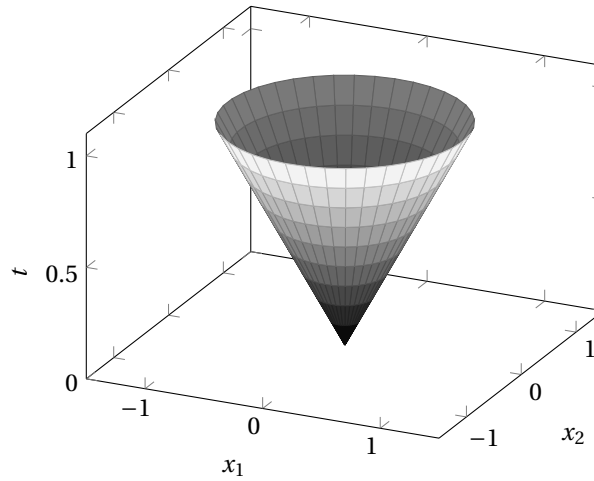
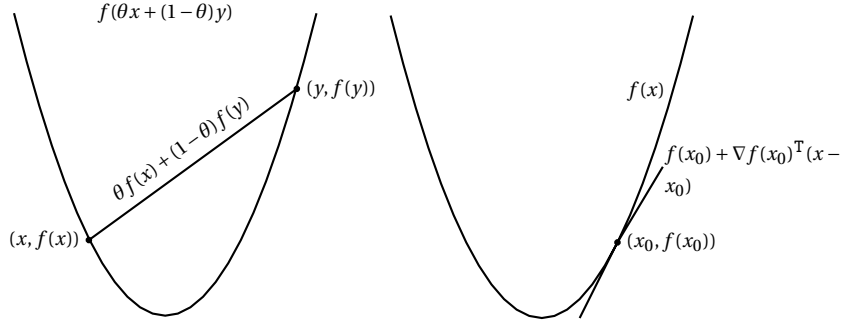


Figure 7.4: Second order cone boundary. It represents a filled cone.



(a) The line joining the two points will always lie above the graph
(b) First order condition for convex functions

Figure 7.5: Graphical representation and properties of a convex function.

As can be seen the right hand side of the first order condition is a Taylor approximation of the function $f(x)$ and the inequality makes it a global underestimator of the function if its convex i.e. the line shown in Figure 7.5b always lies below the graph if the function is convex. This enables deriving global information from local information making it the most important property of convex functions and resulting in beneficial properties in convex optimisation problems Boyd and Vandenberghe 2010. The second order condition is nothing but that the Hessian must be positive semidefinite i.e. the derivative must be non-decreasing and the function of x should have an upward curvature.

These conditions hold for differentiable functions but non differentiable convex functions exist, eg. $f(x) = |x|$. As can be interpreted at $x = 0$, there is a kink in the graph and is a non differential at the point, but it is a convex function. hence the above conditions are not a general requirement for a function to be convex but are a check for differentiable functions.

7.1.2. Convex optimisation Problems: Second-Order Cone Programming

Convex optimisation problems possess certain properties that enable efficient solving of the problem with robust solutions. The major difficulty is the recognition and formulation of the convex problem. Once the two are achieved, solving the problem is almost as similar as least squares or linear programming. Here we will discuss SOCP in detail, since it is the form used for the descent guidance. We put forth the form of *Convex optimisation problems* (Boyd and Vandenberghe 2010)

$$\begin{aligned} & \text{minimise} && f_0(x) \\ & \text{subject to} && g_i(x) \leq 0, \quad i = 1, \dots, m. \\ & && a_j^T x = b_j, \quad j = 1, \dots, p. \end{aligned} \tag{7.11}$$

In comparison with the general optimisation problem, the convex optimisation problem has the following three requirements,

- (i) The objective function f_0 has to be a *convex* function; and
- (ii) The inequality constraints g_1, \dots, g_m have to be *convex*; and
- (iii) The equality constraints $a_j^T x - b_j$ or h_1, \dots, h_p must be *affine*.

The advantage of the constraints being convex is the feasible set of the problem from the intersection of all the constraints is also convex. This is because of the property that intersection of convex sets is convex (Boyd and Vandenberghe 2010).

$$\mathcal{D} = \bigcap_{i=0}^m \text{dom } g_i \tag{7.12}$$

For the problem to be categorised as a SOCP, the following requirements must be met,

- (i) The objective function f_0 has to be a *affine* function; and

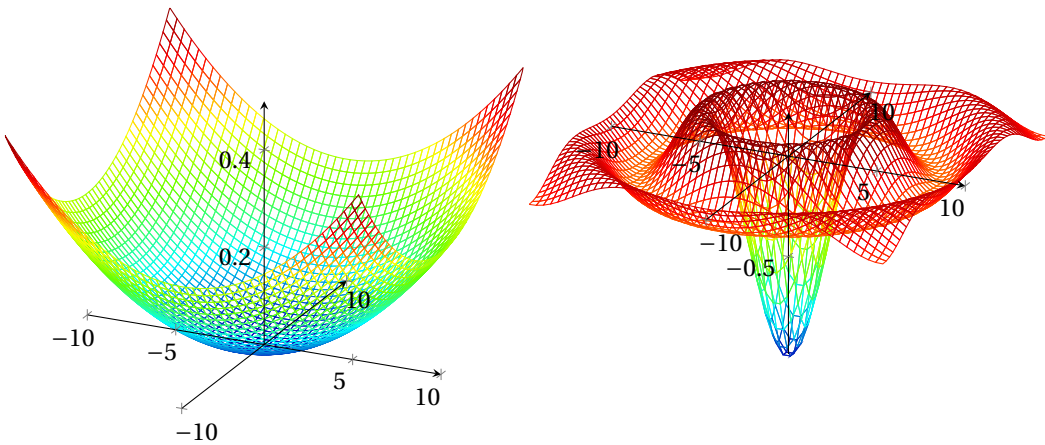


Figure 7.6: Optimal solutions of convex and non-convex problems

(ii) The inequality constraints g_1, \dots, g_m have to be *convex cones*; and

(iii) The equality constraints $a_j^T x - b_j$ or h_1, \dots, h_p must be *affine*.

The form of the convex problem is updated to SOCP as:

$$\begin{aligned} & \text{minimise} && f^T x \\ & \text{subject to} && \|A_i(x) + b_i\| \leq c_i^T x + d_i, \quad i = 1, \dots, m. \\ & && Fx = g \end{aligned} \tag{7.13}$$

where $A \in \mathbb{R}^{k \times n}$ and $F \in \mathbb{R}^{n+1}$. Comparing with Eq. 8.8 it can be seen that the inequality constraints represent a second-order cone.

$$\mathcal{C} = \{(A_i x + b_i, c_i^T x + d_i) \mid \|A_i x + b_i\| \leq c_i^T x + d_i, i + 1, \dots, m\} \subseteq \mathbb{R}^{k+1} \tag{7.14}$$

The obvious reason for using convex optimisation is the necessary existence of *only one global minimum* for convex function over its domain. The probability of getting stuck at a local minimum is therefore nil. Also the negative gradient of the function will always lead to the optimum. A parabola is used to represent a convex function in Figure 7.6a since it is easy to visualize but it does not generalise convexity. In reality convex sets are not intuitive or easy to visualize.

As mentioned earlier the difficult part is the problem formulation in the SOCP form. SOCP possesses remarkable properties which enable speedy solving of the problem. These solvers are on the verge of being a mature technology. At the end of this chapter the descent guidance will be formulated as an SOCP.

The next sections are towards understanding the steps how a nonconvex, nonlinear problem can be reformulated to a convex one without compromising on the constraints or objective function. The convex guidance developed by Açıkmeşe and Ploen 2007 called *lossless convexification* will be briefly discussed to give an overview of the existing methods. Then we will move on to *successive convexification* which has been developed and used in a few recent works (Mao, Szmuk, and Açıkmeşe 2016), (Szmuk, Utku, and Açıkmeşe 2017), (Szmuk and Açıkmeşe 2018), (Açıkmeşe, Carson, and Blackmore 2013) and (Xinfu and Ping 2014).

7.2. Lossless Convexification

Referring back to Problem 2b on page—, it can be seen that the source of nonlinearity comes from the dynamics due to nonlinear gravitational acceleration of the target body and nonconvexity from the control constraint. The method of lossless convexification by Açıkmeşe and Ploen 2007 provides a way to mathematically manipulate nonconvex functions to a second order cone form, thereby making it convex and enabling the computation of the global minimum to a given accuracy with a deterministic upper bound on the number of iterations for convergence. We discuss each step of the procedure in the section and reformulate the nonconvex constraints to a convex form.

7.2.1. Introduction of Slack Variables

The control constraint dealing with the thrust magnitude given in the optimisation problem is the primary nonconvex constraint in the problem. Once the thrusters have been initiated, they cannot be turned off during the maneuver and also there is a minimum level of thrust at which the propulsion system can operate. Below this level the operation is unreliable and hence the thrust magnitude needs to be bounded at the lower end too.

$$0 < T_{min} \leq \|T(t)\| \leq T_{max} \quad (7.15)$$

The lower bound defines the nonconvex feasible control space.² This can be proved geometrically by considering a two dimensional thrust as follows.³

$$\sup\{\|T\| \mid T_z = 0, \|T(t)\| \leq T_{max}\} = \{\|T\| \mid \sqrt{T_x^2 + T_y^2} = T_{max}\} \quad (7.16)$$

$$\inf\{\|T\| \mid T_z = 0, 0 < T_{min} \leq \|T(t)\|\} = \{\|T\| \mid \sqrt{T_x^2 + T_y^2} = T_{min}\} \quad (7.17)$$

$$(7.18)$$

Considering T_{max} and T_{min} , the constraint is geometrically shown in Figure 7.7 as an annular diagram. Repeating the definition of a convex function, it states that a line drawn between two points in the convex set must also lie in the set. As can be seen that the lines passing through the central region of the annulus to connect two points do not lie inside the convex set themselves hence proving the nonconvexity of the function.

Lossless convexification is a simple but effective way of manipulating the nonconvex function to make it convex. A scalar slack variable is introduced to relax the control constraint such that the control space becomes *affine* which makes it inherently convex (Açıkmeşe, Carson, and Blackmore 2013). For the thrust control constraint, its magnitude is replaced by the scalar variable, Γ and the variable itself is constrained by the thrust magnitude.

$$0 < T_{min} \leq \Gamma \leq T_{max} \quad (7.19)$$

$$\|T(t)\| \leq \Gamma \quad (7.20)$$

The thrust magnitude has been relaxed by Γ without a lower bound on it, which means that $\|T(t)\| \leq T_{min}$ is feasible in the new problem, but not in the original problem, with the bounded thrust magnitude. The original control space is therefore a subset of the relaxed control space, represented as below

$$\{T \mid 0 \leq T_{min} \leq \|T(t)\| \leq T_{max}\} \subset \{T, \Gamma \mid 0 < T_{min} \leq \Gamma \leq T_{max}\} \quad (7.21)$$

However, Açıkmese and Ploen 2007 have proved that an optimal solution to the new problem with relaxed constraints will satisfy the original thrust constraints as well. The proof is quite long and hence will not be presented in this thesis and the interested reader can refer to Açıkmese and Ploen 2007 for the same. The central conclusion from the proof is that the optimal control history for both Γ and $\|T\|$ is same as shown below which also requires $\|T^*\|$ to satisfy the Eq. 7.19.

$$\Gamma^*(t) = \|T^*(t)\| \quad (7.22)$$

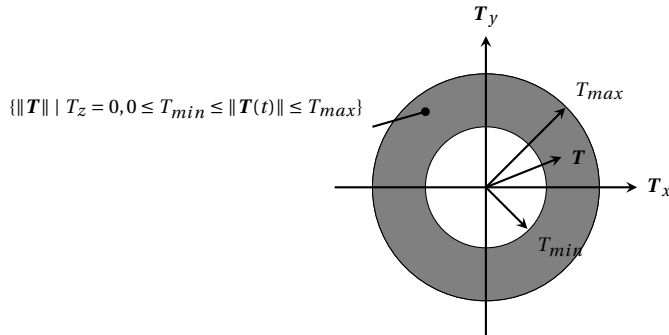


Figure 7.7: Optimal solutions of convex and non-convex problems

²An upper bounded constraint, $0 \leq \|T_B(t)\| \leq T_{max}$ would be convex. Visualizing Figure ??, with just an upper bound, the set would be a closed circle which is convex.

³For $T_z \neq 0$, the region could be imagined as a partially hollow sphere.

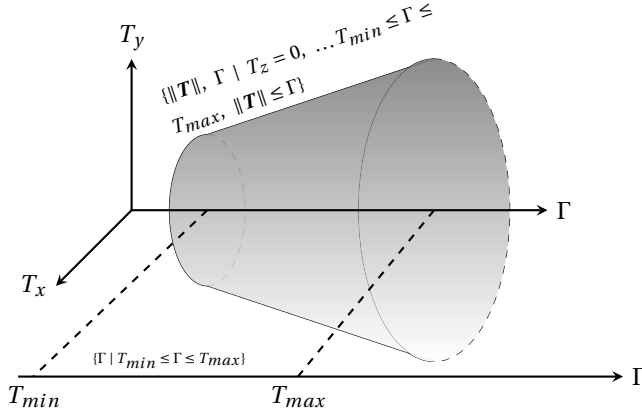


Figure 7.8: Second order cone boundary. It represents a filled cone.

Figure 7.8 represents the visualisation of the relaxed control space for understanding the convexity of the new constraints. The combination of both the relaxed constraints leads to a truncated cone as the control space, which is convex by nature. The affine control space representation shown on the axis Γ is represented similarly in the combined figure. The binding values T_{min} and T_{max} form the end caps of the truncated cone at their locations on the Γ axis parallel to the plane of the torque axes.

In Subsection 7.1.2 the require form for a constraint has been put forth in Eq. 7.13. To take advantage of the beneficial properties of SOCPs, the new constraints need to be in the same form. Therefore any other constraints that might be needed for the powered descent guidance will be added to the problem in later stages in this form. For now, the newly formulated convex problem is as shown in Problem 2c.

► PROBLEM 2c: Convexified Control Constraints

$$\text{minimise } -m(t_f)$$

subject to:

Kinematics:

$$\dot{\mathbf{r}}^I(t) = \mathbf{v}_{B/I}^I(t), \quad \dot{\mathbf{q}}_{B/I}(t) = \frac{1}{2}\boldsymbol{\omega}_{B/I}^B(t) \otimes \mathbf{q}_{B/I}(t)$$

Dynamics:

$$\begin{aligned} \dot{m}(t) &= -\alpha\Gamma(t), & \dot{\mathbf{v}}_{B/I}^I(t) &= \frac{\mathbf{T}^I(t)}{m(t)} + \mathbf{g}_I \\ \dot{\boldsymbol{\omega}}_{B/I}^B(t) &= J^{-1}(\mathbf{r}_B(t) \times \mathbf{T}^B(t) - \boldsymbol{\omega}_{B/I}^B(t) \times J\boldsymbol{\omega}_{B/I}^B(t)) \end{aligned}$$

Control Constraints:

$$0 < T_{min} \leq \Gamma \leq T_{max}$$

$$\|\mathbf{T}^I(t)\| \leq \Gamma$$

Boundary Conditions:

$$\begin{aligned} m(0) &= m_{wet} \\ \mathbf{r}^I(0) &= \mathbf{r}_0^I, \quad \mathbf{r}^I(t_f) = \mathbf{r}_f^I, \quad \mathbf{v}_{B/I}^I(0) = \mathbf{v}_{B/I_0}^I, \quad \mathbf{v}_{B/I}^I(t_f) = \mathbf{v}_{B/I_f}^I \\ \mathbf{q}_{B/I}(0) &= \mathbf{q}_{B/I_0}, \quad \mathbf{q}_{B/I}(t_f) = \mathbf{q}_{B/I_f}, \quad \boldsymbol{\omega}_{B/I}^B(0) = \boldsymbol{\omega}_{B/I_0}^B, \quad \boldsymbol{\omega}_{B/I}^B(t_f) = \boldsymbol{\omega}_{B/I_f}^B \end{aligned}$$

Additional Constraints:

$$\|A_i(\mathbf{x}) + b_i\| \leq c_i^T \mathbf{x} + d_i, \quad i = 1, \dots, m$$

7.2.2. Change of Variables

The Problem 2c has convexified control and additional constraints but is still not fit for convex solvers due to the nonlinearity in the dynamics. The nonlinearity in the mass flow dynamics will be dealt by the change of variables. The control variables $\mathbf{T}(t)$ and $\Gamma(t)$ will be changed to establish linear second order differential equation that can ultimately represent a linear, time-invariant, state-space system (LTI). The control variables

are transformed to accelerations from thrust forces as below,

$$\sigma(t) \triangleq \frac{\Gamma(t)}{m(t)}, \quad \tau(t) \triangleq \frac{\mathbf{T}(t)}{m(t)} \quad (7.23)$$

It is important to mention here, that this change of variables maintains the equivalence in the optimal controls as it was for $\mathbf{T}(t)$ and $\Gamma(t)$ i.e. $\|\tau^*(t)\| = \sigma^*(t)$. Using the new variables $\sigma(t)$ and $\tau(t)$ the EOMs for translational motion and mass flow can be rephrased as:

$$\mathbf{v}(t) = \tau(t) + \mathbf{g} \quad (7.24)$$

$$\frac{\dot{m}(t)}{m(t)} = -\alpha\sigma(t) \quad (7.25)$$

As can be seen the EOMs are still not linearised due to the nonlinear gravity field in Eq. 7.24 and the time dependent mass term in Eq. 7.25. Further steps need to be taken in order to linearise them as well as the other nonlinear and dynamics constraints. The cost function and the control constraints need to be changed with these variables. Eq. 7.25 is a first order, ordinary differential equation (ODE). This ODE can be solved as (Boyce and DiPrima 2008):

$$m(t) = m_0 \exp\left(-\alpha \int_0^{t_f} \sigma(t) dt\right) \quad (7.26)$$

From the above equation, it can be seen that minimizing the exponential function would maximise $m(t)$. Hence the cost function is reformulated to a new but valid cost function as shown below.

$$\text{minimise } -m(t_f) = \text{minimise} \int_0^{t_f} \sigma(t) dt \quad (7.27)$$

The control constraints with the new variables are given as

$$\|\tau(t)\| \leq \sigma(t) \quad (7.28)$$

$$\frac{T_{min}}{m(t)} \leq \sigma(t) \leq \frac{T_{max}}{m(t)} \quad \forall t \in [0, t_f] \quad (7.29)$$

But as can be seen the second constraint is again a source of nonlinearity due to the time dependent mass.

This nonconvexity can be removed by another change of variables, given as

$$z(t) \triangleq \ln m(t) \quad (7.30)$$

The ODE for mass flow in Eq. 7.26 is changed to

$$\dot{z}(t) = -\alpha\sigma(t) \quad (7.31)$$

The inequality control constraint is therefore now rewritten as

$$T_{min} e^{-z(t)} \leq \sigma(t) \leq T_{max} e^{-z(t)} \quad (7.32)$$

This constraint is still not convexified as can be understood from the similar graph of the function $1/z$ and also the exponential cannot be a part of the SOCP constraint. In order to take care of this a Taylor series approximation is used for the the exponential function as below (Boyce).

$$f(z) = \sum_{n=0}^{\infty} \frac{f^{(n)} z_0}{n!} (z - z_0)^n \quad (7.33)$$

where, z_0 and n denote the nominal around which the series is to be extended and the n^{th} order derivative respectively. Considering upto the 2nd order derivative would suffice since it provides enough precision and also it would keep the lower bound thrust convex, which is the purpose of the variable changes. The lower bound on the thrust can be represented as

$$T_{min} e^{-z_1(t)} [1 - (z(t) - z_1(t)) + \frac{1}{2} (z(t) - z_1(t))^2] \leq \sigma(t) \quad (7.34)$$

where, z_1 is the nominal point. For the upper bound on the thrust as discussed above, anything above the first order would maintain nonconvexity and therefore we just the first order Taylor expansion will be used

$$\sigma(t) \leq T_{max} e^{-z_2(t)} [1 - (z(t) - z_2(t))] \quad (7.35)$$

where, z_2 is the nominal point. The pre-factors multiplied to the expansion series can be abbreviated as

$$\mu_1(t) = T_{min} e^{-z_1(t)}, \quad \mu_2(t) = T_{max} e^{-z_2(t)} \quad (7.36)$$

It is important that the mass equivalent variables z_1 and z_2 or the nominal points are logical to ensure sufficient accuracy of the newly defined constraints. This can be done by reiterating the definition of z and setting the slack variable Γ to the lower and upper thrust values for the lower and upper bounds respectively.

$$z_1(t) = \ln m(t) = \ln(m_0 - \alpha T_{min} t) \quad (7.37)$$

$$z_2(t) = \ln m(t) = \ln(m_0 - \alpha T_{max} t) \quad (7.38)$$

An additional constraint needs to be put on z such that the physical bounds on it remain intact.

$$z_1(t) \leq z(t) \leq z_2(t) \quad (7.39)$$

Using all the newly defined constraints the SOCP can be set up for the next phase where we need to convexify the remaining nonlinear dynamics. Also using the equations for relative frame kinematics and dynamics we can update the convexified problem in 2c.

► PROBLEM 2d: Problem Formulation in the Relative Frame

$$\text{minimise } \int_0^{t_f} \sigma(t) dt$$

subject to:

Kinematics:

$$\dot{\mathbf{r}}^A(t) = \mathbf{v}_{B/A}^A(t), \quad \dot{\mathbf{q}}_{B/A}(t) = \frac{1}{2} \boldsymbol{\omega}_{B/A}^B(t) \otimes \mathbf{q}_{B/A}(t)$$

Dynamics:

$$\dot{z}(t) = -\alpha \sigma(t)$$

$$\dot{\mathbf{v}}_{B/A}^A(t) = \boldsymbol{\tau}^A(t) + \mathbf{g}^A - 2\boldsymbol{\omega}_{A/I}^A(t) \times \mathbf{v}_{B/A}^A(t) - \boldsymbol{\omega}_{A/I}^A(t) \times \boldsymbol{\omega}_{A/I}^A(t) \times \mathbf{r}^A(t)$$

$$\dot{\boldsymbol{\omega}}_{B/A}^B(t) = \mathbf{J}^{-1}(\mathbf{T}^B(t) - \boldsymbol{\omega}_{B/A}^B(t) \times \mathbf{J}\boldsymbol{\omega}_{B/A}^B(t) - \boldsymbol{\omega}_{A/I}^B(t) \times \mathbf{J}\boldsymbol{\omega}_{A/I}^B(t) - \boldsymbol{\omega}_{A/I}^B(t) \times \boldsymbol{\omega}_{B/A}^B(t))$$

Control Constraints:

$$\|\boldsymbol{\tau}^A(t)\| \leq \sigma(t)$$

$$\mu_1(t)\{1 - [z(t) - z_1(t)] + \frac{1}{2}[z_1(t) - z_2(t)]^2\} \leq \sigma(t) \leq \mu_2(t)\{1 - [z(t) - z_2(t)]\}$$

$$z_1(t) \leq z(t) \leq z_2(t)$$

Boundary Conditions:

$$m(0) = m_{wet}, \quad \mathbf{q}_{A/I}(0) = \mathbf{q}_{A/I_0}$$

$$\mathbf{r}^A(0) = \mathbf{r}_0^A, \quad \mathbf{r}^A(t_f) = \mathbf{r}_f^A, \quad \mathbf{v}_{B/A}^A(0) = \mathbf{v}_{B/A_0}^A, \quad \mathbf{v}_{B/A}^A(t_f) = \mathbf{v}_{B/A_f}^A$$

$$\mathbf{q}_{B/A}(0) = \mathbf{q}_{B/A_0}, \quad \mathbf{q}_{B/A}(t_f) = \mathbf{q}_{B/A_f}, \quad \boldsymbol{\omega}_{B/A}^B(0) = \boldsymbol{\omega}_{B/A_0}^B, \quad \boldsymbol{\omega}_{B/A}^B(t_f) = \boldsymbol{\omega}_{B/A_f}^B$$

Additional Constraints:

$$\|A_i(\mathbf{x}) + b_i\| \leq c_i^T \mathbf{x} + d_i, \quad i = 1, \dots, m$$

7.3. Dual Quaternion Problem Formulation

Before we can move to the next section of dealing with non linearities in the dynamics, we need to reformulate the problem in the format of DQs. We will deal with the kinematics and dynamics step by step along with the control constraints and boundary conditions to establish the problem in DQs. In the next section of successive convexification we will take care of the non linear kinematics and dynamics in the DQ form.

As can be seen the problem in 2d is in the inertial frame and this is appealing due to the simpler EOMs. However this leads to the final time boundary conditions being dependent on time due to the rotation of the target body about itself. This could render the problem intractable. Also additional constraints of the extended guidance problem (to be discussed in Section 8.6) are defined with respect to the landing site and are convex by nature. If they are to be redefined in the inertial frame, non-convexities will occur in these constraints. To avoid these problems we define the whole problem in the asteroid rotating reference frame. This retains the convexifications done so far and maintains the convex nature of the additional constraints to be added later on. It also has constant initial and final boundary conditions retaining the tractability of the problem. The problem in asteroid rotating frame, A is given as,

► PROBLEM 2e: Problem Formulation using Dual Quaternions

$$\text{minimise } \int_0^{t_f} \sigma(t) dt$$

subject to:

Kinematics:

$$\dot{\tilde{q}}_{B/A} = \frac{1}{2} \tilde{\omega}_{B/A}^B \tilde{\otimes} \tilde{q}_{B/A}$$

Dynamics:

$$\dot{z}(t) = -\alpha \sigma(t)$$

$$\dot{\tilde{\omega}}_{B/A}^B = \check{J}^{-1}(\check{F}^B - (\check{\omega}_{B/A}^B + \check{\omega}_{A/I}^B) \check{\times} \check{J}(\check{\omega}_{B/A}^B + \check{\omega}_{A/I}^B) - \check{J}\check{\omega}_{A/I}^B \check{\times} \check{\omega}_{B/A}^B - \check{\omega}_{A/I}^B \check{\times} \check{\omega}_{A/I}^B \check{\times} A)$$

Control Constraints:

$$\|\tau^A(t)\| \leq \sigma(t)$$

$$\mu_1(t)\{1 - [z(t) - z_1(t)] + \frac{1}{2}[z_1(t) - z_2(t)]^2\} \leq \sigma(t) \leq \mu_2(t)\{1 - [z(t) - z_2(t)]\}$$

$$z_1(t) \leq z(t) \leq z_2(t)$$

Boundary Conditions:

$$m(0) = m_{wet}, \quad \omega_{A/I}^A = \text{constant}$$

$$\dot{\tilde{q}}_{B/A}(0) = \dot{\tilde{q}}_{B/A_0}, \quad \dot{\tilde{q}}_{B/A}(t_f) = \dot{\tilde{q}}_{B/A_0}, \quad \dot{\tilde{\omega}}_{B/A}^B(0) = \dot{\tilde{\omega}}_{B/A_0}^B, \quad \dot{\tilde{\omega}}_{B/A}^B(t_f) = \dot{\tilde{\omega}}_{B/A_f}^B$$

Additional Constraints:

$$\omega_{A/I}^B = C_{B/A} \omega_{A/I}^A$$

$$\|A_i(\mathbf{x}) + b_i\| \leq c_i^T \mathbf{x} + d_i, \quad i = 1, \dots, m$$

7.4. Successive Convexification

Until here the method of lossless convexification proves useful for convexifying the control constraint but it fails to convexify the remaining nonlinear kinematics and dynamics. Mao, Szmuk, and Acıkmeşe 2016 presented a novel method to deal with such nonlinear dynamics, *successive convexification*. The underlying logic is to linearise the non convexities in the dynamics and control constraints about the solution for that iteration, say k^{th} iteration. This leads to a convex sub-problem preferably in the SOCP format, which can be solved to full optimality resulting in a new solution for the $(k+1)^{th}$ iterate. This process is continued successively till convergence. A continuous time convergence analysis done by Mao, Szmuk, and Acıkmeşe 2016 guarantees convergence to the optimal solution of the original problem. The proof is too extensive to be explained in this thesis and can be referred to in Mao, Szmuk, and Acıkmeşe 2016. The procedure for successive convexification will be explained step by step through the sub sections below.

7.4.1. Linearisation

Problem 2b in Chapter 5 shows the presence of nonlinearities in the attitude kinematics, dynamics, translational dynamics, mass dynamics and thrust constraints. We deal with a non-linear polyhedron gravity field for asteroids which adds non linearity in the gravitational acceleration present in the translational dynamics and also a non linearity due to the perturbing acceleration. All of these need to be convexified so to be suitable for the SOCP problem formulation. For this we first redefine the state vectors discussed in Chapter 4 as

below and also define the control vector.

$$\dot{\mathbf{x}}_A(t) = \begin{pmatrix} m(t) \\ \check{\mathbf{q}}_{B/A}(t) \\ \check{\omega}_{B/A}(t) \\ \check{\mathbf{F}}^B(t) \\ \dot{\check{\mathbf{F}}}^B(t) \end{pmatrix}, \quad \dot{\mathbf{u}}_A(t) = \begin{pmatrix} \check{\mathbf{F}}^B(t) \end{pmatrix} \quad (7.40)$$

The inclusion of the dual force and its first derivative in the state vector whilst the second derivative of the dual force in the control vector separates the state and control vector. This separation is beneficial since it prevents high frequency jitters in control due to the nonlinear dependency of the state on the control. The presence of these high frequency jitters have been found in paper and their absence by separation has also been proved. Hence we will go ahead with the separated vectors.

The convexification of the equality constraint is done by linearising them using first order Taylor approximation. But this does not ensure the optimal solution of the problem with linearised constraints to be the one for the original problem as well. To recover this optimality they are successively linearised till convergence. The continuous time nonlinear dynamics is of the form,

$$\dot{\mathbf{x}}(t) = f(\mathbf{x}(t), \mathbf{u}(t), t) \quad a.e. \quad 0 \leq t \leq t_f \quad (7.41)$$

where, $\mathbf{x} : [0, t_f] \rightarrow \mathbb{R}^n$ represents the state trajectory, $\mathbf{u} : [0, t_f] \rightarrow \mathbb{R}^m$, the control inputs and $f : \mathbb{R}^n \times \mathbb{R}^m \times \mathbb{R} \rightarrow \mathbb{R}^n$, the control-state mapping function. The control-state function will be assumed to be Fréchet differentiable⁴ with respect to all arguments and the control input to be Lebesgue integrable i.e. \mathbf{u} is a measurable non negative decreasing function with a finite Lebesgue integral.⁵ The first order Taylor expansion of the dynamics can be given as

$$\begin{aligned} \dot{\mathbf{x}}(t) &= f(\bar{\mathbf{x}}_{i-1}(t), \bar{\mathbf{u}}_{i-1}(t), t) + \frac{\partial}{\partial x} f(\mathbf{x}_{i-1}(t), \mathbf{u}_{i-1}(t), t) (\mathbf{x}(t) - \bar{\mathbf{x}}_{i-1}(t)) + \dots \\ &\quad + \frac{\partial}{\partial u} f(\mathbf{x}_{i-1}(t), \mathbf{u}_{i-1}(t), t) (\mathbf{u}(t) - \bar{\mathbf{u}}_{i-1}(t)) \end{aligned} \quad (7.42)$$

The above equation can be abbreviated with the following substitutions,

$$\mathbf{A}(t) = \left. \frac{\partial}{\partial x} f(\mathbf{x}_{i-1}(t), \mathbf{u}_{i-1}(t), t) \right|_{\bar{\mathbf{x}}_{i-1}, \bar{\mathbf{u}}_{i-1}} \quad (7.43)$$

$$\mathbf{B}(t) = \left. \frac{\partial}{\partial u} f(\mathbf{x}_{i-1}(t), \mathbf{u}_{i-1}(t), t) \right|_{\bar{\mathbf{x}}_{i-1}, \bar{\mathbf{u}}_{i-1}} \quad (7.44)$$

$$\mathbf{z}(t) = f(\bar{\mathbf{x}}_{i-1}(t), \bar{\mathbf{u}}_{i-1}(t), t) - \mathbf{A}(t)\bar{\mathbf{x}}_{i-1}(t) - \mathbf{B}(t)\bar{\mathbf{u}}_{i-1}(t) \quad (7.45)$$

The linearised dynamics would therefore look like,

$$\dot{\mathbf{x}}(t) = \mathbf{A}(t)\mathbf{x}(t) + \mathbf{B}(t)\mathbf{u}(t) + \mathbf{z}(t) \quad (7.46)$$

The problem formulation as shown in Problem 2e, is as per lossless convexification and includes slack variables to convexify the nonconvex controls. However the nonconvexity in the dynamics still exists. We can linearise all the non convex constraints and dynamics in the successive convexification algorithm or we can include the slack variables for the convexified constraints. From the state vector and control vector in Eq. 7.40 we can state the dynamic state as shown in the next page.

The approach is to directly linearise the nonlinearities in the dynamic state at the initial and final time about $\bar{\mathbf{x}}(t)$

⁴A function f is Fréchet differentiable at a if $\lim_{x \rightarrow a} \frac{f(x) - f(a)}{x - a}$ exists.

⁵Lebesgue integral is by definition $\int_0^\infty u(t) dt$.

$$\begin{aligned}\dot{\check{x}}_A(t) &= \begin{pmatrix} \dot{m}(t) \\ \dot{\check{q}}_{B/A}(t) \\ \dot{\check{\omega}}_{B/A}^B(t) \\ \dot{\check{F}}^B(t) \\ \dot{\check{F}}^B(t) \end{pmatrix} \\ &= \begin{pmatrix} -\alpha \|F^B(t)\| \\ \frac{1}{2} \check{\omega}_{B/A}^B(t) \otimes \check{q}_{B/A}(t) \\ \check{J}^{-1}(\check{F}^B(t) - (\check{\omega}_{B/A}^B(t) + \check{\omega}_{A/I}^B(t)) \times \check{J}(\check{\omega}_{B/A}^B(t) + \check{\omega}_{A/I}^B(t)) - \check{J}\check{\omega}_{A/I}^B(t) \times \check{\omega}_{B/A}^B(t) - \check{\omega}_{A/I}^B(t) \times \check{\omega}_{A/I}^B(t) \times A(t)) \\ \check{F}^B(t) \\ \check{u}_A(t) \end{pmatrix} \quad (7.47)\end{aligned}$$

7.4.2. Virtual Control

Linearisation of the dynamics can lead to the introduction of infeasibility in the solution space even if the original nonlinear problem is feasible. This situation is called *artificial infeasibility*. This undesirable infeasibility prevents convergence as it obstructs the iteration process. Mao, Szmuk, and Acıkmeşe 2016 suggest the use of a *virtual control*, $v(t)$ that works as an addition to the actual control input to make the infeasible region infeasible. An unconstrained virtual control ensures that any state in the feasible region of the original problem is reachable in finite time when just the control input $u(t)$ is not enough to do so. The virtual control can be inferred as a an artificial or synthetic acceleration that acts on the SC, to steer it to any state in the feasible region. The linearised dynamics therefore becomes

$$\dot{d}(t) = A(t)d(t) + B(t)e(t) + D(t)v(t) + C(t) \quad (7.48)$$

where, $D(t)$ can be chosen based on $A(t)$ such that both of them ($A(.)$, $D(.)$) are controllable.

The virtual control is unconstrained, which means there is no restriction on its need, which needs to be taken care of to ensure that the control is still within the real bounds and can be achieved by the SC subject to the original nonlinear constraints. This is done by *penalising* the cost function with an additional term of the form

$$\gamma(.):=\text{ess sup}_{t\in[0,t_f]}\|.(t)\|_1 \quad (7.49)$$

where, $\|.\|_1$ is the first norm on \mathbb{R}^n given by $\|c(t)\|_1 = \sum_{i=1}^n |c_i(t)|$. The term used for penalising is Ev and hence the penalty function becomes,

$$\gamma(Ev):=\text{ess sup}_{t\in[0,t_f]}\|E(t)v(t)\|_1 \quad (7.50)$$

The new penalised cost function after linearising therefore becomes,

$$\text{minimise } -z(t_f) + w_v\gamma(Ev) \quad (7.51)$$

where, w_v is the penalty weight for the virtual control.

7.4.3. Trust Regions

Linearising nonlinear functions leads to the concern of another problem arising, which is that it might render the problem unbounded. When a large deviation is allowed to occur from the linearising point, the linear approximation may not be capable of capturing the nonlinearity. To understand this we take simple example problem,—.

Trust region as the name suggests, helps define the region within which the linear approximation can be trusted to capture the nonlinearity. This ensures that the linearised trajectory does not diverge from the nominal trajectory attained in the previous succession by a significant amount. The trust region needs to be co

$$\delta x(t)^T \delta x(t) + \delta u(t)^T \delta u(t) \leq \eta(t) \quad (7.52)$$

The new penalised cost function after linearising therefore becomes,

$$\text{minimise } -z(t_f) + w_v\gamma(Ev) + w_\eta\gamma(\eta) \quad (7.53)$$

where, w_η is the penalty weight for the trust region.

7.5. Extended Convex Guidance

The powered descent guidance algorithm can prove to be challenging because it usually treats the translational and rotational dynamics of the SC separately. This makes it difficult to deal with situations where both these dynamics need to be combined for some mission requirement. Certain constraints like the one on the line of sight of the SC require the SC to keep the target in sight while descent which make it dependent on both the orientation and position of the SC. In this section we will parameterise all such constraints that need to be met while the powered descent phase is in action. Finally in the problem formulation, these constraints will be converted to DQ format.

7.5.1. Need for Extended Constraints

We have the following requirements for the safety of the SC:

- The SC needs to avoid hazards like boulders or rough or highly sloped terrains near the landing site or those that may have not been observed during mapping.
- The SC needs to follow a trajectory such that no part of the SC comes in contact with the target surface before end of flight.
- The SC needs to maintain a certain altitude at the end of flight, so that just the sample collector hardware is in contact with the surface which also requires the enforcing of no subterranean flight to prevent any kind of damage to the hardware or SC.
- Also depending in the resolution of the mapping images, the landing site may need to be changed by HDA and retargeting to a nearby safe site is required. This can lead to drastic changes in the trajectory and there should be a constraint for robustness of the optimiser performance.

7.5.2. Glide-Slope Constraint

The guidance problem for the powered descent is a TPBVP, which means it finds an optimal trajectory from the initial state of the SC to a required final state or landing site. The control constraints discussed in the previous section take care of the feasibility of the trajectory from the point of view of the propulsion system. But we need to implement certain path constraints since this is a TAG descent.

In lieu with all the above requirements, the *glide-slope constraint* can be established, which enforces on the optimiser software a safe reachable space for the SC. The glide slope is nothing but a cone about the normal from the surface of the landing site with its vertex at the landing site location on the surface, which guides the trajectory of the SC to ensure no contact with the surface before the end of flight. In other words this means that the elevation angle of the SC with respect to the plane of the surface must always be greater than the glide-slope angle, θ . Geometrically this is represented in the Figure ?? and mathematically can be represented as

$$\mathbf{r}_{B/A}^A \cdot \mathbf{z}_A \geq \|\mathbf{r}_{B/A}^A\| \cos \phi \quad \forall t \in [t_0, t_f] \quad (7.54)$$

This takes care of the second and third requirements mentioned above. Now with the HDA system in the loop, retargetings might be required on the detection of hazards. One such trigger could be the presence of an unobserved boulder⁶ near the landing site. This can be taken care of by simply increasing the glide-slope angle by the amount required as shown in Figure ?? and resolving the optimisation problem. The same treatment is implemented for a surface with increasing slope close to the landing site.

$$\phi_h = \arctan \left(\frac{h + \delta h}{\sqrt{x_b^2 + y_b^2}} \right) \quad (7.55)$$

The inability of this constraint to safeguard the SC arises in situations where the HDA software detects one or more hazards at the landing site for example rocky terrain or an undetected crater (could be the rim or slope or pit). In this case a new trajectory to a nearby safe landing site needs to be solved for. This will be discussed in detail in Section 8.8, where we discuss the implementation of the logic of optimised landing on a new safe site.

⁶Mapping will detect the tall boulders, only boulders of small height need to be considered. Implementing the presence of tall boulders would make the safe glide slope angle too large and make the landing scenario infeasible.

Implementation

As discussed in the earlier sections the constraint needs to be converted to SOCP form

7.5.3. Attitude Constraints

The rotational manoeuvres of the SC need to be restricted depending on the requirement of the onboard instruments. For altitude measurements for example via RADAR the attitude of the SC should be within a certain angle with respect to the normal to the surface being observed for accurate measurements as well as within a certain angle with respect to the boresight of the RADAR or optical camera due to sensor hardware limitations. Now, the constraint for accurate measurements is an angle about the surface normal(ground fixed frame) whereas the LOS constraint is about the body fixed frame. The visual representation of both these constraints is shown in the Figure ??.

An important constraint on the attitude comes from safety of the SC which intends to prevent the upside-down flight of the SC at all times. But this will already be taken care of by the combination of LOS and accurate measurement constraints.

Implementation

7.5.4. Thrust Direction Constraint

Thrust pointing/direction constraint as the name suggests is the constraint in the body fixed frame for the direction of thrust from the propulsion system. The importance of this constraint is that it couples the feasibility of the physical trajectory to the SC hardware capabilities. In case of a rigidly fixed thruster system to the SC body, this constraint is the same as the attitude constraint since the direction of the commanded thrust will determine the attitude. For the mission scenario of TAG descent, a gimballed thruster would prove to be more beneficial. This is because the SC has a sample collector in the extended position whilst thrusting to successfully hover over the surface in the final phase of descent which would require the thruster to avoid disturbing the surface from where the sample needs to be collected.

If the SC is treated as a point mass and the net thrust is represented by a single thrust vector, then the net thrust on the SC could be pointed arbitrarily. With a rigid body SC, an arbitrary net thrust is not possible since the propulsion thruster cannot have any possible orientation with respect to the SC structure. The restrictions come from the SC design as well as the safety concern for onboard instruments. This can be translated to the thrust direction constraint where the net thrust vector would lie within a cone about the gimbal axis of the propulsion system.

Implementation

7.5.5. Polyhedral Gravity Field

7.6. Discretisation

7.7. Algorithm

8

Simulator Design and Verification

In this chapter we discuss the software simulator required to developed the guidance algorithms. It would represent the asteroid environment and the dynamics and kinematics of the SC motion around the asteroid. Since there is no hardware in the loop, the control actuator models will be simulated for control. The necessary instruments for attitude and position sensing have been modelled in the relative navigation developed in Razgus 2017 and will be utilized to close the loop of the GNC system. The top-level software architecture and lower levels have been discussed below along with their verification. We will validate the whole simulator with the help of data from the Rosetta mission using data kernels from SPICE.

8.1. Software Architecture

In this section, we present the top level architecture of the simulator required to verify and validate the developed GNC system. It gives an idea of the required data flow and closed-loop system and will be used to build detailed architectures of the subsystems in the thesis. Figure 8.1 shows the top level GNC simulator architecture to be achieved in Simulink with scripting in MATLAB.

The green blocks represent the inputs to the system, red blocks the GNC system and the blue blocks the outputs from the system. The blue lines indicate the inertial state and black lines the relative state. The individual components of the simulator are briefly described below:

Instrument Models: for the physical simulation of all the onboard sensors with two measurement outputs, inertial and relative.

Navigation: contains the navigational algorithms with quaternion and dual quaternion state estimator from Razgus 2017 and takes the measurement input and gives an output of the estimated inertial and relative state.

Guidance: contains the guidance algorithms for the different mission phases with their OCPs and constraints formulated with quaternions and dual quaternions.

Control: contains the control laws that minimize the guidance OCPs and provide the optimal controls and trajectories.

SC Dynamics and Model: contains the SC equations of motion in the quaternion and dual quaternion representation. The SC model contains details of the SC like its 3D model, mass, principal moments of inertia.

Asteroid Model and Environment: contains the gravity gradient model and the perturbation models due to 3rd body perturbation and the solar radiation pressure. It also contains the asteroid data like the mass of the asteroid, its mean density and rotation rate. The 3D polyhedron gravity model of the asteroid in the inertial frame and the landmark map are also included in this block.

Actuator Dynamics and Actuators: for the physical simulation of the actuators with the control input from the control block.

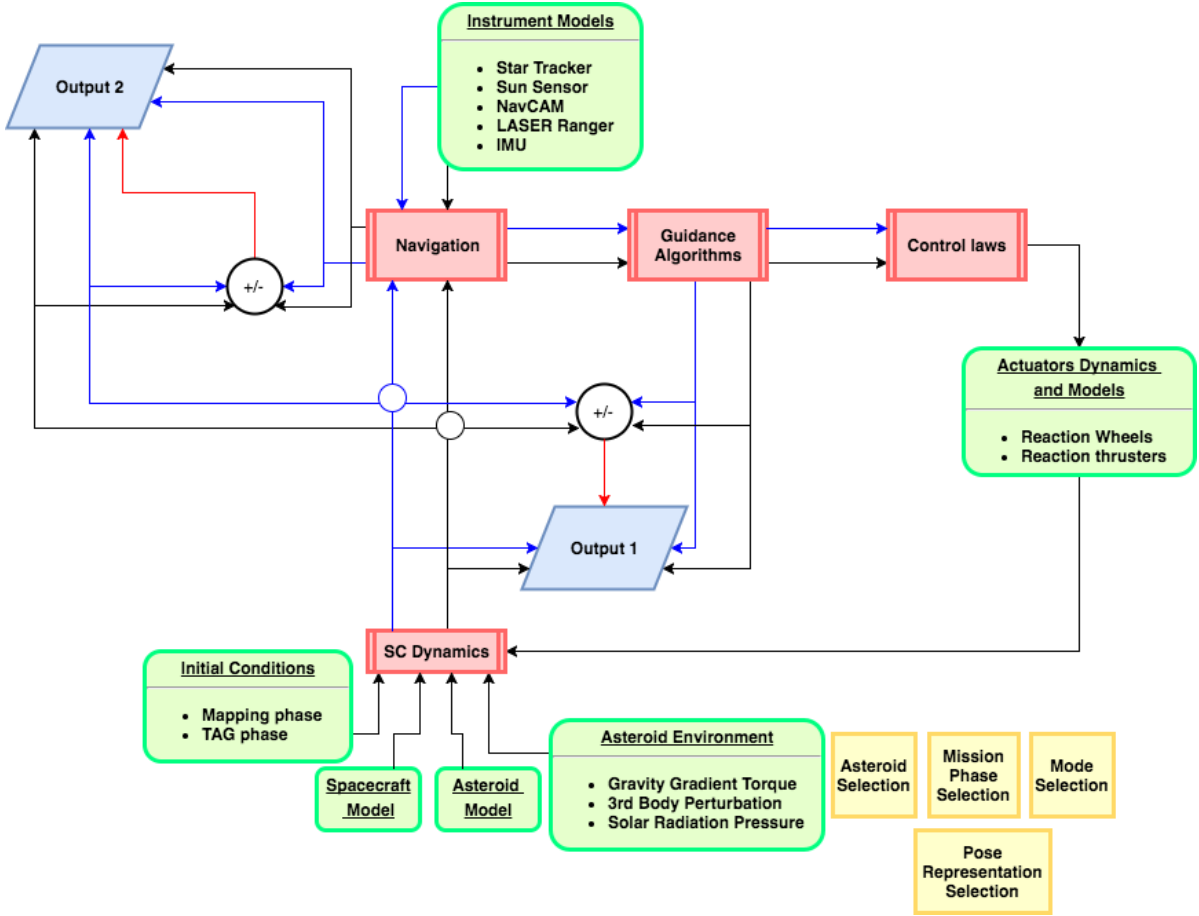


Figure 8.1: Top level Simulator Architecture

Initial Conditions: contains the data input for the initial and final pose of the SC for both its mission phases.

Switches: are required for the selection of particular sequences with specific sub-blocks. The Asteroid Selector switch selects the target asteroid, Mission phase selection selects whether it is the mapping or TAG phase, Mode Selection selects the SC mode and Pose Representation Selection selects whether the quaternion or dual quaternion simulator needs to run.

8.2. Spacecraft Model

In this section, the details for the SC model to be used in the simulator is detailed. The SC is based on Rosetta's dimensions since the mission was to Comet 67P which is at a distance of 3AU and hence it would satisfy for the power needs to similar distant missions. We discuss the dimensions in detail along with its mass and inertia properties and also its reflective properties.

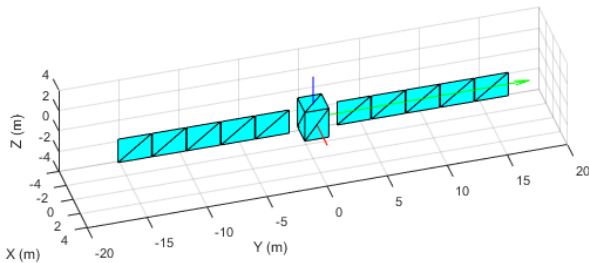


Figure 8.2: Simplified spacecraft model based on Rosetta's dimensions

8.2.1. Structure

The dimensions of Rosetta have been used as reference for the SC model for the simulator. The general structure of the SC is that of a cuboid of dimensions $2 \times 2.1 \times 2.8$ m at the centre with two solar arrays of dimensions $14 \times 0 \times 2.28$ m at about 1 m away from the cuboid along the X-axis. As mentioned the width of the solar arrays is considered negligible. they have an area of 32 sq.m each. The total wingspan of the solar arrays is about 32 m. Figure 8.2 shows the SC model.

Rosetta had bi-propellant (N_2O_4/MMH) thrusters and hence a divided cylindrical fuel tank at the centre of the SC. The upper section of the tank held the propellant whilst the heavier oxidiser was at the bottom section. The tank radius and height are 2.8 m and 1.197 m respectively. For simplicity we consider the orientation of the observation instruments and actuators to be fixed wrt the body. For the descent phase a reaction thruster generating a force in the positive Z-axis of the body reference frame is required and the reaction thrusters will be aligned to fire in the negative Z-axis of the body ref frame.

8.2.2. Mass Properties

The simulator is designed to treat the phases of close observation and descent. The mass properties of Rosetta at these stages is used as reference. At the start of the mission, Rosetta has a wet mass of 3000 kg and a dry mass of 1380 kg including the solar arrays and the Philae lander. The solar arrays weigh 75 kg each. At the comet rendezvous, approximately 776 m/s of Δv had been used. Initially the two-part cylindrical fuel tank contained 660 kg of propellant of density 880 kg/m³ and 1060 kg of oxidiser of density 1440 kg/m³.¹ Using Tsolkovski's equation the mass of the SC at 100 km altitude insertion can be found. Tsolkovski's equation is given as below:

$$m_0 = m_t e^{-\frac{\Delta v}{v_e}} \quad (8.1)$$

where m_t is the total initial mass of the SC, m_0 is the remaining total mass of SC after using Δv with a reaction thruster having an exhaust velocity of v_e . For Rosetta v_e was approximately 2200 m/s. Using the masses provided above, the mass of the SC after Δv usage of 776 m/s is ≈ 2108 kg. The usual propellant to oxidiser ratio for CH_4NH_3/MON is around 1.65 and using this we can find out their remaining masses to be ≈ 370 kg and 610 kg respectively. The inertia tensor of the SC can therefore be computed in three parts, the block, the solar arrays and the fuel tank. The inertia tensor of the SC is time variable due to the usage of propellant and oxidiser and therefore this change can be implemented by simply changing the inertia tensor by updating the propellant mass and dimensions as per the fuel usage requirements.

Block

$$\mathbf{I}_b = \begin{bmatrix} \frac{1}{12} m_b(y_b^2 + z_b^2) & 0 & 0 \\ 0 & \frac{1}{12} m_b(x_b^2 + z_b^2) & 0 \\ 0 & 0 & \frac{1}{12} m_b(x_b^2 + y_b^2) \end{bmatrix} = \begin{bmatrix} 966.9 & 0 & 0 \\ 0 & 1000.4 & 0 \\ 0 & 0 & 686.8 \end{bmatrix} \text{ kg m}^2 \quad (8.2)$$

Solar Arrays

$$\mathbf{I}_s = \begin{bmatrix} \frac{1}{12} m_s(y_s^2 + z_s^2) + m_s x_d^2 & 0 & 0 \\ 0 & \frac{1}{12} m_s(x_s^2 + z_s^2) & 0 \\ 0 & 0 & \frac{1}{12} m_s(x_s^2 + y_s^2) + m_s z_d^2 \end{bmatrix} = \begin{bmatrix} 7332.5 & 0 & 0 \\ 0 & 32.5 & 0 \\ 0 & 0 & 7300 \end{bmatrix} \text{ kg m}^2 \quad (8.3)$$

Bi-propellant Tank

$$\mathbf{I}_p = \begin{bmatrix} \frac{1}{12} m_p(h_p^2 + 3r^2) + m_p(\frac{h_p}{2})^2 & 0 & 0 \\ 0 & \frac{1}{12} m_p(h_p^2 + 3r^2) + m_p(\frac{h_p}{2})^2 & 0 \\ 0 & 0 & \frac{1}{2} m_p(h_p^2 + 3r^2) \end{bmatrix} \text{ kg m}^2 \quad (8.4)$$

$$\mathbf{I}_o = \begin{bmatrix} \frac{1}{12} m_o(h_o^2 + 3r^2) + m_o(h_t - \frac{h_o}{2})^2 & 0 & 0 \\ 0 & \frac{1}{12} m_o(h_o^2 + 3r^2) + m_o(h_t - \frac{h_o}{2})^2 & 0 \\ 0 & 0 & \frac{1}{2} m_o(h_o^2 + 3r^2) \end{bmatrix} \text{ kg m}^2$$

$$\mathbf{I}_t = \mathbf{I}_p + \mathbf{I}_o = \begin{bmatrix} 1006.8 & 0 & 0 \\ 0 & 1006.8 & 0 \\ 0 & 0 & 175.2 \end{bmatrix} \text{ kg m}^2 \quad (8.5)$$

¹<http://www.astronautix.com/n/n2o4mmh.html>

The inertia tensor is a sum of all the above and it comes to:

$$\mathbf{I}_{\text{total}} = \mathbf{I}_b + 2\mathbf{I}_s + \mathbf{I}_t \begin{bmatrix} 16639 & 0 & 0 \\ 0 & 2072.2 & 0 \\ 0 & 0 & 15462 \end{bmatrix} \text{ kg m}^2 \quad (8.6)$$

Inertia Update

The inertia tensor needs to be updated with the trajectory propagation depending on the fuel usage. A simple model will be used for this purpose. Since in reality as the propellant or oxidiser is consumed its level in the tank reduces whilst occupying the whole diameter of the tank, we will assume a change in the dimension of the tank by its height. Also since the treatment of fuel sloshing is out of scope for this thesis we consider the tank size to always be snug to the volume of available propellant or oxidiser at any instant.

Using Tsiolkovski's equation as given in Eq. 9.1 the mass can be updated with Δv usage. This can then be used to determine the new inertia of the SC. Due to the weak gravitational attraction of asteroids the Δv usage for observation and descent phases is within the range of a few km/s. We compute percentage change in inertia due to a range of Δv to decide if it is required to have inertia update every time step or if we can use constant inertia for each phase of the mission.

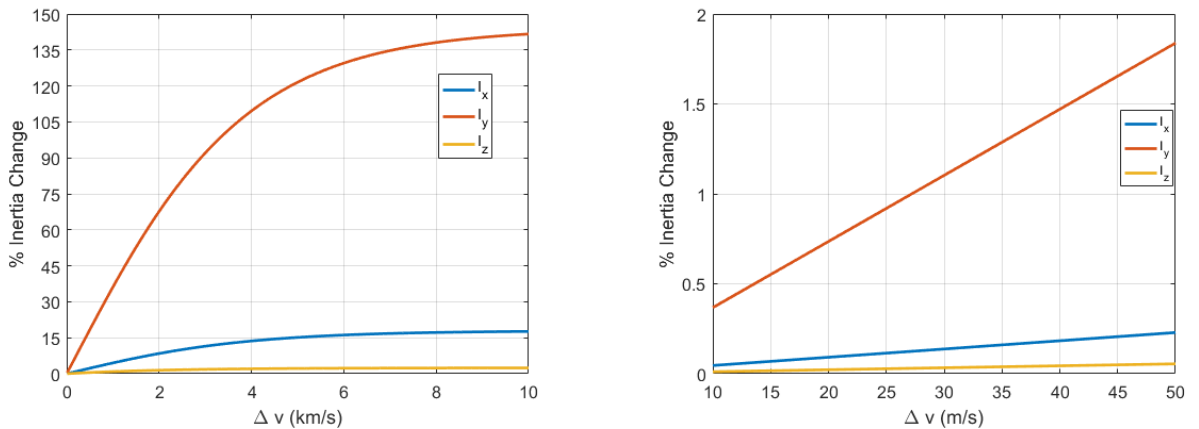


Figure 8.3: Percentage inertia change upto Δv 10 km/s (left) and 50 m/s (right)

8.2.3. Reflectivity

The reflectivity of the SC is a key factor to model the SRP acting on the SC as can be seen from the Eq. in Chapter 3. The SC is divided into two structures: the main body with twelve triangular facets and the solar arrays with ten triangular facets each on either side of the main body as can be seen in Fig 8.2. The solar panels are considered to have zero thickness. The SC therefore has a total of 32 facets which is representative enough to model the SRP. We compute the normals from each of these facets and their centroids to have their distances from the centre of mass of the SC in the body reference frame at all times.

Specular reflection is nothing but the regular reflection where each incident ray is reflected at the same angle to the surface normal as the incident ray but on the opposite side of the surface normal on the plane formed by the incident and reflected rays.² Diffuse reflection is the reflection of light or other waves or particles from a surface such that a ray incident on the surface is scattered at many angles rather than at just one angle as in the case of specular reflection.³ Montebrick and Gill 2008 give the value of reflectivity for solar panels $\alpha_r = 0.21$, thus the absorption is $1 - \alpha_r = 0.79$. The body is assumed to be more reflective, having $\alpha_r = 0.5$.

8.3. Asteroid Model

The asteroid model withholds information about the physical properties of the asteroid. As per our assumptions in Chapter 2, the SC should have a priori knowledge about the shape, mass, angular velocity, mean density, gravity and a landmark map of the asteroid of interest. As also discussed in the chapter, the three

²https://en.wikipedia.org/wiki/Specular_reflection, da-02/05/18

³https://en.wikipedia.org/wiki/Diffuse_reflection, da-02/05/18

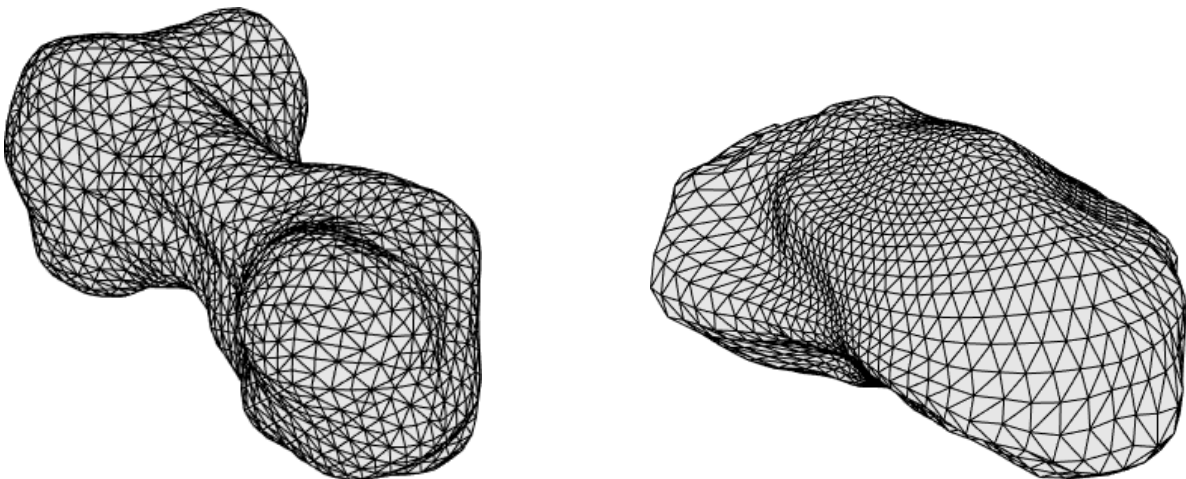


Figure 8.4: Polyhedron models of Kleopatra (left) and Itokawa (right) (not to scale)

small solar system bodies used for the thesis will be Kleopatra, Itokawa and Churyumov Geraseminko. Their properties have been listed in Table 2.1.

8.3.1. Polyhedron Model

A polyhedron model as the name suggests captures the shape of the body of interest by means of polyhedral shapes. In case of the surface structure of irregularly shaped celestial bodies these models consist of triangular facets meshed together. As can be intuitively guessed the smaller the size of these facets, a better resolution of the shape is obtained. But this also means higher number of the facets and this increases computational load as well as more memory storage capacity. The resolution also depends on whether the data is generated by ranging measurements from Earth or from flyby or close proximity missions to them.

The polyhedron.txt files for the selected asteroids for this thesis are already available from the Jet Propulsion Laboratory website.⁴ These files contain the vertices of the facets. The facets are indexed in a counter-clockwise fashion when observed from outside, making the computations of normals from them logical. Figure 8.4 gives the polyhedral surface structures of Kleopatra and Itokawa respectively. Higher resolution polyhedral models are also available but for the purpose of this thesis, these models will suffice.

8.3.2. Landmark Map

The purpose of the mission phase of mapping the asteroid surface as discussed in Chapter 6 is to generate a topographic map of the asteroid surface to help select sites of interest for the descent phase. These sites are selected based on surface features like craters, ridges, rocks or other visually recognizable features. The sampling based motion planning guidance is to find the optimum trajectory to observe the entire asteroid surface while finding a golden mean between the consumption of fuel and mission time. Since no actual SC trajectory maneuver takes place during the autonomous guidance searches for this trajectory we do not need the visual based navigation system to frequently measure the relative position of the SC. The SC just requires a generic landmark map to realize the surface of the asteroid it covers to analyse the computed trajectories and help it search for the optimal trajectory.

Taking real images and doing image processing once the trajectory is selected is not in the scope of this thesis. This is another reason for the requirement of an a priori landmark map. When the algorithm converges to the optimal trajectory and executes the same, it needs the landmark map to simulate the real time error from the navigation system and that computed by the guidance algorithm for autonomous corrections to safeguard the SC from failing to meet mission objectives due to process noise.

For the guidance subsystem we simply require the position of such landmarks with respect to the asteroid frame. Assuming perfect knowledge of the position and attitude of the SC with the help of the navigation subsystem, its ground-track on the surface of the asteroid can be generated. Utilizing a LIDAR model and the ground-track of the SC the surface observed on the asteroid can be modelled.

A number of different Hazard Detection and Avoidance (HDA) algorithms have been enlisted by **Svenja**

⁴<https://echo.jpl.nasa.gov/>, da-20/02/2018

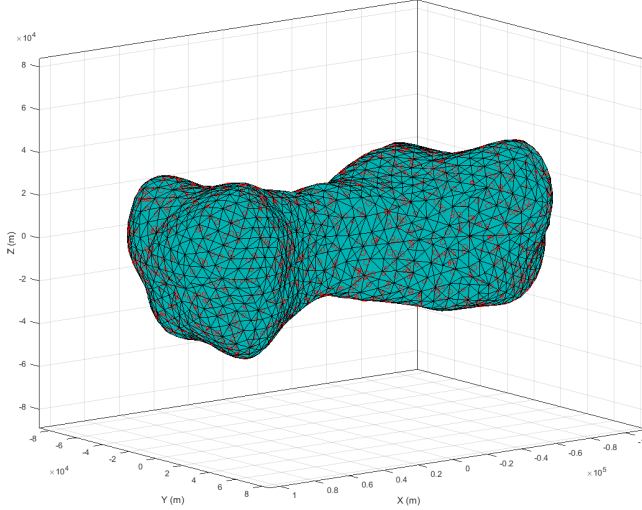


Figure 8.5: Pre-generated landmark map of Kleopatra

From this work it can be seen that recognizing surface features like craters has been developed with — accuracy. Resolving these features is possible either by means of a camera or LIDAR. Since using a LIDAR this resolution can be done from higher altitudes we choose a LIDAR for the mapping phase. For this we select use the specifications of OLA, the LIDAR used on board the current mission OSIRIS-Rex to the asteroid Bennu. From it can be seen that OLA is a state of the art LIDAR with the best specifications at present and hence we go ahead with the same. The specifications are given in the Table ??.

Generating landmarks on the polyhedral model is simple since polyhedrons are convex by nature.

8.3.3. Illumination Model

Mapping phase of the mission requires information about the surface illumination of the asteroid. This enables the guidance algorithm to make intelligent choices of the trajectories. Since the illumination of the surface is dependent on the position of the sun with respect to the target body, its rotation rate and albedo, this model is time variant.

Sun Position

The angle subtended by the sun at the distances of the MAB can be calculated on an average to be —. As can be seen this angle is too small and will not change by much with the orbiting motion of the target body about the sun. The sun position can therefore be fixed since the asteroids move less than a degree per day and we will simulate for a maximum of 48 hrs..

Albedo

"The albedos of planets, satellites and minor planets such as asteroids can be used to infer much about their properties. The study of albedos, their dependence on wavelength, lighting angle ("phase angle"), and variation in time comprises a major part of the astronomical field of photometry. For small and far objects that cannot be resolved by telescopes, much of what we know comes from the study of their albedos. For example, the absolute albedo can indicate the surface ice content of outer Solar System objects, the variation of albedo with phase angle gives information about regolith properties, whereas unusually high radar albedo is indicative of high metal content in asteroids."

Asteroid Rotation

The asteroid rotation rate is already included in the asteroid model and hence can be directly used for the illumination model.

The illumination model is therefore time dependent due to the asteroid rotation rate only. The position of the facets in the polyhedral model of the asteroid is known with respect to the asteroid and the normals to these facets can be calculated as discussed in Chapter 3 in Eq.—. The sun position can be rotated with the help of

the quaternion $\mathbf{q}_{A/I}$. The time dependent angle between the normals and the sun position is calculated as below,

$$\cos \theta = \frac{\mathbf{n}_f \cdot \mathbf{r}_{sun}}{\|\mathbf{r}_{sun}\|} \quad (8.7)$$

This comprises the illumination model providing the guidance algorithm with the information to make an intelligent decision.

8.4. Dynamics Model

The dynamics block as discussed earlier is responsible for incorporating the motion of the SC and the target body. It simulates the translational and rotational motion of the SC as well the rotational motion of the asteroid. It contains a model based on quaternions and another based on DQs. The software architecture presented in Figure 8.1 shows the two outputs from the dynamics block one representing the simulated inertial state and computed relative state. In this section we will verify the dynamics derived in Chapter 5 in the relative frame aligned with the body fixed frame but centre fixed at the asteroid.

8.4.1. Translational and Rotational Motion

The developed dynamics block uses ode45 to integrate the dynamic equations in quaternions and dual quaternions. To verify the translational and rotational motion of the SC given by the EQ. , we consider a simple example with a central point-mass gravity field and in the absence of perturbing forces and torques. This would lead to a normal and precise Keplerian orbit with constant energy.

Test Case: Sphere of radius (target body): 50 km, Mean density: 5000 kg/m³, Semi major axis, a : 60 km, Eccentricity: 0, Inclination: 0°. The mass of the target body is therefore 2.618×10^{18} kg. Using the gravitational constant, G as 6.67×10^{-11} kg m². We consider the A frame to be rotating about the Z-axis of the I frame with a constant angular velocity of $3e-04$ rad/s and the B frame rotating about its X-axis with $6.28318e-4$ rad/s. The test case is the same as Razgus 2017 and hence we can compare the results for the integrator in the inertial frame and then use it verify the integrator wit DQs in the relative frame B. The gravitational acceleration, the circular velocity at the altitude of 10km (both in the asteroid centre fixed inertial frame) and the period of the orbit can be given by the formulae:

$$\mathbf{g}_I = G \frac{M_{\text{target}}}{r^3} \mathbf{r}_I = 0.048535 \text{ m/s}^2, \quad v_{\text{circ}} = \sqrt{\frac{GM_{\text{target}}}{a}} = 53.964 \text{ m/s}, \quad T = 2\pi \sqrt{\frac{a^3}{GM_{\text{target}}}} \approx 6986 \text{ s} \quad (8.8)$$

We simulate the equatorial orbit for 20,000 secs with the initial conditions as follows,

$$\mathbf{r}_0^I = \begin{pmatrix} 0 \\ 60 \\ 0 \end{pmatrix} \text{ km}, \quad \mathbf{v}_0^I = \begin{pmatrix} 53.964 \\ 0 \\ 0 \end{pmatrix} \text{ m/s}, \quad \boldsymbol{\omega}_{A/I}^I = \begin{pmatrix} 0 \\ 0 \\ 3e^{-4} \end{pmatrix} \text{ rad/s}, \quad \boldsymbol{\omega}_{B/I}^I = \begin{pmatrix} 6.28e^{-4} \\ 0 \\ 0 \end{pmatrix} \text{ rad/s}, \quad (8.9)$$

$$\mathbf{q}_{B/I} = \begin{pmatrix} 0 \\ 0 \\ 0 \\ 1 \end{pmatrix}, \quad \mathbf{q}_{A/I} = \begin{pmatrix} 0 \\ 0 \\ 0 \\ 1 \end{pmatrix} \quad (8.10)$$

Figure 8.6 presents the results obtained from the simulation. The plot in the left represents the position of the SC orbiting the asteroid with a point mass gravity field and the one to the right represents the the angular velocity of the B frame with respect to I frame. Since the initial conditions suggest an orbit in the equatorial plane (X-Y plane), the Z-axis component of the SC in the I frame remains zero throughout the duration of approximately three orbital periods. Also with respect to the inertial frame the angular velocity of the B frame remains constant. These results match with the ones presented in Razgus 2017. Also the values of total energy and gravitational acceleration remain constant at .. and .. respectively as also obtained by Razgus 2017. Hence the inertial frame integrator is verified and can be used to generate the orbits and angular velocities in the A frame and B frame. These are then used to verify the DQ dynamics and kinematics integrator in the A frame and B frame.

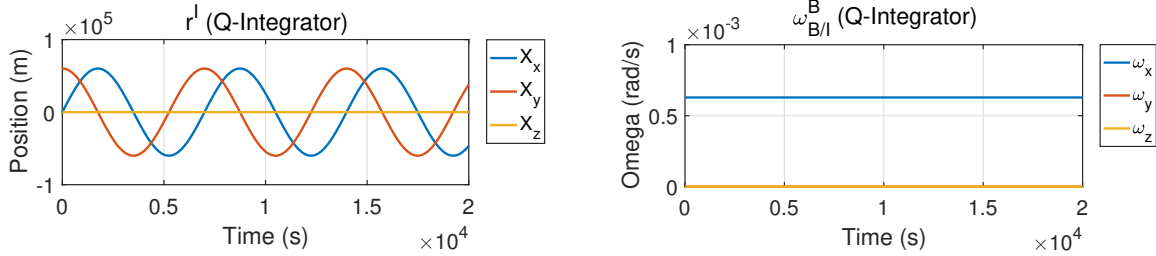


Figure 8.6: Simulated motion in the I frame.

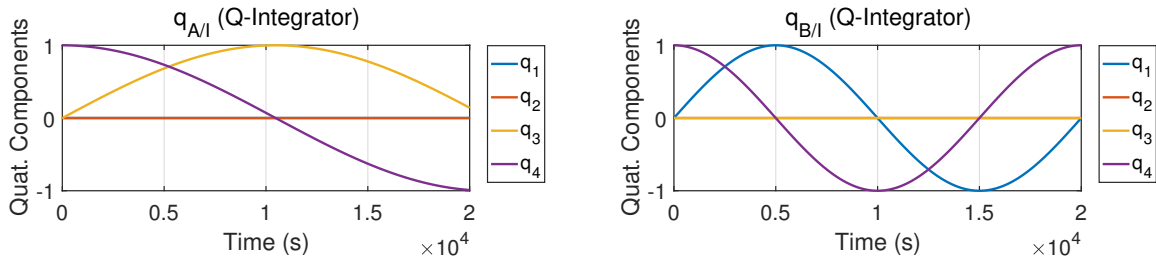


Figure 8.7: Simulated quaternions in the I frame.

Figure 8.8 represents the position of SC in the A frame and Figure 8.9 in the B frame. As can be seen the results from the inertial integrator converted by DCMs to the A frame and the results from the DQ integrator match. Similarly in Figure 8.10 and Figure 8.11 for the angular velocity, $\omega_{B/I}$ in the A and B frame respectively the results from the Q integrator match those from the inertial integrator. We do a similar comparison for the quaternion in Figure 8.12, $q_{B/A}$ and see the results match too.

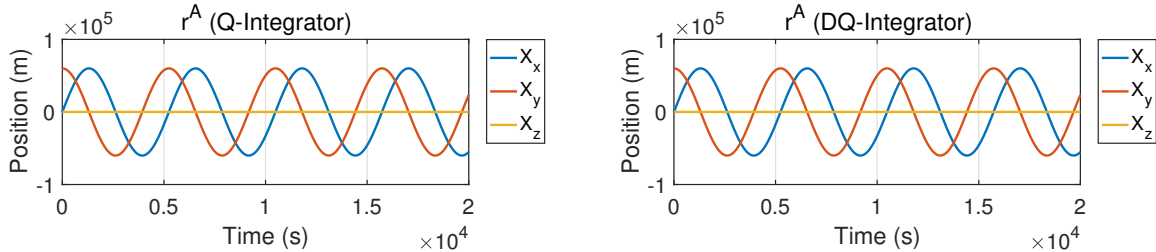


Figure 8.8: Simulated motion in the A frame from Inertial integrator (left) and DQ integrator (right).

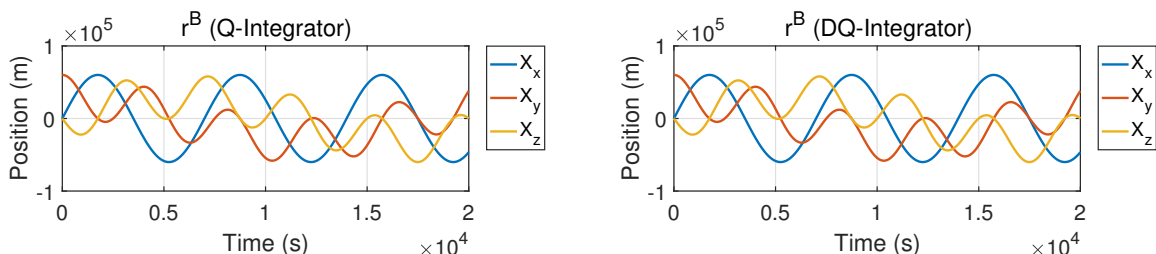
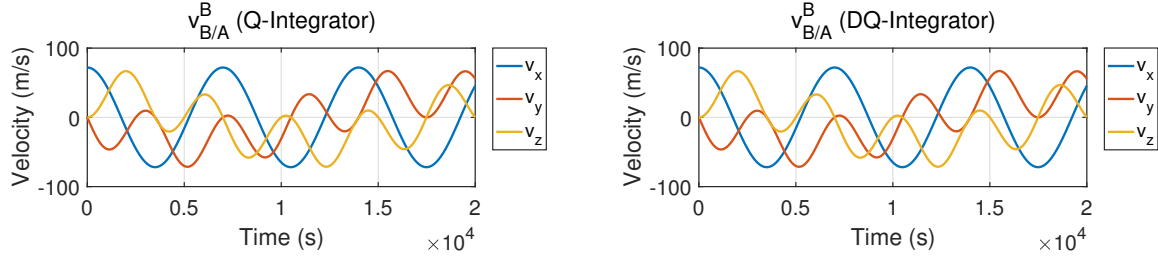
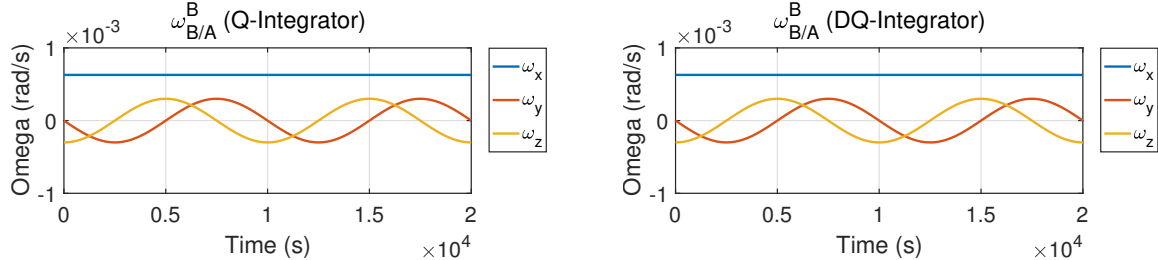
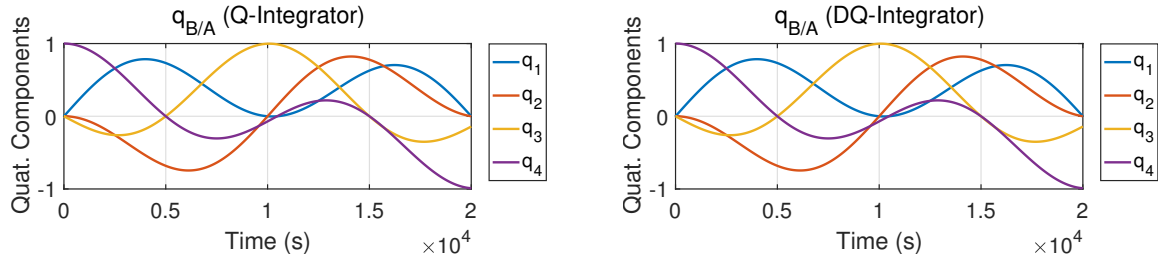


Figure 8.9: Simulated motion in the B frame from Inertial integrator (left) and DQ integrator (right).

Figure 8.10: Simulated angular velocity, $\omega_{B/A}^A$ from Inertial integrator (left) and DQ integrator (right).Figure 8.11: Simulated relative velocity, $v_{B/A}^B$ from Inertial integrator (left) DQ and integrator (right).Figure 8.12: Simulated angular velocity, $q_{B/A}$ from Inertial integrator(left) DQ integrator(right).

Hence the DQ dynamic and kinematic eoms derived in Chapter 5 have been verified to produce the right results.

8.4.2. Solar Radiation Pressure

As shown in Figure 8.2, the SC is made of N plates/faces having an area of A_i and reflectivity α_i . The analytical equation given in Chapter 5, Eq..., gives the sum of the SRP on individual plates. In this section, we use a test case to verify that the mathematical model of the SRP works correctly. Variation equations given in Wakker 2015 will be used for verification. The equations for maximum variation in the orbital elements are as below (Wakker 2015),

$$|\Delta a|_{max} = 2 \frac{f}{n_0^2} \cos \alpha_0 \quad (8.11)$$

$$|\Delta i|_{max} = \frac{f}{n_0^2 r_0} \sin \alpha_0 \quad (8.12)$$

$$|\Delta \Omega|_{max} = 2 \frac{f}{n_0^2 r_0} \sin \alpha_0 \quad (8.13)$$

where, a , i & Ω are the semi-major axis, inclination and right ascension of the ascending node of a Keplerian orbit. f is the acceleration caused by SRP, n_0 the mean motion in orbit and α_0 the angle between the orbital plane and sun direction.

Test Case: Same target body as used for eom model verification, just this time the inclination of the orbit is 90° and the initial position and velocity in the I frame are $[0 \ 0 \ 60]^T$ km and $[0 \ 53.964 \ 0]^T$ m/s respectively. 90.000003983558599 i, 90.000002003184505 omega

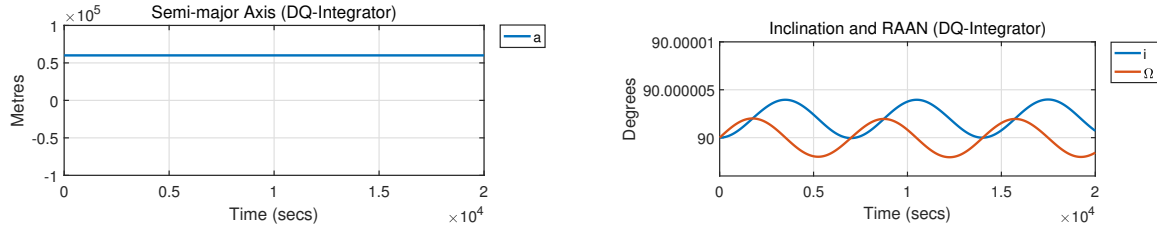


Figure 8.13: Orbital element variations due to SRP force (simulations).

8.4.3. Third Body Perturbation

$$|\Delta i|_{max} = \frac{-3}{2}\pi \frac{\mu_d}{\mu} \frac{r_0}{r_d}^3 \sin i_0 \sin 2\alpha_0 \quad (8.14)$$

$$|\Delta\Omega|_{max} = -3\pi \frac{\mu_d}{\mu} \frac{r_0}{r_d}^3 \cos i_0 \sin 2\alpha_0 \quad (8.15)$$

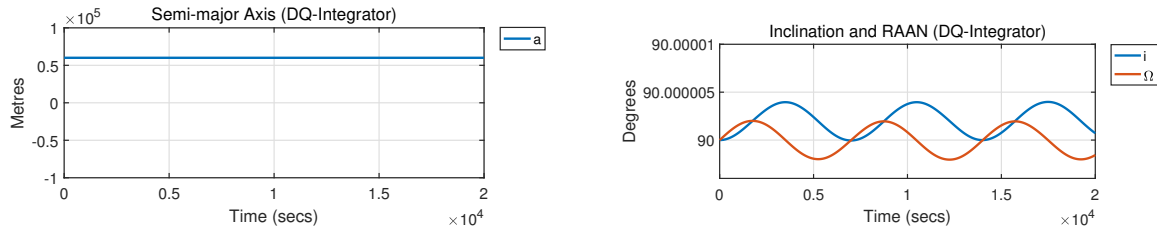


Figure 8.14: Orbital element variations due to 3rd body force (simulations).

8.4.4. Gravity Gradient Torque

8.4.5. Polyhedron Gravity

The polyhedral gravity model has been provided by Razgus 2017. It has been thoroughly verified and hence will be used as is without any changes. The only change would be to convert it to a .mex file to have faster computations of gravity. To make sure that there have been no unintentional changes in the file, the results for a $20 \times 10 \times 10$ m cuboid are compared with the results in Razgus 2017. The following table shows there is no discrepancy in the obtained values and hence the polyhedron gravity field block works fine.

To prove that the .mex files indeed makes computations faster, we generate the gravity field around Kleopatra with 64000 points. With the .m file the computation time is —secs whereas with the .mex file —secs. As can be seen the computation is $----- \times$ faster. Figure 8.15 shows the plot of the gravity field around Kleopatra to 20000 m altitude.

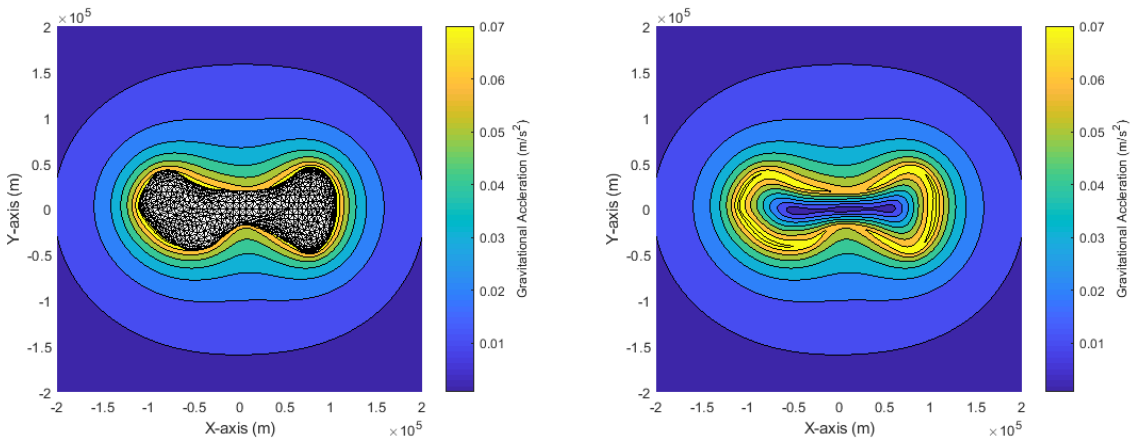


Figure 8.15: Gravity field of Kleopatra in the X-Y plane

8.5. Validation

8.5.1. SPICE

SPICE stands for Spacecraft, Planet, Instrument, C-matrix, Events. NASA's Navigation and Ancillary Information Facility (NAIF) developed this open source software toolkit with data compatible with MATLAB. This toolkit can read data kernels that contain ephemerides of the planets, SC, coordinate frame definitions and attitude. It has data from missions, with the instrument frames and corresponding orientations defined. Razgus 2017 used SPICE to retrieve data for the Rosetta mission for validation purposes and initial data for simulations and we will be continuing with the same for thesis work.

8.6. Control Actuators

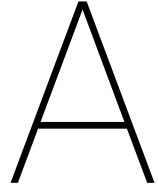
8.7. Navigation

9

Results

10

Conclusions and Recommendations



Mathematical Properties

Matrices

Quaternions

a, b & c are quaternions and $\gamma \in \mathbb{R}$

$$\begin{aligned} \mathbf{a} \otimes (\mathbf{b} + \mathbf{c}) &= \mathbf{a} \otimes \mathbf{b} + \mathbf{a} \otimes \mathbf{c} \\ (\mathbf{a} \otimes \mathbf{b})^* &= \mathbf{b}^* \otimes \mathbf{a}^* \\ (\gamma \mathbf{a}) \otimes \mathbf{b} &= \mathbf{a} \otimes \gamma \mathbf{b} + \gamma(\mathbf{a} \otimes \mathbf{b}) \\ \mathbf{a} \otimes (\mathbf{b} \otimes \mathbf{c}) &= (\mathbf{a} \otimes \mathbf{b}) \otimes \mathbf{c} \\ \mathbf{a}^T (\mathbf{b} \otimes \mathbf{c}) &= \mathbf{c}^T (\mathbf{b}^* \otimes \mathbf{a}) = \mathbf{b}^T (\mathbf{a} \otimes \mathbf{c}^*) \end{aligned}$$

Unit Quaternion Triple Identity

$$(\mathbf{t} \otimes \mathbf{q})^T (\mathbf{y} \otimes \mathbf{q}) = (\mathbf{q} \otimes \mathbf{t})^T (\mathbf{q} \otimes \mathbf{y}) = \mathbf{t}^T \mathbf{y} = \mathbf{y}^T \mathbf{t}$$

Bibliography

- [1] Açıkmeşe, B., Carson, J. M., and Blackmore, L. "Lossless convexification of nonconvex control bound and pointing constraints of the soft landing optimal control problem". *IEEE Transactions on Control Systems Technology* Vol. 21.No. 6 (2013), pp. 2104–2113. DOI: 10.1109/TCST.2012.2237346.
- [2] Açıkmeşe, B. and Ploen, S. R. "Convex programming approach to powered descent guidance for Mars landing". *Journal of Guidance, Control and Dynamics* Vol. 30.No. 5 (2007), pp. 1353–1366. DOI: 10.1109/TCST.2012.2237346.
- [3] Berry, K. et al. "Osiris-rex touch-and-go (tag) mission design and analysis". *Advances in the Astronautical Sciences* Vol. 149 (2013), pp. 667–678.
- [4] Beshore, E. et al. "The OSIRIS-REx Asteroid Sample Return Mission". *IEEE* (2015).
- [5] Boyd, S. and Vandenberghe, L. *Convex Optimization*. Vol. 25. Cambridge University Press, 2010. DOI: 10.1080/10556781003625177.
- [6] Capolupo, F., Simeon, T., and Berges, J. "Heuristic Guidance Techniques for the Exploration of Small Celestial Bodies". *IFAC-PapersOnLine* Vol. 50.No. 1 (2017), pp. 8279–8284. DOI: 10.1016/j.ifacol.2017.08.1401.
- [7] Daniilidis, K. "Hand-Eye Calibration Using Dual Quaternions". *Int. J. Robot. Res.* Vol. 18.No. 3 (1999), pp. 286–298.
- [8] Dickinson, C. et al. "An Overview of the OSIRIS REx Laser Altimeter (OLA)". *43rd Lunar and Planetary Science Conference* (2012).
- [9] Dong, H. et al. "Dual-Quaternion-Based Fault-Tolerant Control for Spacecraft Tracking With Finite-Time Convergence". *IEEE Transactions on Control Systems Technology* Vol. 25.No. 4 (2017), pp. 1231–1242. DOI: 10.1109/TCST.2016.2603070.
- [10] Filipe, N. and Tsiotras, P. "Adaptive Model-Independent Tracking of Rigid Body Position and Attitude Motion with Mass and Inertia Matrix Identification using Dual Quaternions". *AIAA Guidance, Navigation, and Control (GNC) Conference* (2013), pp. 1–15. DOI: 10.2514/6.2013-5173.
- [11] Fujiwara, A. et al. "The Rubble-Pile Asteroid Itokawa as Observed by Hayabusa". *Science* Vol. 312 (2006), pp. 1330–1334. DOI: 10.1126/science.1125841.
- [12] GalEdd, J. and Chevront, A. "The OSIRIS-REx Asteroid Sample Return Mission Operations Design ". *IEEE* (2015).
- [13] Geissler, P. et al. "Collisional and dynamical history of Ida". *Icarus* Vol. 120.No. 1 (1996), pp. 106–118. DOI: 10.1006/icar.1996.0040.
- [14] Hampton, D. L. et al. "An Overview of the Instrument Suite for the Deep Impact Mission". *Space Science Reviews* Vol. 117.No. 1 (Mar. 2005), pp. 43–93. DOI: 10.1007/s11214-005-3390-8.
- [15] Hapke, B. "Bidirectional reflectance spectroscopy. 4. The extinction coefficient and the opposition effect". *Icarus* 67 (1986), pp. 264–280.
- [16] Harris, A. W., Fahnestock, E. G., and Pravec, P. "On the shapes and spins of "rubble pile" asteroids". *Icarus* Vol. 199.No. 2 (2009), pp. 310–318. DOI: 10.1016/j.icarus.2008.09.012.
- [17] Holsapple, K. A. "Equilibrium configurations of solid cohesionless bodies". *Icarus* Vol. 154.No. 2 (2001), pp. 432–448. DOI: 10.1006/icar.2001.6683.
- [18] Jia, Y. B. "Dual quaternion" (2013), pp. 1–8.
- [19] Kavan, L. et al. "Skinning with dual quaternions". *Proceedings of the 2007 symposium on Interactive 3D graphics and games* (2007), pp. 39–46. DOI: 10.1145/1230100.1230107.
- [20] Kenwright, B. "A Beginners Guide to Dual-Quaternions: What They Are, How They Work, and How to Use Them for 3D Character Hierarchies". *The 20th International Conference on Computer Graphics, Visualization and Computer Vision* (2012), pp. 1–13. DOI: 10.1109/CVPR.2015.7298631.

- [21] Kubota, T. et al. "Guidance and navigation of Hayabusa spacecraft for asteroid exploration and sample return mission". *2006 SICE-ICASE International Joint Conference* (2006), pp. 2793–2796. DOI: 10.1109/SICE.2006.314761.
- [22] Kwon, J. W., Lee, D., and Bang, H. "Virtual Trajectory Augmented Landing Control Based on Dual Quaternion for Lunar Lander". *Journal of Guidance, Control, and Dynamics* Vol. 39.No. 9 (2016), pp. 2044–2057. DOI: 10.2514/1.G001459.
- [23] Lee, U. and Mesbahi, M. "Constrained Autonomous Precision Landing via Dual Quaternions and Model Predictive Control". *Journal of Guidance, Control, and Dynamics* Vol. 40.No. 2 (2017), pp. 292–308. DOI: 10.2514/1.G001879.
- [24] Lee, U. and Mesbahi, M. "Optimal Powered Descent Guidance with 6-DoF Line of Sight Constraints via Unit Dual Quaternions". *AIAA Guidance, Navigation, and Control Conference* (2015), pp. 1–21. DOI: 10.2514/6.2015-0319.
- [25] Ley, W., Wittmann, K., and Hallmann, W. *Handbook of Space Technology*. John Wiley & Sons, Ltd., 2011.
- [26] Lissauer, J. J. and Pater, I. de. *Fundamental Planetary Science*. Cambridge University Press, New York, USA, 2013.
- [27] Mao, Y., Szmuk, M., and Acıkmeşe, B. "Successive convexification of non-convex optimal control problems and its convergence properties". *2016 IEEE 55th Conference on Decision and Control, CDC 2016* (2016), pp. 3636–3641. DOI: 10.1109/CDC.2016.7798816.
- [28] Markley, L. F. and Crassidis, J. L. *Fundamentals of Spacecraft Attitude Determination and Control*. Springer, 2013. DOI: 10.1007/978-1-4939-0802-8.
- [29] Maruya, M. et al. "Estimation of Motion and Shape of Asteroid Based on Image Sequences". *14th Int. Symposium on Space Flight Dynamics* (2000).
- [30] Mastrodemos, N., Kubitschek, D. G., and Synnott, S. P. "Autonomous Navigation for the Deep Impact Mission Encounter with Comet Tempel 1". *Space Science Reviews* Vol. 117.No. 1 (2005), pp. 95–121. DOI: 10.1007/s11214-005-3394-4.
- [31] McDonald, J. "Teaching quaternions is not complex". *Computer Graphics Forum* Vol. 29.No. 8 (2010), pp. 2447–2455. DOI: 10.1111/j.1467-8659.2010.01756.
- [32] Montebrick, O. and Gill, E. *Satellite Orbits: Models, Methods and Applications*. American Institute of Aeronautics and Astronautics, 2008.
- [33] Munoz, P. "Preparations and Strategy for Navigation During Rosetta Comet Phase". *Issf* (2012), pp. 1–17.
- [34] Park, R. S., Werner, R. A., and Bhaskaran, S. "Estimating Small-Body Gravity Field from Shape Model and Navigation Data". *Journal of Guidance, Control, and Dynamics* Vol. 33.No. 1 (2010), pp. 212–221. DOI: 10.2514/1.41585.
- [35] Pavone, M. et al. "Spacecraft Autonomy Challenges for Next Generation Space Missions". *Springer Lecture Notes in Control and Information Sciences* (2014), pp. 1–34. DOI: 10.1007/978-3-662-47694-9_1.
- [36] Pfeiffer, C. "An Analysis of Guidance Modes". Tech. rep. NASA Electronics Research Center (1968).
- [37] Razgus, B. "Relative Navigation in Asteroid Missions: Dual Quaternion Approach". MA thesis. Technical University of Delft, 2017.
- [38] Razgus, B., Mooij, E., and Choukroun, D. "Relative Navigation in Asteroid Missions Using Dual Quaternion Filtering". *Journal of Guidance, Control, and Dynamics* Vol. 40.No. 9 (2017), pp. 1–16. DOI: 10.2514/1.G002805.
- [39] Sagliano, M. "Pseudospectral Convex Optimization for Powered Descent and Landing". *Journal of Guidance, Control, and Dynamics* (2017), pp. 1–15. DOI: 10.2514/1.G002818.
- [40] Sawai, S. et al. "Robotics Technology for Asteroid Sample Return Mission MUSES-C". *6th International Symposium on Artificial Intelligence and Robotics Automation in Space* (2001).
- [41] Schaub, H. and Junkins, J. L. *Analytical Mechanics of Space Systems*. American Institute of Aeronautics and Astronautics, 2009.

- [42] Scheeres, D. J. "Orbit Mechanics About Asteroids and Comets". *Journal of Guidance, Control, and Dynamics* Vol. 35.No. 3 (2012), pp. 987–997. DOI: 10.2514/1.57247.
- [43] Seabrook, J. et al. "Shape Model Construction of Bennu using the OSIRIS-REX Laser Altimeter (OLA)." *48th Lunar and Planetary Science Conference* (2017).
- [44] Sheppard, S. S., Jewitt, D., and Kleyna, J. "A Survey for "Normal" Irregular Satellites around Neptune: Limits to Completeness". *The Astronomical Journal* Vol. 132.No. 1 (2006), pp. 171–176. DOI: 10.1086/504799.
- [45] Sidi, M. J. *Spacecraft Dynamics and Control*. Cambridge University Press, 1997.
- [46] Surovik, D. A. and Scheeres, D. J. "Autonomous Maneuver Planning at Small Bodies via Mission Objective Reachability Analysis". *AIAA/AAS Astrodynamics Specialist Conference* (2014), pp. 1–12. DOI: 10.2514/6.2014-4147.
- [47] Surovik, D. A. and Scheeres, D. J. "Non-Keplerian Trajectory Planning via Heuristic-Guided Objective Reachability Analysis" (2017).
- [48] Szmuk, M. and Açıkmese, B. "Successive Convexification for Mars 6-DoF Rocket Powered Landing with Free-Final-Time". *AIAA Guidance, Navigation, and Control Conference* (2018).
- [49] Szmuk, M., Utku, E., and Açıkmese, B. "Successive Convexification for Mars 6-DoF Powered Descent Landing Guidance". *AIAA Guidance, Navigation, and Control Conference*. (2017).
- [50] Takahashi, Y. and Scheeres, D. J. *Small body surface gravity fields via spherical harmonic expansions*. Vol. 119. 2. 2014, pp. 169–206. DOI: 10.1007/s10569-014-9552-9.
- [51] Tsuda, Y., Yoshikawa, M., Abe, M., et al. "System design of the hayabusa 2-asteroid sample return mission to 1999 JU3". *Acta Astronautica* Vol. 91 (2013), pp. 356–362. DOI: 10.1016/j.actaastro.2013.06.028.
- [52] Tsuda, Y., Yoshikawa, M., Saiki, T., et al. "Hayabusa2-Sample return and kinetic impact mission to near-earth asteroid Ryugu". *Acta Astronica* (2017).
- [53] Utashima, M. "Spacecraft Orbits Around Asteroids for Global Mapping". *Journal of Spacecraft and Rockets* Vol. 34.No. 2 (1997).
- [54] Wakker, K. F. *Fundamentals of Astrodynamics*. Technical University of Delft, 2015.
- [55] Werner, R. A. and Scheeres, D. J. "Exterior gravitation of a polyhedron derived and compared with harmonic and mascon gravitation representations of asteroid 4769 Castalia". *Celestial Mechanics and Dynamical Astronomy* Vol. 65.No. 3 (1997), pp. 313–344.
- [56] Wie, B. *Space Vehicle Dynamics and Control*. Springer Verlag, Heidelberg, 2001.
- [57] Woicke, S. et al. "Comparison of Crater-Detection Algorithms for Terrain-Relative Navigation". *AIAA Guidance, Navigation, and Control Conference* (2018).
- [58] Xinfu, L. and Ping, L. "Solving Nonconvex Optimal Control Problems by Convex Optimization". *Journal of Guidance, Control, and Dynamics* Vol. 37.No. 3 (2014).
- [59] Xinfu, L., Ping, L., and Binfeng, P. "Survey of convex optimization for aerospace applications". *Astrodynamics*. Vol. 1.No. 1 (2017).
- [60] Zhang, F. and Duan, G. "Robust Integrated Translation and Rotation Finite-Time Maneuver of a Rigid Spacecraft Based on Dual Quaternion". *AIAA Guidance, Navigation, and Control Conference* No. 92 (2011), pp. 1–17. DOI: 10.2514/6.2011-6396.